The role of the self-energy in the functional renormalization group description of interacting Fermi systems

Dissertation
der Mathematisch-Naturwissenschaftlichen Fakultät
der Eberhard Karls Universität Tübingen
zur Erlangung des Grades eines
Doktors der Naturwissenschaften
(Dr. rer. nat)

vorgelegt von
Cornelia Undine Hille
aus Homburg

Tübingen
2020

Gedruckt mit Genehmigung der
Mathematisch-Naturwissenschaftlichen Fakultät der Eberhard Karls
Universität Tübingen

Tag der mündlichen Qualifikation:	19.06.2020
Dekan:	Prof. Dr. Wolfgang Rosenstiel
1. Berichterstatter:	Prof. Dr. Sabine Andergassen
2. Berichterstatter:	Prof. Dr. Carsten Honerkamp

Abstract:

The functional renormalization group (fRG) has a long history in the qualitative exploration of correlated electron systems in condensed matter. In this work, the fRG method is improved by the implementation of an efficient parametrization of the two-particle vertex and of the multiloop extension, circumventing the standard hierarchy truncation in fRG and recovering the parquet approximation. With these developments, the response functions remain finite at all studied temperatures indicating that, in agreement with the Mermin-Wagner theorem, there is no spontaneous symmetry breaking at finite temperatures. Furthermore, a detailed analysis of the self-energy and susceptibilities in the 2D Hubbard model is performed showing that it is now possible to obtain quantitatively reliable results. However, for the exact comparison between fRG and parquet in the case of a Truncated Unity momentum parametrization of the vertex, a new flow equation for the self-energy has to be introduced. Therefore, this work focuses on the self-energy which describes the effect of the interaction on the single-particle propagation. It is analysed on a diagrammatic level, how the conventional flow equation generates approximations when a finite number of form-factors in the Truncated Unity momentum parametrization is used. The new flow scheme, inspired by the exact Schwinger-Dyson relation, resolves this issue leading to excellent agreement between post-processing and flowing fRG results as well as between the fRG and the self-consistent parquet approach. Also, the comparison of the fRG results to numerically exact determinant Quantum Monte Carlo data shows a very good agreement up to moderate interaction strengths. Furthermore, it is shown that the Schwinger-Dyson inspired flow scheme is able to open a pseudogap in the 2D Hubbard model at half-filling, in contrast to the conventional flow. This property is analysed using diagrammatic arguments. In addition, long-range antiferromagnetic fluctuations are found to be responsible for this prominent feature observed in high-T_c superconductors.

The improvements on fRG presented in this work represent the basis for future qualitative investigations and quantitative calculations on the 2D Hubbard model as well as other interesting model systems.

Zusammenfassung:

Die funktionale Renormierungsgruppe (fRG) wird in der kondensierten Materie schon seit langem für qualitative Untersuchungen korrelierter Elektronensysteme angewandt. In dieser Arbeit wird diese Methode durch die Implementierung einer effizienten Parametrisierung der Zwei-Teilchen-Wechselwirkung und der multiloop Erweiterung, welche die übliche Hierarchietrunkierung in fRG umgeht und die Parquet Näherung erfüllt, verbessert. Diese Weiterentwicklung führt zu endlichen Suszeptibilitäten für alle untersuchten Temperaturen, sodass, im Einklang mit dem Mermin-Wagner Theorem, keine spontane Symmetriebrechung bei endlichen Temperaturen auftritt. Außerdem wird eine detaillierte Analyse der Selbstenergie und Suszeptibilitäten im 2D Hubbard Modell durchgeführt. Diese zeigt, dass zuverlässige quantitative Ergebnisse berechnet werden können. Allerdings muss für den exakten Vergleich zwischen fRG und Parquet eine neue Selbstenergie-Flussgleichung eingeführt werden, falls die Impulsabhängigkeit der effektiven Wechselwirkung durch Truncated Unity parametrisiert wurde. Um dies zu erklären, konzentriert sich diese Arbeit auf die Selbstenergie, welche Wechselwirkungseffekte auf dem Einteilchenpropagator beschreibt. Durch diagrammatische Argumente wird gezeigt, wie die herkömmliche Flussgleichung bei endlicher Anzahl von Formfaktoren in der Truncated Unity Impulsparametrisierung genäherte Diagramme erzeugt. Die exakte Schwinger-Dyson Gleichung dient als Vorbild für die neue Flussgleichung, welche dieses Problem behebt und zu einer sehr guten Übereinstimmung zwischen den direkten und nachträglich berechneten Ergebnissen des fRG Flusses als auch zwischen der fRG und der selbstkonsistenten Parquet Methode führt. Der Vergleich zwischen fRG Ergebnissen und der numerisch exakten determinant Quantum Monte Carlo Methode zeigt ferner eine sehr gute Übereinstimmung bis zu mittleren Wechselwirkungsstärken. Des Weiteren wird gezeigt, dass der Schwinger-Dyson inspirierte Fluss eine impulsabhängige Spektrallücke (Pseudogap) im halbgefüllten 2D Hubbard Modell hervorrufen kann, während diese in der herkömmlichen Flussgleichung nicht beobachtet wird. Die diagrammatische Analyse des flussabhängigen Auftretens zeigt außerdem, dass auch in fRG der Grund für diese bedeutende in Hochtemperatur-Supraleitern auftretende Eigenschaft in langreichweitigen antiferromagnetischen Fluktuationen liegt.

Die hier eingeführten Fortschritte der fRG legen den Grundstein für weiterführende qualitative Analysen und quantitative Rechnungen im 2D Hubbard Model als auch in weiteren allgemeineren Systemen.

Acknowledgements

I would like to thank many people who shared with me the last years and the development process of this thesis. First of all, I want to thank my supervisors Sabine Andergassen and Carsten Honerkamp for the introduction in this very interesting topic, the many discussions, possibilities to present at conferences or workshops and patience when I got stuck at the correction of a bug in the code. Another very important source of knowledge and inspiration were the discussions with many other scientist among which I specifically thank Philipp Hansmann, Daniel Rohe, Alessandro Toschi and Anna Kauch.

I am particularly grateful that I could spend over a year working with Agnese Tagliavini in order to implement large part of the code, overcome frustrations, find solutions to so many problems and finally present the results in a common paper.

I also appreciated a lot to meet many nice colleagues, just mentioning the most important to me: Xiaodong Cao, Christian Eckhardt, Jannis Ehrlich, Daniil Mantadakis and Demetrio Vilardi. Thank you for the many interesting scientific discussions as well as the great time together.

A successful PhD is not only based on science but also on a lot of motivation. To keep this high, I could always count on my office mates Marcel, Sarah and Manfred (the best mascot ever), and all those great people on the 8th floor of the D-building. Many of you became very close friends. In particularly, I appreciate a lot the friendship with Fabienne, Gine and Nadia, and all the support you gave me.

It was also a great pleasure to participate and organize the *studentisches Salonorchester Tübingen*. Whatever effort I put in, it came back multiple times in appreciation and joy. Keep going!

Last but not least I want to thank the my great relatives and friends for the support, advise and encouragement throughout the time. Also, thank you, Annika, for spotting my English mistakes in this thesis! Special thanks to Paolo for the support and patience in particular in this Corona-lockdown.

Contents

1. Introduction

Interacting Fermi systems are a wide and intriguing field within condensed matter physics. It comprises the physics of electrons in a solid which, in addition to an external potential created by the ions, feel a repulsive Coulomb interaction among each other. In these complex many-body systems, unconventional phenomena arise. Among the most fascinating is the high T_c-superconductivity discovered in 1986 [6]. In cuprates, a hole doping dependent superconducting dome arises with transition temperatures up to $T_c = 164K$. At half-filling antiferromagnetic order prevails and in between a pseudogap phase can be found. The latter indicates a system in which a gap only occurs on a part of the Fermi surface. Other systems for which it is crucial to understand electronic correlations are e.g. twisted bilayer graphene, pnictides, iron arsenides, heavy fermions and other transition metal oxides.

Already without the inter-electron interaction, condensed matter systems represent quantum many-body problems. In traditional ab-initio theory, numerical solutions are obtained using methods like density functional theory [63]. However, these band-structure calculations are not sufficient if inter-electron interactions induce strong electronic correlations. In this case, a solution of the full ab-initio many-body problem would become an overwhelming numerical task. Fortunately, the physical properties of a system are mainly defined by the electrons near the Fermi energy. Therefore, the problem can be downfolded to a few-orbital or few-bands system describing accurately the physics near the Fermi surface while averaging the effect of the degrees of freedom far away. In order to describe high-T_c superconductors, the 2D Hubbard model [50] is often examined. Also this work focuses on this model, which describes rather well the arising physics although for realistic and quantitative calculations more complex models are proposed [33]. In the simplest form of the 2D Hubbard model, electrons carrying either the spin up or down can occupy discrete points of a 2D lattice. Their kinetic freedom is characterized by the amplitude of the hopping process between lattice sites with the material dependence mainly encoded in the relative strength between the next-nearest neighbor and the nearest neighbor hopping [20]. Electrons on the same lattice site interact locally and in extended versions of the 2D Hubbard model longer range interactions are added. In order to determine the interaction values from the band-structure calculations, the constrained random phase approximation (cRPA) [5] is commonly used. This weak coupling method sums up all contributions from the particle-hole excitation channel. For high energy excitations, this approximation is certainly appropriate. However, a constrained variant of the functional renormalization group (cfRG) showed that for downfolding bands near the Fermi surface, the interplay between the channels is very important [45]. In condensed matter physics, the functional renormalization group (fRG) is a weak coupling method which is unbiased regarding the included excitation channels. It can be intuitively visualized using diagrams and by artificial suppression of the channel feedback the random phase approximation can be recovered. More information about this method is provided in the following and particularly in Chapter 2. While in this work the fRG is only applied to the 2D Hubbard model, it should be kept in mind that this method can also be adapted to obtain the effective interaction parameters for the low energy model itself.

In order to solve the latter, several many-body methods were proposed. It can be attempted to obtain exact solutions by a brute-force exact diagonalization (ED) [13], which however is only possible for small system sizes. The density-matrix renormalization group (DMRG) using matrix-product states (MPS) [133, 105] which truncates the exponentially-large Hilbert space is particularly strong in the treatment for one-dimensional systems while the application to 2D systems is more difficult and less accurate [108]. Also quantum Monte Carlo (QMC) methods [143], like the determinant quantum Monte Carlo (dQMC) [11, 99] in the here included benchmark, yield exact solutions but are only applicable in a restricted parameter range as they suffer from the so-called sign-problem. When the sign approaches zero, it becomes increasingly difficult to reach statistically satisfying results. These problems cannot be solved in general and therefore it is essential to consider approximate methods. Being correct in specific limits, their validity can be, in the best case, extended to a larger parameter range. These approaches can be roughly divided into strong-coupling and weak-coupling methods. In order to investigate strong correlations, the dynamical mean-field theory (DMFT) is probably one of the most popular tools [83, 22, 23]. While it is exact in the limit of infinite dimensions, it takes into account the local excitations when applied to a final dimensional system. In order to extend the method to non-local excitations, its cluster extensions like the dynamical cluster approximation (DCA) [37], cellular dynamical mean-field theory (CDMFT) [65, 62] and variational cluster approach (VCA) [88] were introduced. Also diagrammatic extension like the dynamical vertex approximation (DΓA) [114, 36] and the functional renormalization group extension DMF^{2}RG [112] allow one to include a part of the non-local excitation on top of the single-site DMFT solution. On the weak-coupling side, the before mentioned random phase approximation is an improvement over straightforward perturbation theory. For the particle-hole channel, all contributions up to infinite order can be summed up. Yet, when electronic correlations are present, this single-channel picture is no longer sufficient. In these cases, channel coupling is provided by the fluctuation exchange approximation (FLEX) [10], the two-particle self-consistent approach (TPSC) [123], self-consistent parquet approach (PA) [8] and last but not least the fRG [82].

In this work, the fRG is pushed to new limits in terms of accuracy and applicability. In this process, it benefits from various conceptual and technical developments from many different sides which are presented in the following.

The fRG belongs to the renormalization group (RG) methods, which have found application in many fields of theoretical physics. Their ubiquity ranges from the study of divergences in quantum field theories [128], critical phenomena [134, 127] and quantum impurity problems [4, 135] to current attempts to elucidate deep learning algorithms by physics [80]. The common aspect of these questions is to relate the quantities describing the physics of a system at a specific scale to those at another scale through differential equations. These quantities are often coupling constants although no stringent restriction exists. Their evolution with the scale is referred to as “flow” in the following. In fRG, the flowing quantities are functions of variables. More specifically, for most condensed matter problems, they represent interaction vertices or response functions. Although in practice only interactions of at most two particles are considered, the describing equations are coupled to others within an infinite hierarchy of coupled differential equations. By the truncation of this hierarchy, the fRG becomes a weak-coupling method. Differently to perturbation theory, it is however not restricted to a certain order in the interaction similar to the random phase approximation. In contrast to the latter, it takes into account all excitation channels on equal footing and, most importantly for correlated electron systems, the inter-channel coupling. It is shown in this work that the multiloop extension of fRG is capable of summing up all contributions from the parquet approximation. While this is in principle also possible with the self-consistent PA, the fRG has the advantage that unphysical infrared divergences can be avoided by an appropriate choice of the flow regulator. Furthermore, while the PA yields reliable physical information only when full convergence is reached, the division into relevant, marginal and irrelevant couplings [82] in fRG allows to obtain qualitative results even if quantitative convergence cannot be obtained for conceptual or numerical reasons.

The applicability, accuracy and versatility of fRG has been already studied in zero-dimensional [54, 61] and one-dimensional systems [2, 3]. However, it is particularly interesting to apply the fRG to the 2D-Hubbard model because of its ability to cope with inter-channel coupling. This can lead to novel insights in the physics of high-T_c superconductors [139, 41, 31]. Therefore, besides its physical importance, it can also serve as a test case for new methods or implementations. While no exact solution of this model is known for all parameters, results from many methods exists. Last but not least, the fRG is not limited neither to this certain geometry nor to the single-band case. Several applications to the honeycomb lattice, describing single- or bilayer graphene, were performed [44, 59, 87]. Also the Heisenberg model on the anisotropic triangular lattice was treated [90]. The case of the multiband Hubbard model was considered for a study of the constrained fRG [46]. Unfortunately, with increasing complexity of the systems the computational requirements grow rapidly. On the one hand, reasonable simplifications are often applied in order to tackle new and challenging problems. On the other hand, technical considerations in the direction of high performance computing can push the applicability to more sensitive or complex systems [91, 76]. Although the differential equations in fRG are strongly coupled, high-performance calculations could be carried out using hybrid parallelization [76]. Nevertheless computational optimization can only tap its full potential if improvements on the theoretical and methodological side are equally imposed.

It is therefore crucial to improve and optimize the method itself while studying common systems, like the single-band 2D-Hubbard model in the case of this work. Above all in higher dimensional systems, the bad scaling of the flowing functions with the frequency and momentum parametrization demands for strong simplifications or particularly efficient treatment of these dependencies. In the following, some common approaches for the latter are presented. In the momentum sector, several approaches were pursued among which the N-patch technique [142, 141, 30, 116] and the Truncated Unity fRG (TUfRG) [76], inspired strongly by the advantages of a channel decomposition [53] and singular-mode fRG [125]. Using the latter, the two of the three independent momentum dependencies are expanded on form factors, allowing for a very fine remaining momentum resolution while keeping the numeric effort controllable. Much information regarding the principal ordering tendencies could already be obtained with a good treatment of the momenta while neglecting frequency and the self-energy describing single-particle properties [141, 140, 31, 41, 82].

Only later, the frequency dependence was added adopting different approaches to deal with the discrete Matsubara frequency grid. First, a scheme rather similar to the N-patch technique was used [117]. Also a comparison of this straightforward discretization with respect to (w.r.t.) a parametrization with Lorentz functions was performed [52]. Finally, the high-frequency asymptotics are used in Refs. [122, 89], taking advantage of detailed studies of the frequency dependence of the vertex [129, 75].

Neglecting the self-energy feedback, the numerical effort could be reduced in many early works. Nevertheless, there are two main reasons why to include it. On the one hand, the self-energy allows to access spectral properties. In the framework of the 2D-Hubbard model, it is particularly interesting as the rather particular pseudogap phase can be investigated through the excitation spectrum. The fRG method allows to study this effect from the weak-coupling perspective [43, 47, 58, 92]. On the other hand, the Fermi surface shift induced by the self-energy is relevant in the RG sense. While in some cases the feedback of the self-energy even corrected the nature of the leading instability [122], it is certainly important for quantitative predictions. The next important step in the method development is the introduction of the multiloop extension for fRG [67, 69]. With this approach, the approximation introduced through the truncation of the hierarchy of flow equations can be lifted up to the so-called parquet one. Instead of working with higher order vertices, additional equations to the flow of the self-energy and two-particle vertices are introduced. Due to the division into contributions from consecutive loop orders which decrease in weight in the weak-coupling regime, the loop order itself is the natural parameter to study the convergence. Furthermore, the computational effort only grows linearly in loop order. The theory predicts, that the fRG flow with multiloop extension leads to the same results as the self-consistent PA [68].

The implementation developed and used throughout this work incorporates momentum and frequency dependent vertices and self-energy. This full treatment was previously only applied in Ref. [117] and [122]. More specifically, the TUfRG for the momentum treatment was combined with the high-frequency asymptotics similar to Ref. [122]. In contrast to the latter, the form-factor truncation here is adaptable. In addition, the flow of the susceptibilities and fermion-boson vertices is explicitly implemented such that it can be compared to the results from the post-processing procedure. Most importantly, this work presents the first and up to date only implementation of the multiloop extension up to arbitrary loop and self-energy iteration order. Furthermore, with its possibility to choose between the conventional and a newly-created flow equation of the self-energy, spectral properties can be examined even better.

The first goal of this work is to prove that the theoretically predicted equivalence between PA and fRG holds if the multiloop extension is taken into account. A particular focus lies on the self-energy flow. It will be explained, how its conventional formulation collides with the parametrization of the vertex. This will be resolved through the introduction of an alternative flow equation of the self-energy. This could only be achieved on the basis of an extensive study of the fRG implementation itself. Therefore, this work first focuses on how the numerical accuracy of the fRG can be improved. This includes on the one hand the parametrization of the vertex and on the other hand the implementation of the multiloop extension. Due to an unbiased implementation, it is possible to study the effect of different approximations and the corrections due to the multiloop extension. An fRG internal comparison between results coming from different loop truncations already shows a reduction of the pseudo-critical temperature T_{pc} hinting to an eventual satisfaction of the Mermin-Wagner theorem stated in Ref. [81]. It turns out that the multiloop fRG results do not satisfy the exact many-body relations employed also in the PA if the conventional self-energy flow is used. A detailed analytical analysis is given in order to explain this difference and show how the momentum parametrization for the vertex effects the evaluation of the self-energy flow. Only with the new flow equation for the self-energy, the many-body relations for the self-energy are satisfied. However, it improves not only quantitative numerical results but can also alter qualitative predictions as the subsequent study of the pseudogap opening in the half-filled 2D-Hubbard model shows. While this feature is one of the key properties of interest in this model, there are contradicting observations within the fRG community [139, 47, 58, 92, 119]. Also the present study finds qualitative difference between the different flow schemes. The objective in this part of the work was to confirm the stability of this feature with temperature, vertex parametrization and multiloop extension and to find an explanation for the flow scheme dependence. A detailed analysis of the involved momentum truncation shows that the exact scheme of parametrization and implementation of self-energy flow equations is important. This not only explains the apparently inconsistent results but also urges to use the new self-energy flow equation whenever a good description of spectral properties in TUfRG is needed.

This work lays the foundation for many applications. The improved accuracy allows one to search for d-wave pairing instabilities in high-T_c superconductors and in particular with the new self-energy flow scheme, the spectral properties can be studied. Its unbiased implementation allows to calculate all susceptibilities and vertices needed for comparison and the transparent structure of the equations makes it possible to study the feedback effect of the individual channels. Exploiting this modularity, the origin and effect of interesting features can be studied, in contrast to many exact methods. An application to other parameters, lattice geometries, more general bare interactions and more complicated systems can be easily realized.

The work is structured as follows: In Chapter 2, the theoretical background for the application of the fRG method is presented. This includes an introduction to the objects under consideration in Section 2.1, the explicit one loop (1ℓ) and multiloop flow equations in Section 2.2 and a discussion of the different flow schemes in Section 2.3. Many computational aspects like a study of the exact form of the flow regulators, the exact definition of the vertex parametrization and the evaluation of the fermionic excitations are collected in Section 2.4. A detailed discussion on the flow equation of the self-energy is given in Chapter 3. First in Section 3.1, it is argued why the self-energy result of the conventional flow equation does not satisfying the Schwinger-Dyson equation in TUfRG and then in Section 3.2, the improved flow equation for the self-energy is introduced. With the presented theoretical and technical know-how at hand, this improved multiloop fRG scheme is then applied to the 2D-Hubbard model in Chapter 4. After the definition of the system in Section 4.1, first an internal consistency check is performed in Section 4.2, studying explicitly the convergence w.r.t. the vertex parameters, higher loop orders and the self-energy iteration. The comparison of different approximations highlight the importance of the frequency dependence and the self-energy. Next, an external benchmark compares fRG to the self-consistent PA and dQMC in Section 4.3. The excellent agreement at small and reasonable consistency at larger interaction strengths indicates that the presented fRG implementation is suited for quantitative examinations. For same model, the focus is redirected to the potential opening of a (pseudo-)gap in Chapter 5. After an introduction on the observation of this feature with different methods Section 5.1, the results obtained in this fRG scheme are presented in Section 5.2, showing that the introduction of the new self-energy flow equation also has qualitative impact. In particular, it allows for the opening of a pseudogap in contrast to the conventional one. Finally a conclusion and outlook is given in Chapter 6.

This work is based on three publications: In the first [110], I share co-authorship with

A. Tagliavini. From this publication with the title “Multiloop functional renormalization group for the two-dimensional Hubbard model: Loop convergence of the response functions” published in *SciPost Physics*, **6**, 009 (2019), I report here the 1ℓ-flow equations in Section 2.2.1, the graphical representation of the 1ℓ-flow scheme in Fig. 2.3, Section 2.4.3 describing the calculation of the fermionic excitations, Section 4.2.1 studying the convergence with ameliorating vertex parametrization, Section 4.2.2 about the effect of different approximations, Section 4.2.3 and its discussion. The second publication [38] with the title “Quantitative functional renormalization-group description of the two-dimensional Hubbard model” currently available under the *ArXiv*-identifier 2002.02733 was submitted to *Physical Review Research.* It provided the material for part of the discussion in Section 3.1, the new self-energy flow scheme presented in Section 3.2, Figs. 4.6, 4.7, 4.9 and 4.10, their discussion, the introduction of the benchmark methods in Section 4.3.1 and benchmark itself in Section 4.3. The last publication [39] with the title ”Pseudogap opening in the two-dimensional Hubbard model: a functional renormalization group analysis”, currently available under the *ArXiv*-identifier 2003.01447 and equally submitted to *Physical Review Research* is the source for Figs. 3.2 and 3.3, Chapter 5 (except for Fig. 5.2, the right panel in Fig. 5.8, Fig. 5.9 and the right panel in Fig. 5.12) and Appendix B. Formulas, text, plots and pictures were adapted for different notations or for space distribution. My personal contributions to the publications are detailed in Appendix C.

2. The functional renormalization group

In this chapter, the fRG equations are presented and discussed. Their derivation is not reported here as it can be found in several works [96, 64, 7, 82]. Being a weak-coupling method the fRG is commonly used in the study of instabilities. It consists of an infinite hierarchy of coupled differential equations derived from the Wetterich equation [132]. Starting from a system to which the solution is known, the N-particle vertices (see Section 2.1) describing the system of interest are obtained. The evolution between these systems is described with a scale parameter Λ (see Section 2.3). The change of the functions representing the N-particle vertices is calculated through the flow equations (see Section 2.2). The functions depend on various variables including e.g. the momentum $\mathbf{k}$, frequencies ν and and other quantum numbers like spin σ and orbitals o. If possible, they are in this work collected using a single fermionic (bosonic) dependence k (q). An efficient description and implementation of these functions (see Section 2.4) is needed in order to solve the differential equations with reasonable computational effort.

2.1 N-particle vertices

This work deals with a subgroup of N-particle vertices which are represented through the flowing functions. The particles here might be either fermions or bosons. In particular, in the purely fermionic sector, the one-particle vertex, or self-energy $\Sigma(k)$ and the two-particle vertex $V(k_1, k_2, k_3)$ are considered. From the bosonic vertices, only the susceptibilities $\chi_\eta(q)$ are studied where $\eta = \mathrm{M/D/SC}$ indicates the magnetic, density and superconducting channel, respectively. Finally, the fermion-boson vertices $\gamma_{3,\eta}(q, k)$ from the mixed section are used here. These objects are shortly introduced in the following.

The self-energy $\Sigma(k)$ describes the correction of the free one-particle propagation $G_0(k)$ due to inter-particle interaction and relates the latter to the full one-particle propagator $G(k)$ by

$$\Sigma_{\sigma_1\,\sigma_2}(k) = G^{-1}_{0,\sigma_1\,\sigma_2}(k) - G^{-1}_{\sigma_1\,\sigma_2}(k)\ . \tag{2.1}$$

Using SU(2) symmetry, we separate the spin-dependence and write the self-energy in the spinless form

$$\Sigma(k) = \delta_{\sigma_1,\sigma_2}\Sigma_{\sigma_1\,\sigma_2}(k)\ . \tag{2.2}$$

The two-particle vertex $V(k_1, k_2, k_3, k_4)$ describes the effective interaction between two electrons. For momentum and frequency conserving systems, the forth dependency $k_4 =$

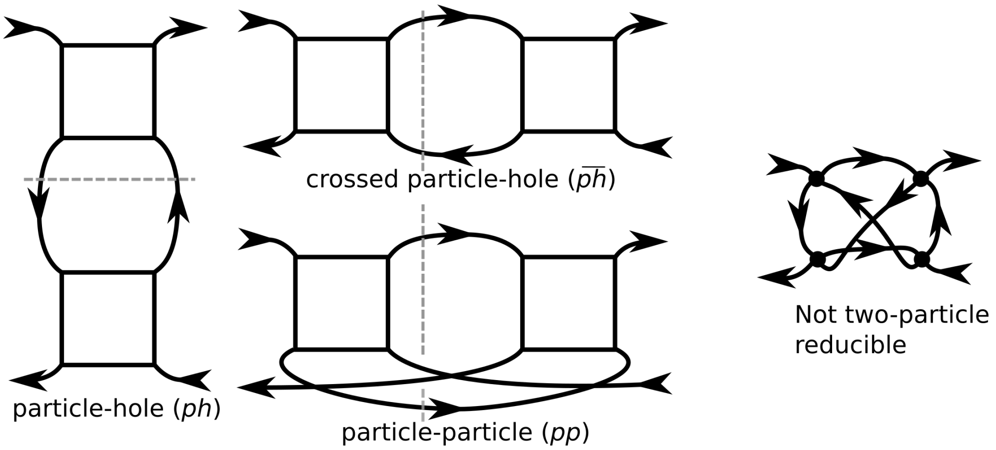

Figure 2.1: Classification of diagrams according to the parquet decomposition. The squares represent two-particle vertices, the black lines Green's functions and the gray dotted lines indicates the reducibility of the diagram. The right diagram is an example of a not two-particle reducible vertex.

$k_1 + k_3 - k_2$ is fixed. In SU(2), the spin-dependence can be eliminated through

$$\begin{aligned} V(k_1, k_2, k_3, k_4)_{\sigma_1,\sigma_2,\sigma_3,\sigma_4} = &- \delta_{\sigma_1,\sigma_4}\delta_{\sigma_2,\sigma_3} V(k_1, k_4, k_3) \\ &+ \delta_{\sigma_1,\sigma_2}\delta_{\sigma_3,\sigma_4} V(k_1, k_2, k_3) \ . \end{aligned} \tag{2.3}$$

A crucial part for the numerical treatment of any method dealing directly with the two-particle vertex is the parquet decomposition [55]

$$\begin{aligned} V(k_1, k_2, k_3) = &V_{\text{2PIR}}(k_1, k_2, k_3) + \Phi_{ph}(k_2 - k_1, k_1, k_4) \\ &+ \Phi_{\overline{ph}}(k_3 - k_2, k_1, k_2) + \Phi_{pp}(k_1 + k_3, k_1, k_2) \end{aligned} \tag{2.4}$$

and a subsequent efficient parameterization of the frequency and momentum dependency. For the two-particle irreducible (2PIR) part of the vertex, the parquet approximation $V_{\text{2PIR}}(k_1, k_2, k_3) \approx U$ is applied.

In the parquet decomposition, a diagram is considered two-particle reducible in a certain channel if cutting two single-particle propagators yields two separate parts. The association to the channel depends on which propagators are cut and is illustrated in Fig. 2.1. The power of fRG is that it can sum up the particle-hole (ph), crossed particle-hole ($\overline{ph}$) and particle-particle (pp) diagrams in an unbiased way. Diagrams which are not two-particle reducible, like the diagram on the right of Fig. 2.1, are not included in this description leading to a deviation of $\mathcal{O}(U^4)$ from the exact solution.

For the parametrization, we choose a combination of the TUfRG approach for the momentum dependence [76] and high-frequency asymptotics [129] for the frequency dependence. For a detailed description thereof, see Section 2.4.2.

The susceptibilities $\chi_\eta(q)$ describe the response of a system to external perturbation. If a system undergoes a transition to an order state, the corresponding response function diverges. For a more straightforward interpretation of a divergence, the response functions are reported directly in the physical channels η = M/D/SC. For a translation between diagrammatic and physical channels, see appendix A.

In Matsubara frequency space, the susceptibilities in the physical channels are defined via Fourier transform w.r.t. imaginary time τ,

$$\chi_\eta(\mathbf{q}, i\omega_l) = \int_0^\beta \mathrm{d}\tau e^{i\omega_l \tau} \chi_\eta(\mathbf{q}, \tau) \ , \tag{2.5}$$

where $\eta = \mathrm{M/D/SC}$ indicates the magnetic, density and superconducting (s- and d-wave) channel, respectively.

In the half-filled Hubbard model the dominant susceptibility is the antiferromagnetic (AF) one, defined by $\chi_{\mathrm{AF}} = \chi_{\mathrm{M}}(\mathbf{q} = (\pi,\pi), i\omega = 0)$ through the magnetic (or spin) susceptibility

$$\chi_{\mathrm{M}}(\mathbf{q}, \tau) = \langle T_\tau \hat{s}^z(\mathbf{q}, \tau) \hat{s}^z(\mathbf{q}, 0) \rangle - \langle \hat{s}^z(\mathbf{q}, \tau) \rangle \langle \hat{s}^z(\mathbf{q}, 0) \rangle \ , \tag{2.6}$$

where the spin operator in z-direction is $\hat{s}^z(\mathbf{q}, \tau) = (\hat{n}_\uparrow(\mathbf{q}, \tau) - \hat{n}_\downarrow(\mathbf{q}, \tau))/2$ and the spin-resolved density operator $\hat{n}_\uparrow(\mathbf{q}, \tau) = \sum_{\mathbf{k}} \hat{c}^\dagger_\uparrow(\mathbf{k} + \mathbf{q}, \tau)\, \hat{c}_\uparrow(\mathbf{k}, \tau)$. The sum over momenta includes the normalization factor $1/V_{\mathrm{BZ}}$.

The density (or charge) response function is defined by

$$\chi_{\mathrm{D}}(\mathbf{q}, \tau) = \frac{1}{4} \left(\langle T_\tau \hat{n}(\mathbf{q}, \tau) \hat{n}(\mathbf{q}, 0) \rangle - \langle \hat{n}(\mathbf{q}, \tau) \rangle \langle \hat{n}(\mathbf{q}, 0) \rangle \right) \ , \tag{2.7}$$

with $\hat{n}(\mathbf{q}, \tau) = \hat{n}_\uparrow(\mathbf{q}, \tau) + \hat{n}_\downarrow(\mathbf{q}, \tau)$. In the results the charge compressibility $\kappa = 4\chi_{\mathrm{D}}(\mathbf{q} = (0,0), i\omega = 0)$ and the charge density wave susceptibility $\chi_{\mathrm{CDW}} = \chi_{\mathrm{D}}(\mathbf{q} = (\pi,\pi), i\omega = 0)$ are shown.

For the $n = s, d$ pairing susceptibility

$$\chi_{\mathrm{SC},n}(\mathbf{q}, \tau) = \frac{1}{2} \Big\langle T_\tau \left(\hat{\Delta}_n(\mathbf{q}, \tau) \hat{\Delta}^\dagger_n(\mathbf{q}, 0) \right) \Big\rangle \ , \tag{2.8}$$

both the local s-wave $\hat{\Delta}_s(\mathbf{q}, \tau) = \sum_{\mathbf{k}} \hat{c}^\dagger_\uparrow(\mathbf{q} - \mathbf{k}, \tau) \hat{c}^\dagger_\downarrow(\mathbf{k}, \tau)$ and the nearest-neighbor d-wave pairing $\hat{\Delta}_d(\mathbf{q}, \tau) = \sum_{\mathbf{k}} (\cos(k_x) - \cos(k_y))\, \hat{c}^\dagger_\uparrow(\mathbf{q} - \mathbf{k}, \tau) \hat{c}^\dagger_\downarrow(\mathbf{k}, \tau)$ are considered. Of particular interest are the $\mathbf{q} = (0,0)$ and $i\omega_l = 0$ components, referred to as $\chi_{\mathrm{SC},s}$ and $\chi_{\mathrm{SC},d}$.

The fermion-boson vertex $\gamma_{3,\eta}(q,k)$ connects the fermionic and bosonic sector. It is defined analogously to the susceptibilities with the difference that the left one of the density (or pairing) operators are replaced by $\left[\hat{c}^\dagger_\uparrow(\mathbf{k} + \mathbf{q}, \tau_1)\, \hat{c}_\uparrow(\mathbf{k}, \tau_2) \pm \hat{c}^\dagger_\downarrow(\mathbf{k} + \mathbf{q}, \tau_1)\, \hat{c}_\downarrow(\mathbf{k}, \tau_2)\right]$ (or $\left[\hat{c}^\dagger_\uparrow(\mathbf{q} - \mathbf{k}, \tau_1) \hat{c}^\dagger_\downarrow(\mathbf{k}, \tau_2)\right] \ / \ \left[(\cos(k_x) - \cos(k_y))\, \hat{c}^\dagger_\uparrow(\mathbf{q} - \mathbf{k}, \tau_1) \hat{c}^\dagger_\downarrow(\mathbf{k}, \tau_2)\right]$).

The susceptibilities and fermion-boson vertices in this work are calculated in two different ways which are briefly introduced in this work and discussed in more detail in Ref. [109]. On the one hand, one can calculate them directly during the flow. In Sections 2.2.1 and 2.2.2, the (multiloop) flow equations are reported. On the other hand, they can be calculated subsequently using the two-particle vertex and self-energy from the end of the flow using Eq. (2.38).

2.2 Truncation of the hierarchy of flow equations and beyond

In the infinite hierarchy of flow equations derived from the Wetterich equation [132], each one describes the flow of a certain N-particle vertex. The right hand side (r.h.s.) always depends on the vertices up to the same order *and* the next higher order vertex.

This makes it impossible to solve all equations at once. Using weak-coupling and power-counting arguments [82], the hierarchy can be truncated in order to obtain a finite set of coupled differential equations. The most common approximation is the one-loop (1ℓ) fRG specified in Section 2.2.1. The multiloop extension presented in Section 2.2.2 allows to go beyond and includes also the quite popular Katanin substitution and two-loop (2ℓ) approach, which are treated within this section.

2.2.1 1ℓ-fRG

The self-energy and the two-particle vertex are described by the first two differential equations in the infinite hierarchy of the fRG. They depend on each other and on higher order vertices. One can argue that the higher order vertices contribute only at higher interaction order $\mathcal{O}[(U)^3]$. Furthermore, they have a more complex parameter dependence. For a qualitative study at weak to intermediate coupling, they are usually neglected leading to the numerically more feasible 1ℓ truncation [82]. The flow equations in the 1ℓ scheme for the self-energy and two-particle vertex are presented in the following. Throughout this work, a dot on top of a one- or two-particle vertex represents its Λ-derivative.

The self-energy flow reads

$$\dot{\Sigma}^{\Lambda}(k) = \sum_{p} \Big(V^{\Lambda}_{\sigma\,\overline{\sigma},\overline{\sigma}\,\sigma}(k,k,p) + V^{\Lambda}_{\sigma\,\sigma,\sigma\,\sigma}(k,k,p) \Big) S^{\Lambda}(p) \tag{2.9}$$

where the convention that the summation over Matsubara frequencies includes a implicit factor T and the integration over momenta is normalized over the first Brillouin zone. The single-scale propagator

$$S^{\Lambda} = \ \partial_{\Lambda} G^{\Lambda}|_{\Sigma=\text{const}} \tag{2.10}$$

is defined through the scale derivative of the Green's function at constant self-energy. By SU(2) symmetry, the equal spin vertex can be transformed to an up-down spin vertex giving

$$\dot{\Sigma}^{\Lambda}(k) = \sum_{p} \Big(2V^{\Lambda}(k,k,p) - V^{\Lambda}(p,k,k) \Big) S^{\Lambda}(p) \ . \tag{2.11}$$

The self-energy flow does not depend on vertices of order higher than the two-particle vertex and the 1ℓ-truncation enters only through the approximation of the two-particle vertex.

The vertex flow

$$\dot{V}^{\Lambda}(k_1,k_2,k_3) = \mathcal{T}^{\Lambda}_{ph}(k_2-k_1,k_1,k_4) + \mathcal{T}^{\Lambda}_{\overline{ph}}(k_3-k_2,k_1,k_2) + \mathcal{T}^{\Lambda}_{pp}(k_1+k_3,k_1,k_2) \tag{2.12}$$

consists of three parts

$$\begin{aligned}\mathcal{T}^{\Lambda}_{ph}(k_2-k_1,k_1,k_4) = \int dp\, \Big[&2\, V^{\Lambda}(k_1,k_2,k_2-k_1+p)\; V^{\Lambda}(p,k_2-k_1+p,k_3) - \\ &V^{\Lambda}(k_1,p,k_2-k_1+p)\; V^{\Lambda}(p,k_2-k_1+p,k_3) - \\ &V^{\Lambda}(k_1,k_2,k_2-k_1+p)\; V^{\Lambda}(p,k_4,k_3)\Big] \times \\ &\Big[S^{\Lambda}(p)G^{\Lambda}(k_2-k_1+p) + (S \leftrightarrow G)\Big]\;, \end{aligned} \tag{2.13a}$$

$$\begin{aligned}\mathcal{T}^{\Lambda}_{\overline{ph}}(k_3-k_2,k_1,k_2) = -\int dp\, &V^{\Lambda}(k_1,p,k_3-k_2+p)V^{\Lambda}(p,k_2,k_3)\times \\ &\Big[S^{\Lambda}(p)G^{\Lambda}(k_3-k_2+p) + (S \leftrightarrow G)\Big]\;, \end{aligned} \tag{2.13b}$$

$$\begin{aligned}\mathcal{T}^{\Lambda}_{pp}(k_1+k_3,k_1,k_2) = -\int dp\, &V^{\Lambda}(k_1,k_1+k_3-p,k_3)V^{\Lambda}(k_1+k_3-p,k_2,p)\times \\ &\Big[S^{\Lambda}(p)G^{\Lambda}(k_1+k_3-p) + (S \leftrightarrow G)\Big]\;, \end{aligned} \tag{2.13c}$$

where

$$S^{\Lambda}(k) = -G^{\Lambda}(k)\partial_{\Lambda}\big(G^{\Lambda}_0(k)^{-1}\big)G^{\Lambda}(k) = \partial_{\Lambda}G^{\Lambda}(k)|_{\Sigma^{\Lambda}(k)=\text{const.}} \tag{2.14}$$

is the single-scale propagator. Each of $\mathcal{T}^{\Lambda}_r$ contributes to one specific channel r of the parquet decomposition in Eq. (2.4) such that Eq. (2.12) can be written as three coupled differential equations each one describing one Φ_r-flow via $\dot{\Phi}^{\Lambda}_r = \mathcal{T}^{\Lambda}_r$. In the TUfRG (see also Section 2.4.2), the fermionic momentum dependence of the channels is expanded on form factors

$$\Phi_r(q,k,k') = \sum_{n\,n'} f_n(\mathbf{k})f^*_{n'}(\mathbf{k}')\Big[\mathbf{\Phi}_r(q,i\nu_m,i\nu_{m'})\Big]_{n\,n'}\;, \tag{2.15}$$

where the generalized fermionic momentum $k = \{\mathbf{k}, i\nu_m\}$ is separated in its momentum and frequency part and the bold symbols represent matrices in the form-factor space. The flow equations for the TU-projected channels read

$$\begin{aligned}\dot{\mathbf{\Phi}}^{\Lambda}_{ph}(q,i\nu_m,i\nu_{m'}) = \sum_{i\nu_{m''}} \dot{\mathbf{\Pi}}^{\Lambda}_{S,ph}(q,i\nu_{m''})\Big[&2\mathbf{V}^{\Lambda}_{ph}(q,i\nu_m,i\nu_{m''})\mathbf{V}^{\Lambda}_{ph}(q,i\nu_{m''},i\nu_{m'}) \\ &-\mathbf{V}^{\Lambda}_{\overline{ph}}(q,i\nu_m,i\nu_{m''})\mathbf{V}^{\Lambda}_{ph}(q,i\nu_{m''},i\nu_{m'}) \\ &-\mathbf{V}^{\Lambda}_{ph}(q,i\nu_m,i\nu_{m''})\mathbf{V}^{\Lambda}_{\overline{ph}}(q,i\nu_{m''},i\nu_{m'})\Big] \end{aligned} \tag{2.16a}$$

$$\dot{\mathbf{\Phi}}^{\Lambda}_{\overline{ph}}(q,i\nu_m,i\nu_{m'}) = -\sum_{i\nu_{m''}} \mathbf{V}^{\Lambda}_{\overline{ph}}(q,i\nu_m,i\nu_{m''})\dot{\mathbf{\Pi}}^{\Lambda}_{S,ph}(q,i\nu_{m''})\mathbf{V}^{\Lambda}_{\overline{ph}}(q,i\nu_{m''},i\nu_{m'}) \tag{2.16b}$$

$$\dot{\mathbf{\Phi}}^{\Lambda}_{pp}(q,i\nu_m,i\nu_{m'}) = -\sum_{i\nu_{m''}} \mathbf{V}^{\Lambda}_{pp}(q,i\nu_m,i\nu_{m''})\dot{\mathbf{\Pi}}^{\Lambda}_{S,pp}(q,i\nu_{m''})\mathbf{V}^{\Lambda}_{pp}(q,i\nu_{m''},i\nu_{m'})\;, \tag{2.16c}$$

where the fermionic bubbles (see also Section 2.4.3) with single-scale propagator (subscript S for the bubble) are defined as

$$\Big[\dot{\mathbf{\Pi}}^{\Lambda}_{S,ph}(q,i\nu_m)\Big]_{n\,n'} = \int d\mathbf{p} f^*_n(\mathbf{p})f_{n'}(\mathbf{p})\;\Big(G^{\Lambda}(k)S^{\Lambda}(q+k) + (S \leftrightarrow G)\Big)\;, \tag{2.17a}$$

$$\Big[\dot{\mathbf{\Pi}}^{\Lambda}_{S,pp}(q,i\nu_m)\Big]_{n\,n'} = \int d\mathbf{p} f^*_n(\mathbf{p})f_{n'}(\mathbf{p})\;\Big(G^{\Lambda}(k)S^{\Lambda}(q-k) + (S \leftrightarrow G)\Big)\;. \tag{2.17b}$$

Coupling the fermionic degrees of freedom to an external bosonic field, an infinite hierarchy of flow equations can be obtained also for the response functions [82, 97, 31]. The susceptibility and the fermion-boson vertex are the first two objects in this hierarchy. For completeness, we report the corresponding TUfRG-flow equations

$$\dot{\boldsymbol{\gamma}}^{\Lambda}_{3,\eta}(q,i\nu_m) = -\sum_{i\nu_{m'}} \boldsymbol{\gamma}^{\Lambda}_{3,\eta}(q,i\nu_{m'})\dot{\mathbf{\Pi}}^{\Lambda}_{S,\eta}(q,i\nu_{m'})\mathbf{V}^{\Lambda}_{\eta}(q,i\nu_{m'},i\nu_m) \tag{2.18a}$$

$$\dot{\boldsymbol{\chi}}^{\Lambda}_{\eta}(q) = \frac{1}{2}\sum_{i\nu_m} \boldsymbol{\gamma}^{\Lambda}_{3,\eta}(q,i\nu_m)\dot{\mathbf{\Pi}}^{\Lambda}_{S,\eta}(q,i\nu_m)\boldsymbol{\gamma}^{\Lambda}_{3,\eta}(q,i\nu_m)\ , \tag{2.18b}$$

where $\eta = \{\mathrm{D},\mathrm{M},\mathrm{SC}\}$ denote the physical channels. The vertices in these channels are recovered from the diagrammatic channels via Eq. (2.58) and the fermionic bubbles through

$$\dot{\Pi}^{\Lambda}_{S,\mathrm{D/M}} = -\,\dot{\Pi}^{\Lambda}_{S,ph} \tag{2.19a}$$

$$\dot{\Pi}^{\Lambda}_{S,\mathrm{SC}} = \dot{\Pi}^{\Lambda}_{S,pp}\ . \tag{2.19b}$$

In the following, the 1ℓ-flow equations in Eqs. (2.11), (2.16) and (2.18) constitute the first contribution to the multiloop flow equations. They are marked with a 1ℓ-superscript.

2.2.2 Multiloop fRG

A multiloop extension of fRG (mfRG) was recently introduced by Kugler and van Delft [67, 66] in order to sum up all parquet-like diagrams in addition to those included already in the 1ℓ-truncation. Later, it was shown explicitly that the derivation of the parquet relations leads directly to the mfRG equations [68]. The connection between fRG and the Schwinger-Dyson equations for the self-energy and the N-particle vertices was also studied by Veschgini and Salmhofer [118]. Their Schwinger-Dyson renormalization group is exact up to terms of order $\mathcal{O}[(U)^3]$ unlike the accuracy up to $\mathcal{O}[(U)^4]$ in mfRG. Further, mfRG is formulated in such a way that the computational effort only grows linearly in loop order. The numerical proof that the multiloop extension converges to a flow scheme independent solution [110] and correctly reproduces PA [12, 38] is one of the scopes of the presented work.

The first step towards the full mfRG-approach is the substitution of the single-scale propagator by the derivative of the Green's function w.r.t. the scale Λ [56]

$$S^{\Lambda} = \partial_{\Lambda} G^{\Lambda}|_{\Sigma^{\Lambda}=\mathrm{const.}} \ \rightarrow\ d_{\Lambda}G^{\Lambda} = S^{\Lambda} + G^{\Lambda}\dot{\Sigma}G^{\Lambda}\ . \tag{2.20}$$

In the following, the single-scale propagator with this Katanin substitution is denoted S^{Λ}_{K} and the fermionic bubble using the full derivative $\dot{\mathbf{\Pi}} = d_{\Lambda}\mathbf{\Pi}$ without subscript S.

The 2ℓ-extension [57, 15] provides the first explicit correction terms for the two-particle vertex flow. It leads to a reduction of the pseudo-critical scales [15] and its addition to the Katanin substitution is already correct up to $\mathcal{O}[(U)^3]$. The 2ℓ contribution corresponds to the combination of the so-called left (L) and right (R) multiloop vertex corrections

$$\dot{\Phi}^{\Lambda,2\ell}_{r} = \dot{\Phi}^{\Lambda,2\ell,L}_{r} + \dot{\Phi}^{\Lambda,2\ell,R}_{r} \tag{2.21}$$

and enter the r.h.s. of the flow equations as

$$\dot{\Phi}^{\Lambda}_{r} = \dot{\Phi}^{\Lambda,1\ell}_{r} + \dot{\Phi}^{\Lambda,2\ell}_{r}\ , \tag{2.22}$$

where $\dot{\Phi}^{1\ell}_r$ corresponds to Eq. (2.16). As the 2ℓ fRG can be considered as a special case of mfRG, the left and right multiloop vertex corrections are directly introduced in the general form

$$\begin{aligned}
\dot{\boldsymbol{\Phi}}^{\Lambda,\ell,L}_{ph}(q,i\nu_m,i\nu_{m'}) = \sum_{i\nu_{m''}} \Big(& 2\dot{\mathbf{I}}^{\Lambda,\ell-1}_{ph}(q,i\nu_m,i\nu_{m''})\boldsymbol{\Pi}^{\Lambda}_{ph}(q,i\nu_{m''})\mathbf{V}^{\Lambda}_{ph}(q,i\nu_{m''},i\nu_{m'}) \\
& - \dot{\mathbf{I}}^{\Lambda,\ell-1}_{\overline{ph}}(q,i\nu_m,i\nu_{m''})\boldsymbol{\Pi}^{\Lambda}_{ph}(q,i\nu_{m''})\mathbf{V}^{\Lambda}_{ph}(q,i\nu_{m''},i\nu_{m'}) \\
& - \dot{\mathbf{I}}^{\Lambda,\ell-1}_{ph}(q,i\nu_m,i\nu_{m''})\boldsymbol{\Pi}^{\Lambda}_{ph}(q,i\nu_{m''})\mathbf{V}^{\Lambda}_{\overline{ph}}(q,i\nu_{m''},i\nu_{m'})\Big) \ , \qquad (2.23a) \\
\dot{\boldsymbol{\Phi}}^{\Lambda,\ell,L}_{\overline{ph}}(q,i\nu_m,i\nu_{m'}) = - \sum_{i\nu_{m''}} & \dot{\mathbf{I}}^{\Lambda,\ell-1}_{\overline{ph}}(q,i\nu_m,i\nu_{m''})\boldsymbol{\Pi}^{\Lambda}_{ph}(q,i\nu_{m''})\mathbf{V}^{\Lambda}_{\overline{ph}}(q,i\nu_{m''},i\nu_{m'}) \ , \qquad (2.23b) \\
\dot{\boldsymbol{\Phi}}^{\Lambda,\ell,L}_{pp}(q,i\nu_m,i\nu_{m'}) = - \sum_{i\nu_{m''}} & \dot{\mathbf{I}}^{\Lambda,\ell-1}_{pp}(q,i\nu_m,i\nu_{m''})\boldsymbol{\Pi}^{\Lambda}_{pp}(q,i\nu_{m''})\mathbf{V}^{\Lambda}_{pp}(q,i\nu_{m''},i\nu_{m'}) \qquad (2.23c)
\end{aligned}$$

and

$$\begin{aligned}
\dot{\boldsymbol{\Phi}}^{\Lambda,\ell,R}_{ph}(q,i\nu_m,i\nu_{m'}) = \sum_{i\nu_{m''}} \Big(& 2\mathbf{V}^{\Lambda}_{ph}(q,i\nu_m,i\nu_{m''})\boldsymbol{\Pi}^{\Lambda}_{ph}(q,i\nu_{m''})\dot{\mathbf{I}}^{\Lambda,\ell-1}_{ph}(q,i\nu_{m''},i\nu_{m'}) \\
& - \mathbf{V}^{\Lambda}_{\overline{ph}}(q,i\nu_m,i\nu_{m''})\boldsymbol{\Pi}^{\Lambda}_{ph}(q,i\nu_{m''})\dot{\mathbf{I}}^{\Lambda,\ell-1}_{ph}(q,i\nu_{m''},i\nu_{m'}) \\
& - \mathbf{V}^{\Lambda}_{ph}(q,i\nu_m,i\nu_{m''})\boldsymbol{\Pi}^{\Lambda}_{ph}(q,i\nu_{m''})\dot{\mathbf{I}}^{\Lambda,\ell-1}_{\overline{ph}}(q,i\nu_{m''},i\nu_{m'})\Big) \ , \qquad (2.24a) \\
\dot{\boldsymbol{\Phi}}^{\Lambda,\ell,R}_{\overline{ph}}(q,i\nu_m,i\nu_{m'}) = - \sum_{i\nu_{m''}} & \mathbf{V}^{\Lambda}_{\overline{ph}}(q,i\nu_m,i\nu_{m''})\boldsymbol{\Pi}^{\Lambda}_{ph}(q,i\nu_{m''})\dot{\mathbf{I}}^{\Lambda,\ell-1}_{\overline{ph}}(q,i\nu_{m''},i\nu_{m'}) \ , \qquad (2.24b) \\
\dot{\boldsymbol{\Phi}}^{\Lambda,\ell,R}_{pp}(q,i\nu_m,i\nu_{m'}) = - \sum_{i\nu_{m''}} & \mathbf{V}^{\Lambda}_{pp}(q,i\nu_m,i\nu_{m''})\boldsymbol{\Pi}^{\Lambda}_{pp}(q,i\nu_{m''})\dot{\mathbf{I}}^{\Lambda,\ell-1}_{pp}(q,i\nu_{m''},i\nu_{m'}) \ , \qquad (2.24c)
\end{aligned}$$

where the two-particle irreducible vertex of channel r is defined by

$$\begin{aligned}
I_r &= V_r - \Phi_r \\
&= U + \sum_{r' \neq r} \hat{P}_{r' \to r} \Phi_{r'} \ . \qquad (2.25)
\end{aligned}$$

As usual, the two-particle reducible vertex in the channel r, Φ_r, is always in the channel-specific notation and V_r, written in the notation r, always contains all channels and the bare interaction U.

The fermionic bubbles in Eqs. (2.23) and (2.24), defined as

$$\Big[\boldsymbol{\Pi}^{\Lambda}_{ph}(q,i\omega_l,i\nu_m)\Big]_{n\,n'} = \int d\mathbf{p} f^{*}_{n}(\mathbf{p}) f_{n'}(\mathbf{p}) \ G^{\Lambda}(k) G^{\Lambda}(q+k) \ , \qquad (2.26a)$$

$$\Big[\boldsymbol{\Pi}^{\Lambda}_{pp}(q,i\omega_l,i\nu_m)\Big]_{n\,n'} = \int d\mathbf{p} f^{*}_{n}(\mathbf{p}) f_{n'}(\mathbf{p}) \ G^{\Lambda}(k) G^{\Lambda}(q-k) \ , \qquad (2.26b)$$

are, in contrast to Eq. (2.17), not derived w.r.t. the scale Λ. However, the computational difficulties and the solution thereof discussed in 2.4.3 are the same.

In any higher loop order the 1ℓ-flow equations are corrected by multiloop contributions with $\ell > 1$

$$\dot{\Phi}^{\Lambda}_{r} = \sum_{1 \leq \ell \leq N_\ell} \dot{\Phi}^{\Lambda,\ell}_{r} \ . \qquad (2.27)$$

where $\dot{\Phi}^{1\ell}$ corresponds to Eq. (2.16) and the highest loop order N_ℓ is in principle sent to infinity. The r.h.s. of the loop contribution to the flow equations becomes

$$\dot{\Phi}_r^{\Lambda,\ell} = \dot{\Phi}_r^{\Lambda,\ell,L} + \dot{\Phi}_r^{\Lambda,\ell,C} + \dot{\Phi}_r^{\Lambda,\ell,R} \,, \tag{2.28}$$

where the left and right contributions from Eqs. (2.23) and (2.24) appear again and additional central (C) diagrams for $\ell \geq 3$ have to be considered. Those diagrams carry the derivative w.r.t. the scale Λ sandwiched between two contributions involving the full vertex

$$\begin{aligned}
\dot{\mathbf{\Phi}}_{ph}^{\Lambda,\ell,C}(q, i\nu_m, i\nu_{m'}) = \sum_{i\nu_{m''}\, i\nu_{m'''}} \Big(& 4\mathbf{V}_{ph}^{\Lambda}(q, i\nu_m, i\nu_{m''})\mathbf{\Pi}_{ph}^{\Lambda}(q, i\nu_{m''}) \\
& \quad \dot{\mathbf{I}}_{ph}^{\Lambda,\ell-2,L}(q, i\nu_{m''}, i\nu_{m'''})\mathbf{\Pi}_{ph}^{\Lambda}(q, i\nu_{m'''})\mathbf{V}_{ph}^{\Lambda}(q, i\nu_{m'''}, i\nu_{m'}) \\
& - 2\mathbf{V}_{\overline{ph}}^{\Lambda}(q, i\nu_m, i\nu_{m''})\mathbf{\Pi}_{ph}^{\Lambda}(q, i\nu_{m''}) \\
& \quad \dot{\mathbf{I}}_{ph}^{\Lambda,\ell-2,L}(q, i\nu_{m''}, i\nu_{m'''})\mathbf{\Pi}_{ph}^{\Lambda}(q, i\nu_{m'''})\mathbf{V}_{ph}^{\Lambda,\ell-1,L}(q, i\nu_{m'''}, i\nu_{m'}) \\
& - 2\mathbf{V}_{ph}^{\Lambda}(q, i\nu_m, i\nu_{m''})\mathbf{\Pi}_{ph}^{\Lambda}(q, i\nu_{m''}) \\
& \quad \dot{\mathbf{I}}_{\overline{ph}}^{\Lambda,\ell-2,L}(q, i\nu_{m''}, i\nu_{m'''})\mathbf{\Pi}_{ph}^{\Lambda}(q, i\nu_{m'''})\mathbf{V}_{ph}^{\Lambda,\ell-1,L}(q, i\nu_{m'''}, i\nu_{m'}) \\
& - 2\mathbf{V}_{ph}^{\Lambda}(q, i\nu_m, i\nu_{m''})\mathbf{\Pi}_{ph}^{\Lambda}(q, i\nu_{m''}) \\
& \quad \dot{\mathbf{I}}_{ph}^{\Lambda,\ell-2,L}(q, i\nu_{m''}, i\nu_{m'''})\mathbf{\Pi}_{ph}^{\Lambda}(q, i\nu_{m'''})\mathbf{V}_{\overline{ph}}^{\Lambda,\ell-1,L}(q, i\nu_{m'''}, i\nu_{m'}) \\
& + \mathbf{V}_{\overline{ph}}^{\Lambda}(q, i\nu_m, i\nu_{m''})\mathbf{\Pi}_{ph}^{\Lambda}(q, i\nu_{m''}) \\
& \quad \dot{\mathbf{I}}_{\overline{ph}}^{\Lambda,\ell-2,L}(q, i\nu_{m''}, i\nu_{m'''})\mathbf{\Pi}_{ph}^{\Lambda}(q, i\nu_{m'''})\mathbf{V}_{ph}^{\Lambda}(q, i\nu_{m'''}, i\nu_{m'}) \\
& + \mathbf{V}_{ph}^{\Lambda}(q, i\nu_m, i\nu_{m''})\mathbf{\Pi}_{ph}^{\Lambda}(q, i\nu_{m''}) \\
& \quad \dot{\mathbf{I}}_{\overline{ph}}^{\Lambda,\ell-2,L}(q, i\nu_{m''}, i\nu_{m'''})\mathbf{\Pi}_{ph}^{\Lambda}(q, i\nu_{m'''})\mathbf{V}_{\overline{ph}}^{\Lambda}(q, i\nu_{m'''}, i\nu_{m'}) \\
& + \mathbf{V}_{\overline{ph}}^{\Lambda}(q, i\nu_m, i\nu_{m''})\mathbf{\Pi}_{ph}^{\Lambda}(q, i\nu_{m''}) \\
& \quad \dot{\mathbf{I}}_{ph}^{\Lambda,\ell-2,L}(q, i\nu_{m''}, i\nu_{m'''})\mathbf{\Pi}_{ph}^{\Lambda}(q, i\nu_{m'''})\mathbf{V}_{\overline{ph}}^{\Lambda}(q, i\nu_{m'''}, i\nu_{m'})\Big)
\end{aligned} \tag{2.29a}$$

$$\begin{aligned}
\dot{\mathbf{\Phi}}_{\overline{ph}}^{\Lambda,\ell,C}(q, i\nu_m, i\nu_{m'}) = -\sum_{i\nu_{m''}\, i\nu_{m'''}} & \mathbf{V}_{\overline{ph}}^{\Lambda}(q, i\nu_m, i\nu_{m''})\mathbf{\Pi}_{ph}^{\Lambda}(q, i\nu_{m''}) \\
& \dot{\mathbf{I}}_{\overline{ph}}^{\Lambda,\ell-2,L}(q, i\nu_{m''}, i\nu_{m'''})\mathbf{\Pi}_{ph}^{\Lambda}(q, i\nu_{m'''})\mathbf{V}_{\overline{ph}}^{\Lambda}(q, i\nu_{m'''}, i\nu_{m'})
\end{aligned} \tag{2.29b}$$

$$\begin{aligned}
\dot{\mathbf{\Phi}}_{pp}^{\Lambda,\ell,C}(q, i\nu_m, i\nu_{m'}) = -\sum_{i\nu_{m''}\, i\nu_{m'''}} & \mathbf{V}_{pp}^{\Lambda}(q, i\nu_m, i\nu_{m''})\mathbf{\Pi}_{pp}^{\Lambda}(q, i\nu_{m''}) \\
& \dot{\mathbf{I}}_{pp}^{\Lambda,\ell-2,L}(q, i\nu_{m''}, i\nu_{m'''})\mathbf{\Pi}_{pp}^{\Lambda}(q, i\nu_{m'''})\mathbf{V}_{pp}^{\Lambda}(q, i\nu_{m'''}, i\nu_{m'}) \,.
\end{aligned} \tag{2.29c}$$

The scale derivative of the two-particle irreducible vertex $\dot{I}_r^{\ell-2}$ here depends on the $\ell - 2$ flow equation as the equation involves in total two fermionic bubbles. A part of the central diagrams can be identified with the left (or respectively right) diagrams in Eq. (2.23)

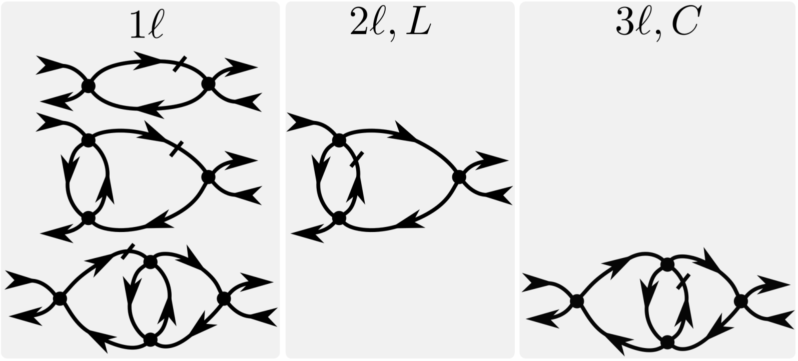

Figure 2.2: Example of 1ℓ-, 2ℓ- and 3ℓ-diagrams in the crossed particle-hole channel. In the 2ℓ-diagram, only the left contribution is shown and in the 3ℓ only the central. The dash on a Green's function indicates the scale derivative.

(or Eq. (2.24)) leading to numerically more convenient single loop equations

$$\begin{aligned}\dot{\mathbf{\Phi}}_{ph}^{\Lambda,\ell,C}(q,i\nu_m,i\nu_{m'}) = \sum_{i\nu_{m''}} \Big(&2\mathbf{V}_{ph}^{\Lambda}(q,i\nu_m,i\nu_{m''})\mathbf{\Pi}_{ph}^{\Lambda}(q,i\nu_{m''})\dot{\mathbf{\Phi}}_{ph}^{\Lambda,\ell-1,L}(q,i\nu_{m''},i\nu_{m'}) \\ &- \mathbf{V}_{\overline{ph}}^{\Lambda}(q,i\nu_m,i\nu_{m''})\mathbf{\Pi}_{ph}^{\Lambda}(q,i\nu_{m''})\dot{\mathbf{\Phi}}_{ph}^{\Lambda,\ell-1,L}(q,i\nu_{m''},i\nu_{m'}) \\ &- \mathbf{V}_{ph}^{\Lambda}(q,i\nu_m,i\nu_{m''})\mathbf{\Pi}_{ph}^{\Lambda}(q,i\nu_{m''})\dot{\mathbf{\Phi}}_{\overline{ph}}^{\Lambda,\ell-1,L}(q,i\nu_{m''},i\nu_{m'})\Big) \end{aligned} \tag{2.30a}$$

$$\dot{\mathbf{\Phi}}_{\overline{ph}}^{\Lambda,\ell,C}(q,i\nu_m,i\nu_{m'}) = -\sum_{i\nu_{m''}} \mathbf{V}_{\overline{ph}}^{\Lambda}(q,i\nu_m,i\nu_{m''})\mathbf{\Pi}_{ph}^{\Lambda}(q,i\nu_{m''})\dot{\mathbf{\Phi}}_{\overline{ph}}^{\Lambda,\ell-1,L}(q,i\nu_{m''},i\nu_{m'}) \tag{2.30b}$$

$$\dot{\mathbf{\Phi}}_{pp}^{\Lambda,\ell,C}(q,i\nu_m,i\nu_{m'}) = -\sum_{i\nu_{m''}} \mathbf{V}_{pp}^{\Lambda}(q,i\nu_m,i\nu_{m''})\mathbf{\Pi}_{pp}^{\Lambda}(q,i\nu_{m''})\dot{\mathbf{\Phi}}_{pp}^{\Lambda,\ell-1,L}(q,i\nu_{m''},i\nu_{m'}) \ . \tag{2.30c}$$

In Fig. 2.2, an example of a left flow diagram in the 2ℓ-truncation and a central flow diagram in the 3ℓ-truncation is compared to flow diagrams already contained in the 1ℓ-truncation.

Further, for the full reproduction of the Schwinger-Dyson equation (Eq. (3.2)) with the parquet approximated vertex, multiloop corrections for the self-energy flow equations have to be considered

$$\dot{\Sigma}^{\Lambda} = \dot{\Sigma}^{\Lambda,1\ell} + \dot{\Sigma}^{\Lambda,1} + \dot{\Sigma}^{\Lambda,2} \ . \tag{2.31}$$

The first correction

$$\dot{\Sigma}^{\Lambda,1}(k) = \int dp\, G^{\Lambda}(p)\Big[2\dot{I}_{ph,m\ell}^{\Lambda,C}(k,k,p) - \dot{I}_{ph,m\ell}^{\Lambda,C}(p,k,k)\Big] \,, \tag{2.32}$$

where $m\ell$ stands for the sum over all contributions from 3ℓ to $N_\ell\ell$, is proportional to the central ph-irreducible diagrams

$$\begin{aligned}\dot{I}_{ph,m\ell}^{\Lambda,C}(k_1,k_2,k_3) = \sum_{3\le\ell\le N_\ell}\sum_{n\,n'} \Big[& f_n(\mathbf{k}_1)f_{n'}^{*}(\mathbf{k}_4)\Big[\dot{\mathbf{\Phi}}_{pp}^{\Lambda,\ell,C}(k_1+k_3,i\nu_{m_1},i\nu_{m_4})\Big]_{n\,n'} \\ &+ f_n(\mathbf{k}_1)f_{n'}^{*}(\mathbf{k}_2)\Big[\dot{\mathbf{\Phi}}_{\overline{ph}}^{\Lambda,\ell,C}(k_3-k_2,i\nu_{m_1},i\nu_{m_2})\Big]_{n\,n'}\Big] \ . \end{aligned} \tag{2.33}$$

As the central diagrams are generated only at third loop order, the first self-energy flow correction does not contribute to loop orders below 3ℓ.

The second correction to the self-energy in the multiloop scheme is

$$\dot{\Sigma}^{\Lambda,2}(k) = -\int dp\, \delta S^{\Lambda}(p)\Big[2V^{\Lambda}(k,k,p) - V^{\Lambda}(p,k,k)\Big] \,, \tag{2.34}$$

where $\delta S^{\Lambda} = G^{\Lambda}\dot{\Sigma}^{\Lambda,1}G^{\Lambda}$. Also $\dot{\Sigma}^{\Lambda,2}$ does not contribute to loop orders below 3ℓ.

In the definition of the single-scale propagator with Katanin subsitution ∂G, also the corrections $\dot{\Sigma}^{\Lambda,1}$ and $\dot{\Sigma}^{\Lambda,2}$ should be entered. However, they depend on the vertex flow and are therefore not known when the single-scale propagator is calculated for the first time. At this point, the only possible solution is to self-consistently recalculate the multiloop from the beginning with the corrected self-energy flow in Eq. (2.31) as many times as it is needed to converge the self-energy multiloop corrections. This procedure is refered to as self-energy iteration.

Finally, we report the multiloop equations for the response functions. The fermion-boson vertex $\gamma_{3,\eta}^{\Lambda,l>1} = \gamma_{3,\eta}^{\Lambda,l,R} + \gamma_{3,\eta}^{\Lambda,l,C}$ obtains two corrections and the susceptibility $\chi_{\eta}^{\Lambda,l>1} = \chi_{\eta}^{\Lambda,l,C}$ only one. For a specific loop order, these corrections read

$$\begin{aligned}
\dot{\boldsymbol{\gamma}}_{3,\eta}^{\Lambda,\ell,R}(q,i\nu_m) &= -\sum_{i\nu_{m'}} \boldsymbol{\gamma}_{3,\eta}^{\Lambda}(q,i\nu_{m'})\mathbf{\Pi}_{\eta}^{\Lambda}(q,i\nu_{m'})\dot{\mathbf{I}}_{\eta}^{\Lambda,\ell-1}(q,i\nu_{m'},i\nu_m) && \text{(2.35a)}\\
\dot{\boldsymbol{\gamma}}_{3,\eta}^{\Lambda,\ell,C}(q,i\nu_m) &= \sum_{i\nu_{m'}\, i\nu_{m''}} \boldsymbol{\gamma}_{3,\eta}^{\Lambda}(q,i\nu_{m'})\mathbf{\Pi}_{\eta}^{\Lambda}(q,i\nu_{m'}) \\
&\qquad \dot{\mathbf{I}}_{\eta}^{\Lambda,\ell-2}(q,i\nu_{m'},i\nu_{m''})\mathbf{\Pi}_{\eta}^{\Lambda}(q,i\nu_{m''})\mathbf{V}_{\eta}^{\Lambda}(q,i\nu_{m''},i\nu_m) && \text{(2.35b)}\\
\dot{\boldsymbol{\chi}}_{\eta}^{\Lambda,\ell,C}(q) &= -\frac{1}{2}\sum_{i\nu_{m'}\, i\nu_{m''}} \boldsymbol{\gamma}_{3,\eta}^{\Lambda}(q,i\nu_{m'})\mathbf{\Pi}_{\eta}^{\Lambda}(q,i\nu_{m'})\dot{\mathbf{I}}_{\eta}^{\Lambda,\ell-2}(q,i\nu_{m'},i\nu_{m''}) \\
&\qquad \mathbf{\Pi}_{\eta}^{\Lambda}(q,i\nu_{m''})\boldsymbol{\gamma}_{3,\eta}^{\Lambda}(q,i\nu_{m''},i\nu_m) \,. && \text{(2.35c)}
\end{aligned}$$

These mfRG-flow equations depend again on the scale derivative of the vertex but not of the response functions themselves. As the loop order resolved $\dot{\gamma}_{3,\eta}^{\Lambda,\ell}$ and $\dot{\chi}_{\eta}^{\Lambda,\ell}$ is not needed, it is convenient to perform the summation over the loop order ℓ and consider directly $\dot{\gamma}_{3,\eta,m\ell}^{\Lambda,R} = \sum_{1<\ell\leq N_\ell} \dot{\gamma}_{3,\eta}^{\Lambda,\ell,R}$, $\dot{\gamma}_{3,\eta,m\ell}^{\Lambda,C} = \sum_{2<\ell\leq N_\ell} \dot{\gamma}_{3,\eta}^{\Lambda,\ell,C}$ and $\dot{\chi}_{\eta,m\ell}^{\Lambda} = \sum_{2<\ell\leq N_\ell} \dot{\chi}_{\eta}^{\Lambda,\ell,C}$. The latter are calculated directly through

$$\begin{aligned}
\dot{\boldsymbol{\gamma}}_{3,\eta,m\ell}^{\Lambda,R}(q,i\nu_m) &= -\sum_{i\nu_{m'}} \boldsymbol{\gamma}_{3,\eta}^{\Lambda}(q,i\nu_{m'})\mathbf{\Pi}_{\eta}^{\Lambda}(q,i\nu_{m'})\dot{\mathbf{I}}_{\eta,m\ell}^{\Lambda}(q,i\nu_{m'},i\nu_m) && \text{(2.36a)}\\
\dot{\boldsymbol{\gamma}}_{3,\eta,m\ell}^{\Lambda,C}(q,i\nu_m) &= -\sum_{i\nu_{m'}} \boldsymbol{\gamma}_{3,\eta}^{\Lambda}(q,i\nu_{m'})\mathbf{\Pi}_{\eta}^{\Lambda}(q,i\nu_{m'})\dot{\mathbf{\Phi}}_{\eta,m\ell}^{\Lambda,L}(q,i\nu_{m'},i\nu_m) && \text{(2.36b)}\\
\dot{\boldsymbol{\chi}}_{\eta,m\ell}^{\Lambda}(q) &= \frac{1}{2}\sum_{i\nu_{m'}} \dot{\boldsymbol{\gamma}}_{3,\eta,(m-1)\ell}^{\Lambda,R}(q,i\nu_{m'})\mathbf{\Pi}_{\eta}^{\Lambda}(q,i\nu_{m'})\boldsymbol{\gamma}_{3,\eta}^{\Lambda}(q,i\nu_{m'},i\nu_m) \,, && \text{(2.36c)}
\end{aligned}$$

where $\dot{I}_{\eta,m\ell}^{\Lambda} = \sum_{1\leq\ell<N_\ell} \dot{I}_{\eta}^{\Lambda,\ell}$, $\dot{\Phi}_{\eta,m\ell}^{\Lambda,L} = \sum_{1<\ell<N_\ell} \dot{\Phi}_{\eta}^{\Lambda,\ell,L}$ and $\dot{\gamma}_{3,\eta,(m-1)\ell}^{\Lambda,R} = \sum_{1<\ell<N_\ell} \dot{\gamma}_{3,\eta}^{\Lambda,\ell,R}$. Note that the summation range differs in $\dot{\gamma}_{3,\eta,(m-1)\ell}^{\Lambda,R}$ w.r.t. $\dot{\gamma}_{3,\eta,m\ell}^{\Lambda,R}$. With these simplifications, the flow equations for the response functions are composed by a 1ℓ- and a $m\ell$-part according

to

$$\dot{\gamma}^{\Lambda}_{3,\eta} = \frac{1}{2}\dot{\gamma}^{\Lambda,1\ell}_{3,\eta} + \frac{1}{2}\dot{\gamma}^{\Lambda,R}_{3,\eta,m\ell} + \dot{\gamma}^{\Lambda,C}_{3,\eta,m\ell} \tag{2.37a}$$

$$\dot{\chi}^{\Lambda}_{\eta} = \dot{\chi}^{\Lambda,1\ell}_{\eta} + \dot{\chi}^{\Lambda}_{\eta,m\ell} \, . \tag{2.37b}$$

Using this multiloop extension for self-energy, vertex and susceptibilities, the solution will satisfy by construction the Bethe-Salpeter equations for the two-particle reducible vertices, the Schwinger-Dyson equation for the self-energy (see Eq. (3.2)) and the equations connecting susceptibilities and vertices through the contraction of the latter

$$\boldsymbol{\chi}_{\eta}(q) = \sum_{i\nu_m} \mathbf{\Pi}_{\eta}(q, i\nu_m) \; + \sum_{i\nu_m\, i\nu_{m'}} \mathbf{\Pi}_{\eta}(q, i\nu_m)\mathbf{V}_{\eta}(q, i\nu_m, i\nu_{m'})\mathbf{\Pi}_{\eta}(q, i\nu_{m'}) \, . \tag{2.38}$$

These relations are numerically verified in this work.

2.3 Flow schemes

The flexibility of fRG to choose between different flow regulators or cutoffs can be seen as an advantage or as puzzle concerning the incomparable results obtained from different schemes. In the following, these two points of view will be discussed, the flow schemes used in this work are presented and it will be argued how the puzzle is lifted in the multiloop extension of fRG.

The flow scheme defines in which order the degrees of freedom are integrated out during the fRG flow. Therefore, different regulators yield critical scales with different physical interpretations and depending on the physics to describe, the appropriate flow scheme can be chosen. In the original idea of fRG an infrared cutoff which first integrates over the degrees of freedom far away from the Fermi-surface, is proposed. The momentum and the frequency cutoffs are typically infrared regulators which enter the single-particle propagator through

$$G^{\Lambda}_0(\mathbf{k}, i\nu_m) = R^{\Lambda}(\mathbf{k}, i\nu_m)G_0(\mathbf{k}, i\nu_m) \, , \tag{2.39}$$

where $R^{\Lambda_{\text{init}}}(i\nu_m, \mathbf{k}) = 0$ and $R^{\Lambda_{\text{final}}}(i\nu_m, \mathbf{k}) = 1$. The simplest form of the regulator would be a sharp momentum $R^{\Lambda}(i\nu_m, \mathbf{k}) = \theta(|\epsilon_{\mathbf{k}}| - \Lambda)$ or a sharp frequency cutoff $R^{\Lambda}(i\nu_m, \mathbf{k}) = \theta(|i\nu_m| - \Lambda)$. This work does not consider the momentum cutoff, as the inclusion of the self-energy can shift the Fermi-surface. An infrared regulating momentum cutoff would need to take this a priory unknown shift into account.

The here used frequency flow (Ω-flow) [53, 24] is implemented through the cutoff

$$R^{\Lambda}(\mathbf{k}, i\nu_m) = \frac{\nu_m^2}{\nu_m^2 + \Lambda^2} \, , \tag{2.40}$$

which is smeared out in order to facilitate numerical integration. The scale flows from $\Lambda_{\text{init}} \to \infty$ to $\Lambda_{\text{final}} = 0$. The evolution of the physical quantities with the scale Λ is very slow for large values and becomes much more sensitive at scales around unity. It is studied in Section 2.4.1, how the parametrization of the scale $\Lambda(t)$ w.r.t. the integration parameter t can speed up the numerical evaluation.

Other often used flow schemes are the regularizing temperature flow which gradually decreases temperature [48], and the interaction flow describing the change with increasing bare interaction [42]. The cutoff used in the latter is $R^{\Lambda}(\mathbf{k}, i\nu_m) = \Lambda$ leading to to the bare scale dependent propagator

$$G_0^{\Lambda}(i\nu_m, \mathbf{k}) = \Lambda G_0(i\nu_m, \mathbf{k}) \; , \tag{2.41}$$

where $\Lambda_{\text{init}} = 0$ and $\Lambda_{\text{final}} = 1$. While this flow scheme is not regularizing, it has the advantage that the result at each scale can be translated to the solution for a specific smaller bare vertex U. For a detailed study on this scaling property at each loop order, see Appendix B.

In 1ℓ fRG, the drawback of the freedom of choice is a large variety of solutions of the same model and method but different flow schemes. These differences are caused by the truncation of the infinite hierarchy of flow equations. If no truncation would be used, the flow schemes ultimately lead all to the same result. This is in particular the case for the multiloop fRG which, by construction, sums up all parquet diagrams with the correct weight [68]. As those are independent from the cutoff, this property extends to multiloop fRG. From this perspective, one can also argue, why the 1ℓ fRG is cutoff dependent. The 2ℓ and 3ℓ examples in Fig. 2.2 clearly depend on the cutoff scheme through the scale derivative of the propagator which finally reflects in numerically different solutions in 1ℓ fRG.

Furthermore, the starting point for the fRG flow does not necessarily have to be the free single-particle propagator. Also the DMFT solution can be used allowing to apply the method to stronger interactions [130, 120]. This requires a particular DMFT conserving flow scheme.

2.4 Implementation

In the following, some specific problems and solutions to the actual implementation are presented. For a general outline of the code structure, see also Fig. 2.3 for the 1ℓ-truncation and for the full multiloop fRG scheme the description below. The used objects and symbols are introduced in the specified subsections.

The computation of the fRG flow is preceded by a precalculation step in which the projection matrices from one channel (see Section 2.4.2) to another and the weight $\mathbf{W}(\mathbf{R})$ used in the calculation of the fermionic excitations (see Section 2.4.3) are initialized. Further, the indices in the objects are grouped according to symmetry relations allowing to reduce the calculation effort during the flow.

The core of the implementation is an ordinary differential equation solver for which the *ODEINT*-library of *boost* was used. In this work, the Runge-Kutta Cash-Karp method was chosen adopting further the adaptive integration possibility. Inside one Λ-step, first the self-energy is calculated using Eq. (2.11). Then, the self-energy iteration loop is opened and $\dot{\Sigma}$ is used for the Katanin substitution according to Eq. (2.20). With the resulting single-scale propagator, the fermionic excitations in Eqs. (2.17) and (2.26) (see Section 2.4.3) are calculated. Those are used in the calculation of 1ℓ-flow of the two-particle reducible vertices reported in Eq. (2.16). For each of the three channels, a low frequency vertex $\mathcal{R}_r$ and the corresponding asymptotics $\mathcal{K}_{1,r}$ and $\mathcal{K}_{2,r}$ are computed (see Section 2.4.2). Then, the fermion-boson vertex $\gamma_{3,\eta}$, its asymptotic $\gamma_{3\eta}^{a}$ and the susceptibilities χ_η are calculated according to the 1ℓ-flow equations in Eq. (2.18). After the evaluations of the 2ℓ-flow equations for the vertices and their asymptotics according to Eq. (2.23), the iteration over mfRG-loops is started. First, the right (Eq. (2.24)) and left (Eq. (2.23)) multiloop corrections are calculated and next, with the help of the latter, the central (Eq. (2.30))

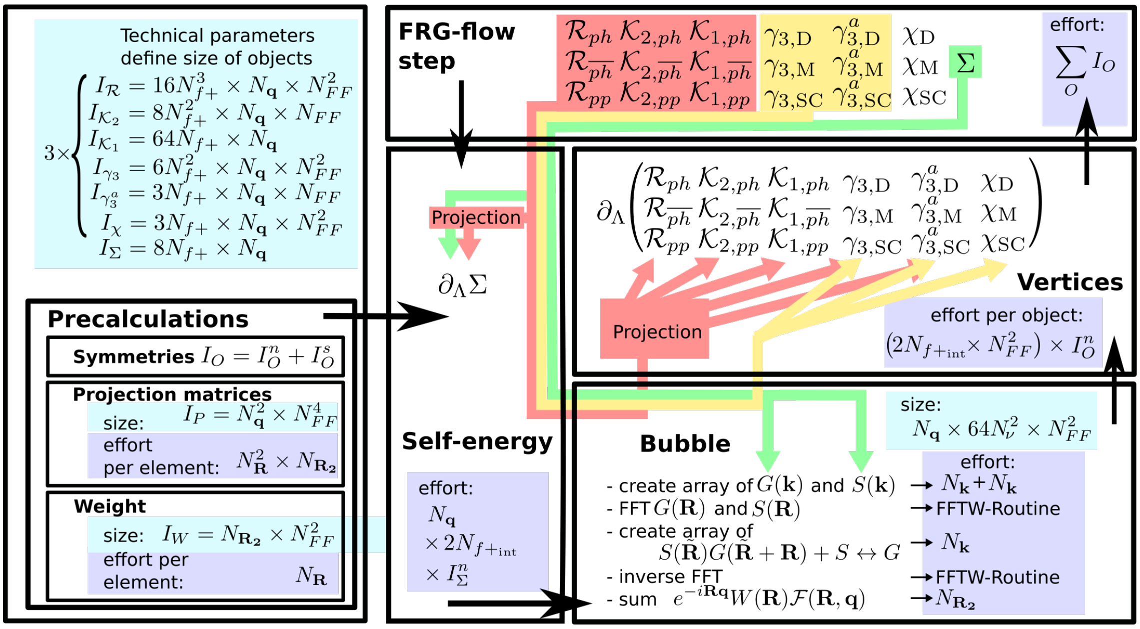

Figure 2.3: Summary of the code structure including information about object size, order of computation and object dependencies restricted to the 1ℓ-truncation. Also the numerical effort for each step is estimated. I_O denotes the number of elements in object O. It is defined by the number of positive fermionic frequencies of the rest function N_{f+}, the number of bosonic momentum patches $N_{\mathbf{q}}$, the number of form factors N_{FF}, the number of momentum/real space points for the Fast-Fourier Transform $N_{\mathbf{k}}$ and the number of frequencies $N_{f+_{\mathrm{int}}}$ in the integration of the fermionic excitation. The total number of elements I_O is reduced by the symmetries to I_O^n independent elements. The colored arrows indicate the feedback of the different objects: e.g. the rest-function and frequency asymptotics of the two-particle vertices (red) feed back into the self-energy through a projection to the fermionic notation and to the two-particle vertices themselves and the fermion-boson response function through a channel-channel projection. The feedback of the two-particle vertices to the susceptibilities is only indirect through the fermion-boson response function. The multiloop-extended version of the fRG program is not depicted. The multiloop iteration would take place inside the **Vertices**-box adding also the multiloop-equations for the self-energy. In addition, self-energy iteration would include both the **Vertices**-box and the **Bubble**-box.

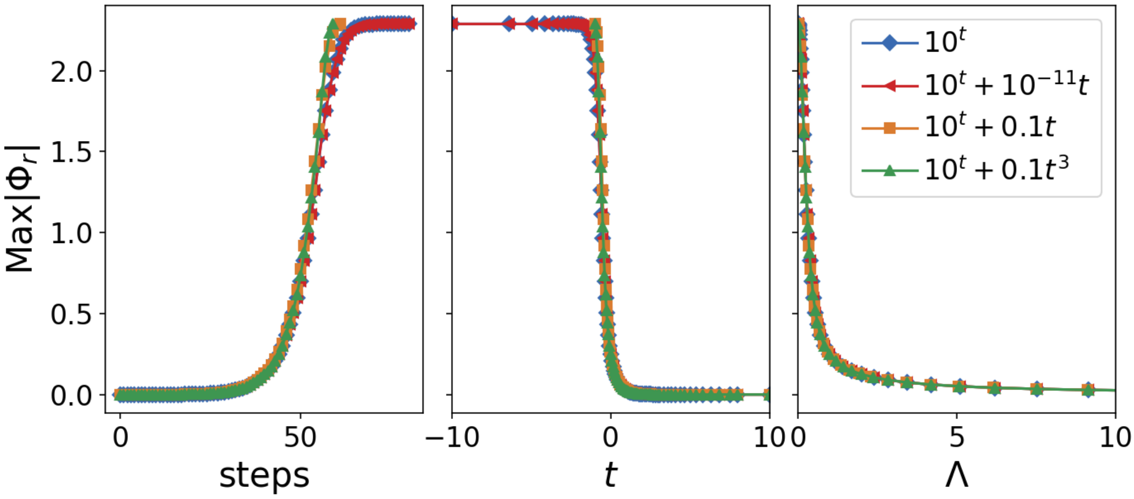

Figure 2.4: Maximal absolute value of the two-particle reducible vertices as a function of the adaptive integration step (left), the parametrization for the adaptive integration t (central) and the scale Λ (right) in the Ω-flow scheme with different parametrizations of the scale $\Lambda(t)$.

multiloop corrections. After each loop, a convergence criterion is applied and if the total and relative error on all objects is smaller than a threshold, or the maximum number of loops is reached, the loop is exited. After completion of the loop on the vertex corrections, the multiloop self-energy corrections according to Eqs. (2.32) and (2.34) are determined. The sum of all self-energy contributions from Eq. (2.31) is then compared to the previous self-energy iteration (or to the 1ℓ-self-energy for the first iteration). Again, if the total or relative error is smaller than a certain threshold or the maximal number of self-energy iterations is reached, the self-energy iteration is finished. Finally, the multiloop corrections of the response functions according to Eq. (2.36) are calculated. After the Λ-step is concluded, the change in all objects is returned to the differential equation solver, which then proposes the next scale Λ.

Within the Λ-step, the sum over multiloop corrections has to be tracked for the calculation of the multiloop correction of the self-energy, fermion-boson vertex and susceptibility. In total, $\dot{\mathbf{I}}^{\Lambda,C}_{ph,m\ell}$, $\dot{\mathbf{\Phi}}^{\Lambda,L}_{\eta,m\ell}$, and $\dot{\mathbf{I}}^{\Lambda}_{\eta,m\ell}$ have to be recorded for the last order and additionally $\dot{\mathbf{I}}^{\Lambda}_{\eta,m\ell}$ again for second to last loop order.

In Appendix A of [66] a pseudocode for the multiloop fRG is provided without the calculation of the response functions but keeping explicitly track on intermediate results and dependencies.

2.4.1 Parametrization of flow regulators

In Section 2.3, different flow schemes, among which the here used soft frequency cutoff and the non-regularizing interaction flow, were introduced. Advantages and disadvantages of the freedom of the scheme choice were discussed and it was pointed out that in the multiloop limit, all flow schemes finally lead to the same result. Not all of the data presented in this work are calculated in this limit, so it is worth to improve the flow schemes independently.

In this section, the focus lies on the numerical efficiency of the scale parametrization

$\Lambda(t)$. In the interaction flow, the vertices grow roughly linearly with the scale Λ. Therefore, the integration parameter t for the differential equation solver is conveniently proportional to the scale $\Lambda(t) = t$. In contrast, the scale $\Lambda(t)$ in the frequency flow extends over a large range covering very high values at which the flow is weak and low values at which it is very sensitive to scale changes. In order to integrate out the high-frequency regime faster and slowing down the flow at low frequencies, the natural relation between the scale and the integration parameter is

$$\Lambda(t) = 10^t \; . \tag{2.42}$$

The integration is started at $t_{\text{init}} = 10$ and ended at $t_{\text{final}} = -10$. The flow of the strongest two-particle channel, which in this case is $\Phi_{\overline{ph}}$, for the 2D Hubbard model at half-filling, $U = 2$ and $1/T = 5$ (technical parameters: $N_{f+} = 4$, $N_{q_x} = 12$), is shown in Fig. 2.4. In the left panel, the flow w.r.t. the performed integration steps is shown. Note that in the central (right) panel, the flow goes from large to small integration parameters t (frequency scales $\Lambda(t)$). The reason for the initially flat curve is the slow increase of the vertex functions at high energies and the adaptive differential equation solver expecting the solution to be of this order of magnitude (which could be presumably changed by the absolute integration error allowed to the solver). There is a steep increase about $t = 0$ (or $\Lambda(t) \approx 1$) and a second plateau for $t < 0$. In the following it is discussed how to decrease the second plateau at low frequencies. First, note that the flow according to Eq. (2.42) is never reaching $\Lambda_{\text{final}} = 0$. If a linear component $10^{-11}t$ is added, this final scale is exactly reached at $t = -10$ and the flow is not changed at all. Increasing the linearity factor to $0.1t$, the final scale is reached at $t_{\text{final}} = -1$ where the adaptive integration is stopped. With this choice, the plateau at low frequencies is shortened and the flow is concluded in 80% of the time needed of Eq. (2.42). The calculation time can be further decreased to 79% by

$$\Lambda(t) = 10^t + 0.1t^3 \; . \tag{2.43}$$

Note that the computation time depends also on the number of attempted but rejected integration steps of the solver. The optimal parametrization may finally depend also on the actual system to be solved.

2.4.2 Parametrization of the two-particle vertex

The vertex is a highly complex object depending on three frequencies, three momenta and in principle also spin and orbital degrees of freedom. While the spin degrees of freedom can be simplified using $SU(2)$-symmetry (compare [94] for an exhaustive elaboration of one- and two-particle vertex symmetries), the orbital degrees of freedom cannot be simplified without loss of generality. An attempt for an efficient approximation was made in [46] in particular designed for the constrained fRG approach. This work is restricted to the single particle case.

After the parquet decomposition in Eq. (2.4), the problem of an efficient frequency and momentum parametrization is shifted from the full two-particle vertex to the two-particle reducible vertices. This important task can be devided into two parts: the TU formulation of the momentum dependence and the decomposition of the vertices in high-frequency asymptotics and precise low-frequency structures. The two methods are combined, starting with the separation of the vertices into asymptotics and low frequency objects and subsequently expanding the remaining fermionic dependencies on the form factors from the TUfRG.

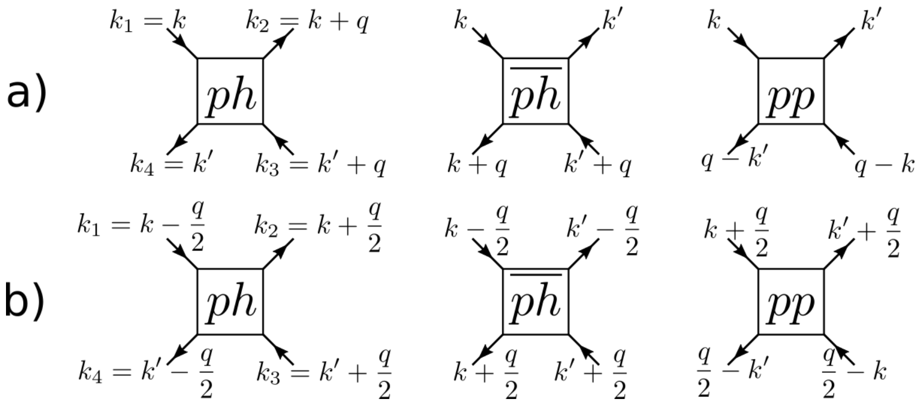

Figure 2.5: a) Non-symmetrized versus b) symmetrized notation for the two-particle vertices.

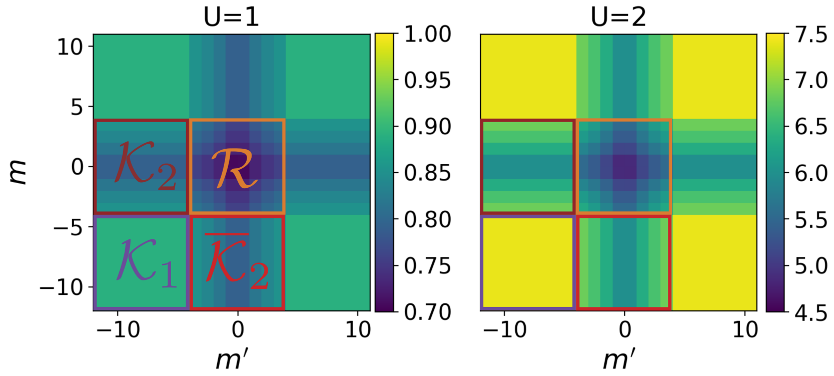

Figure 2.6: Crossed particle-hole irreducible vertex $\left[\mathbf{\Phi}_{\overline{ph}}(i\omega_l = 0, i\nu_m, i\nu_{m'}, \mathbf{q} = (\pi,\pi))\right]_{0\,0}$ in the 1ℓ-fRG with Katanin substitution for interaction strengths $U = 1$ and $U = 2$ and $1/T = 5$. The colored boxes indicate the frequency ranges used for the high-frequency asymptotics and low-frequency structure. The frequency structure is more pronounced for larger U and the overall values are larger.

Frequency asymptotics

In the numeric implementation of the frequencies, the symmetrized notation (compare Fig. 2.5) is used

$$\begin{aligned} V(i\nu_{m_1}, i\nu_{m_2}, i\nu_{m_3}) \approx U& \\ &+ \Phi_{ph}\left(i\omega_{m_2-m_1}, i\nu_{m_1+\left\lfloor\frac{m_2-m_1}{2}\right\rfloor}, i\nu_{m_4+\left\lfloor\frac{m_2-m_1}{2}\right\rfloor}\right) \\ &+ \Phi_{\overline{ph}}\left(i\omega_{m_3-m_2}, i\nu_{m_1+\left\lfloor\frac{m_3-m_2}{2}\right\rfloor}, i\nu_{m_2+\left\lfloor\frac{m_3-m_2}{2}\right\rfloor}\right) \\ &+ \Phi_{pp}\left(i\omega_{m_1+m_3+1}, i\nu_{m_1-\left\lceil\frac{m_1+m_3+1}{2}\right\rceil}, i\nu_{m_2-\left\lceil\frac{m_1+m_3+1}{2}\right\rceil}\right), \end{aligned} \tag{2.44}$$

where $i\omega_l = i2l\pi T$ is a bosonic and $i\nu_m = i(2m+1)\pi T$ a fermionic frequency. The floor and ceiling operations are needed in order to work with integer indices. Further, note that $-i\nu_m = i\nu_{-m-1}$ and $i\nu_{m_1} + i\nu_{m_2} = i\omega_{m_1+m_2+1}$.

In the symmetrized notation, for any fixed bosonic frequency one can observe a structure in the fermionic frequencies similar to the one shown in Fig. 2.6. In Ref. [129] similar plots with larger frequency windows show, that at large m and m', the two-particle reducible vertex of channel r only depends on the bosonic frequency $i\omega_l$. Therefore, a large portion of the information on the frequency dependence can be obtained already from the so-called *Kernel-1* function $\mathcal{K}_1(i\omega_l) = \lim_{\nu_m,\nu_{m'}\to\infty} \Phi(i\omega_l, i\nu_m, i\nu_{m'})$. For one small and one large fermionic frequency, the frequency dependence is corrected through the Kernel-2 functions $\mathcal{K}_2(i\omega_l, i\nu_m) = \lim_{\nu_{m'}\to\infty} \Phi(i\omega_l, i\nu_m, i\nu_{m'}) - \mathcal{K}_1(i\omega_l)$ and $\overline{\mathcal{K}}_2(i\omega_l, i\nu_{m'}) = \lim_{\nu_m\to\infty} \Phi(i\omega_l, i\nu_m, i\nu_{m'}) - \mathcal{K}_1(i\omega_l)$. The remaining dependency on all three frequencies, called *Rest*-function $\mathcal{R}(i\omega_l, i\nu_m, i\nu_{m'})$, is bounded to a small frequency window, which in the symmetrized notation is centered around $m = 0$ and $m' = 0$. This is the core advantage w.r.t. the non-symmetrized notation, where the center is shifted by $i\omega_l/2$ for finite bosonic frequencies.

Note that sending all frequencies to infinity, the bare interaction U is recovered. This is in particular also true for the fully two-particle irreducible vertex V_{2PIR}. With this observation it can be argued that the fermionic momentum dependency simplifies together with its corresponding fermionic frequency (compare Refs. [129, 131]).

Applying this frequency asymptotics based parametrization, the two-particle reducible vertices can be obtained for any frequency combination through

$$\begin{aligned}\Phi_r(\mathbf{q}, \mathbf{k}, \mathbf{k}', i\omega_l, i\nu_m, i\nu_{m'}) = \mathcal{R}_r(\mathbf{q}, \mathbf{k}, \mathbf{k}', i\omega_l, i\nu_m, i\nu_{m'}) +& \\ \mathcal{K}_{2,r}(\mathbf{q}, \mathbf{k}, i\omega_l, i\nu_m) + \bar{\mathcal{K}}_{2,r}(\mathbf{q}, \mathbf{k}', i\omega_l, i\nu_{m'}) + \mathcal{K}_{1,r}(\mathbf{q}, i\omega_l).& \end{aligned} \tag{2.45}$$

The flow of the different Kernels is implemented through the very same functions as in Eq. (2.16). The frequency limit to infinity is achieved by setting it to a large but finite value.

For the extension to the calculation of response functions, a frequency Kernel for the fermion-boson vertex can be defined analogously by $\gamma^a_{3,\eta}(i\omega_l) = \lim_{\nu_m\to\infty} \gamma_{3,\eta}(i\omega_l, i\nu_m)$.

In order to obtain converged observables at small frequencies, it is sufficient to restrict the calculation to a few low frequencies. Indeed, the rest function and asymptotics in Fig. 2.6 are not completely decayed but the frequency parametrization here yields converged results for the susceptibility. For an exemplary convergence study, see also Fig. 4.1 in Section 4.2.1.

Truncated-Unity fRG

While the expansion of the fermionic momentum dependencies of the vertex on form factors was already performed in [53, 52, 24, 79], the formalisation under the name of TUfRG was realized in [76]. The name comes from the insertion of the unity

$$\mathbb{1} = \int d\mathbf{p}' \sum_n f_n^*(\mathbf{p}') f_n(\mathbf{p}) \tag{2.46}$$

into the flow equations Eq. (2.13) and a truncation to only few form factors in the practical application. The definitions of the form-factor projected two-particle reducible vertices in Eq. (2.15) and the fermionic bubbles in Eqs. (2.17) and (2.26) follow naturally. While in Refs. [76, 87, 18] the form-factor convergence was explicitly studied, for the here presented results of the half-filled Hubbard model at $t' = 0$ only the s-wave form factor is considered. When going to finite doping or $t' \neq 0$, the d-wave form factor is added. The form factors implemented in the fRG-code are summarized in Table 2.1.

	n	$f_n(\mathbf{k})$	$f_n(\mathbf{R}_i, \mathbf{R}_j)$
LOC s-wave	0	1	$\delta_{j,i}$
1NN	1	$\sqrt{2}\cos(k_x)$	$\frac{1}{\sqrt{2}}(\delta_{j,i+x} + \delta_{j,i-x})$
	2	$\sqrt{2}\cos(k_y)$	$\frac{1}{\sqrt{2}}(\delta_{j,i+y} + \delta_{j,i-y})$
	3	$\sqrt{2}\sin(k_x)$	$\frac{i}{\sqrt{2}}(\delta_{j,i+x} - \delta_{j,i-x})$
	4	$\sqrt{2}\sin(k_y)$	$\frac{i}{\sqrt{2}}(\delta_{j,i+y} - \delta_{j,i-y})$
1NN d-wave	1	$\big(\cos(k_y) + \cos(k_x)\big)$	$\frac{1}{2}\big(\delta_{j,i+y} + \delta_{j,i-y} + \delta_{j,i+y} + \delta_{j,i-y}\big)$

Table 2.1: Local, first nearest-neighbor (full shell) and first nearest neighbor restricting on d-wave form factors both in momentum and real space representation. It is specified ih calculation which form factors are used. For a pure s-wave calculation only the local form factor (top) is used, for $s + d$-wave either the first two nearest neighbors form factors (center) or the d-wave form factor (bottom) are added, and a calculation with all nearest neighbors form factors takes into account the local (top) and the four 1NN (center) form factors.

Contrary to Ref. [76], we expand the non-symmetrized fermionic momenta on the form factors. This leads to a simpler translation symmetry. In the purely fermionic momentum space the latter is simply

$$\Phi(\mathbf{k}_1, \mathbf{k}_2, \mathbf{k}_3) = \Phi(\mathbf{k}_1 + \mathbf{K}, \mathbf{k}_2, \mathbf{k}_3) = \Phi(\mathbf{k}_1, \mathbf{k}_2 + \mathbf{K}, \mathbf{k}_3) = \Phi(\mathbf{k}_1, \mathbf{k}_2, \mathbf{k}_3 + \mathbf{K}) \tag{2.47}$$

with the reciprocal lattice vector $\mathbf{K} = i_x \times (2\pi, 0) + i_y \times (0, 2\pi)$. Also in the non-symmetrized momentum version (compare Fig. 2.5) the vertices are invariant under a reciprocal lattice vector shift in both bosonic and fermionic momenta

$$\begin{aligned} \Phi^{\mathrm{non-symm}}(\mathbf{q}, \mathbf{k}, \mathbf{k}') = \Phi^{\mathrm{non-symm}}(\mathbf{q} + \mathbf{K}, \mathbf{k}, \mathbf{k}') = \\ \Phi^{\mathrm{non-symm}}(\mathbf{q}, \mathbf{k} + \mathbf{K}, \mathbf{k}') = \Phi^{\mathrm{non-symm}}(\mathbf{q}, \mathbf{k}, \mathbf{k}' + \mathbf{K}) \; . \end{aligned} \tag{2.48}$$

On the contrary, the translation symmetry in the scheme with symmetrized momenta becomes more involved

$$\begin{aligned} \Phi^{\mathrm{symm}}(\mathbf{q}, \mathbf{k}, \mathbf{k}') = \Phi^{\mathrm{symm}}(\mathbf{q}, \mathbf{k} + \mathbf{K}, \mathbf{k}') = \\ \Phi^{\mathrm{symm}}(\mathbf{q}, \mathbf{k}, \mathbf{k}' + \mathbf{K}) = \Phi^{\mathrm{symm}}(\mathbf{q} + \mathbf{K}, \mathbf{k} + \frac{\mathbf{K}}{2}, \mathbf{k}' + \frac{\mathbf{K}}{2}) \; . \end{aligned} \tag{2.49}$$

In the latter version, the backfolding of the form-factor projected two-particle reducible vertex in bosonic momentum space involves a possible sign change

$$\big[\mathbf{\Phi}^{\mathrm{symm}}(\mathbf{q} + \mathbf{K})\big]_{n\,n'} = s_n s_{n'} \big[\mathbf{\Phi}^{\mathrm{symm}}(\mathbf{q})\big]_{n\,n'} \; , \tag{2.50}$$

where s_n is defined by $f_n(\mathbf{k} + \frac{\mathbf{K}}{2}) = s_n f_n(\mathbf{k})$ and can assume the value ± 1 for the form factors presented in Table 2.1.

As in the non-symmetrized notation, the form-factor projected vertex has the trivial backfolding property

$$\big[\mathbf{\Phi}^{\mathrm{non-symm}}(\mathbf{q} + \mathbf{K})\big]_{n\,n'} = \big[\mathbf{\Phi}^{\mathrm{non-symm}}(\mathbf{q})\big]_{n\,n'} \; , \tag{2.51}$$

it is more convenient for numerical implementation. A further issue of the symmetrized notation is the appearance of 'bosonic' real space vectors $\frac{\mathbf{R}_1 + \mathbf{R}_2}{2}$ in the real-space calculation of the fermionic bubble and projection matrices.

While the calculation of the fermionic excitation in the non-symmetrized momentum notation is discussed in Section 2.4.3, we focus in the following on the projection of one channel notation to another. The projection is needed in the calculation of the r.h.s. of Eq. (2.16), where the parquet decomposition of the vertex has to be inserted for in the correct channel projection $\mathbf{V}_r(q, i\nu_m, i\nu_{m'})$. The first contribution of the projections of the latter, is the projection of the fully two-particle irreducible vertex. In the parquet approximation it is approximated by the bare interaction, giving

$$\begin{aligned}[\hat{P}_{\to pp}[U](q, i\nu_m, i\nu_{m'})]_{n\,n'} &= [\hat{P}_{\to ph}[U](q, i\nu_m, i\nu_{m'})]_{n\,n'} \\ &= [\hat{P}_{\to \overline{ph}}[U](q, i\nu_m, i\nu_{m'})]_{n\,n'} = U\delta_{n,0}\delta_{n',0}\;. \end{aligned} \tag{2.52}$$

Next, each vertex includes also the two-particle reducible vertex in the channel of the notation (e.g. $\mathbf{\Phi}_{pp}(q, i\nu_m, i\nu_{m'})$ in $\mathbf{V}_{pp}(q, i\nu_m, i\nu_{m'})$) which does not need to be projected. Finally, there are two two-particle reducible channels in a different notation than the total vertex. The here needed projection from one channel to another has to be performed in frequency and momentum (or form-factor) space. The former leads to a comparatively simple linear combination of frequency arguments which can be found in Eq. (2.56).

In momentum space, the projection is more involved due to the form-factor dependence. Following the procedure of Ref. [76], we identify the projection matrices which describe the momentum translation from one channel to another using a matrix multiplication

$$\left[\hat{P}_{r'\to r}[\mathbf{\Phi}_{r'}](\mathbf{q}, i\omega_l, i\nu_m, i\nu_{m'})\right]_{n\,n'} = \sum_{m\,m',\mathbf{l}} A^{r\,r'}_{n\,n',m\,m'}(\mathbf{q},\mathbf{l})\left[\mathbf{\Phi}_{r'}(\mathbf{l},\ldots)\right]_{m\,m'}\;, \tag{2.53}$$

where $\ldots$ stands for a linear combination of frequency dependencies depending on the specific channels involved in the projection.

We exemplify the projection for the $\overline{ph}$-channel to the pp-channel. In momentum space, it reads

$$\begin{aligned}\left[\hat{P}_{\overline{ph}\to pp}[\mathbf{\Phi}_{\overline{ph}}](\mathbf{q}, i\omega_l, i\nu_m, i\nu_{m'})\right]_{n\,n'} &= \int d\mathbf{k}d\mathbf{k}' f^*_n(\mathbf{k})\; f_{n'}(\mathbf{k}')\times \\ \Phi_{\overline{ph}}\Big(\mathbf{q}-\mathbf{k}'-\mathbf{k}, \mathbf{k}, \mathbf{k}', i\omega_{(-m'-m-|l \bmod 2|-1)\equiv l'}, &i\nu_{m+\lceil\frac{l}{2}\rceil+\lfloor\frac{l'}{2}\rfloor}, i\nu_{m'+\lceil\frac{l}{2}\rceil+\lfloor\frac{l'}{2}\rfloor}\Big) \\ &= \sum_{\tilde{n}\,\tilde{n}'}\int d\mathbf{k}d\mathbf{k}' f^*_n(\mathbf{k})\; f_{n'}(\mathbf{k}')\; f_{\tilde{n}}(\mathbf{k})\; f^*_{\tilde{n}'}(\mathbf{k}')\times \\ \Big[\mathbf{\Phi}_{\overline{ph}}\Big(\mathbf{q}-\mathbf{k}'-\mathbf{k}, i\omega_{(-m'-m-|l \bmod 2|-1)\equiv l'}, &i\nu_{m+\lceil\frac{l}{2}\rceil+\lfloor\frac{l'}{2}\rfloor}, i\nu_{m'+\lceil\frac{l}{2}\rceil+\lfloor\frac{l'}{2}\rfloor}\Big)\Big]_{\tilde{n}\,\tilde{n}'}\;. \end{aligned} \tag{2.54}$$

We now transform the form factors to real space and shift the momentum dependence in order to get the matrix form of Eq. (2.53)

$$\begin{aligned}\left[\hat{P}_{\overline{ph}\to pp}[\mathbf{\Phi}_{\overline{ph}}](\mathbf{q}, i\omega_l, i\nu_m, i\nu_{m'})\right]_{n\,n'} &= \sum_{\tilde{n}\,\tilde{n}'}\int d\mathbf{K}\sum_{\mathbf{R}\mathbf{R_1}\mathbf{R_2}} e^{i\mathbf{l}\mathbf{R}-i\mathbf{q}\mathbf{R}} f^*_n(\mathbf{R}_1-\mathbf{R}) f_{n'}(\mathbf{R}_2+\mathbf{R})\times \\ f_{\tilde{n}}(\mathbf{R}_1) f^*_{\tilde{n}'}(\mathbf{R}_2)\Big[\mathbf{\Phi}_{\overline{ph}}\Big(\mathbf{l}, i\omega_{(-m'-m-|l \bmod 2|-1)\equiv l'}, &i\nu_{m+\lceil\frac{l}{2}\rceil+\lfloor\frac{l'}{2}\rfloor}, i\nu_{m'+\lceil\frac{l}{2}\rceil+\lfloor\frac{l'}{2}\rfloor}\Big)\Big]_{\tilde{n}\,\tilde{n}'}\;. \end{aligned} \tag{2.55}$$

The same procedure for every channel projection leads to the matrix equations

$$\begin{aligned}\Big[\hat{P}_{\overline{ph}\rightarrow pp}[\mathbf{\Phi}_{\overline{ph}}](\mathbf{q}, i\omega_l, i\nu_m, i\nu_{m'})\Big]_{n\,n'} &= \sum_{\tilde{n}\,\tilde{n}',\mathbf{l}} A^{pp,\overline{ph}}_{n\,n',\tilde{n}\,\tilde{n}'}(\mathbf{q},\mathbf{l})\times \\ &\Big[\mathbf{\Phi}_{\overline{ph}}\Big(\mathbf{l}, i\omega_{(-m'-m-|l \bmod 2|-1)\equiv l'}, i\nu_{m+\lceil\frac{l}{2}\rceil+\lfloor\frac{l'}{2}\rfloor}, i\nu_{m'+\lceil\frac{l}{2}\rceil+\lfloor\frac{l'}{2}\rfloor}\Big)\Big]_{\tilde{n}\,\tilde{n}'}\end{aligned} \tag{2.56a}$$

$$\begin{aligned}\Big[\hat{P}_{ph\rightarrow pp}[\mathbf{\Phi}_{ph}](\mathbf{q}, i\omega_l, i\nu_m, i\nu_{m'})\Big]_{n\,n'} &= \sum_{\tilde{n}\,\tilde{n}',\mathbf{l}} A^{pp,ph}_{n\,n',\tilde{n}\,\tilde{n}'}(\mathbf{q},\mathbf{l})\times \\ &\Big[\mathbf{\Phi}_{ph}\Big(\mathbf{l}, i\omega_{(m'-m)\equiv l'}, i\nu_{m+\lceil\frac{l}{2}\rceil+\lfloor\frac{l'}{2}\rfloor}, i\nu_{-m'-1+\lfloor\frac{l}{2}\rfloor+\lfloor\frac{l'}{2}\rfloor}\Big)\Big]_{\tilde{n}\,\tilde{n}'}\end{aligned} \tag{2.56b}$$

$$\begin{aligned}\Big[\hat{P}_{pp\rightarrow\overline{ph}}[\mathbf{\Phi}_{pp}](\mathbf{q}, i\omega_l, i\nu_m, i\nu_{m'})\Big]_{n\,n'} &= \sum_{\tilde{n}\,\tilde{n}',\mathbf{l}} A^{\overline{ph},pp}_{n\,n',\tilde{n}\,\tilde{n}'}(\mathbf{q},\mathbf{l})\times \\ &\Big[\mathbf{\Phi}_{pp}\Big(\mathbf{l}, i\omega_{(m+m'+|l \bmod 2|+1)\equiv l'}, i\nu_{m-\lfloor\frac{l}{2}\rfloor-\lceil\frac{l'}{2}\rceil}, i\nu_{m+\lceil\frac{l}{2}\rceil-\lceil\frac{l'}{2}\rceil}\Big)\Big]_{\tilde{n}\,\tilde{n}'}\end{aligned} \tag{2.56c}$$

$$\begin{aligned}\Big[\hat{P}_{\overline{ph}\rightarrow ph}[\mathbf{\Phi}_{\overline{ph}}](\mathbf{q}, i\omega_l, i\nu_m, i\nu_{m'})\Big]_{n\,n'} &= \sum_{\tilde{n}\,\tilde{n}',\mathbf{l}} A^{ph,\overline{ph}}_{n\,n',\tilde{n}\,\tilde{n}'}(\mathbf{q},\mathbf{l})\times \\ &\Big[\mathbf{\Phi}_{\overline{ph}}\Big(\mathbf{l}, i\omega_{(m'-m)\equiv l'}, i\nu_{m-\lfloor\frac{l}{2}\rfloor+\lfloor\frac{l'}{2}\rfloor}, i\nu_{m+\lceil\frac{l}{2}\rceil+\lfloor\frac{l'}{2}\rfloor}\Big)\Big]_{\tilde{n}\,\tilde{n}'}\end{aligned} \tag{2.56d}$$

$$\begin{aligned}\Big[\hat{P}_{pp\rightarrow ph}[\mathbf{\Phi}_{pp}](\mathbf{q}, i\omega_l, i\nu_m, i\nu_{m'})\Big]_{n\,n'} &= \sum_{\tilde{n}\,\tilde{n}',\mathbf{l}} A^{ph,pp}_{n\,n',\tilde{n}\,\tilde{n}'}(\mathbf{q},\mathbf{l})\times \\ &\Big[\mathbf{\Phi}_{pp}\Big(\mathbf{l}, i\omega_{(m+m'+|l \bmod 2|)\equiv l'}, i\nu_{m-\lfloor\frac{l}{2}\rfloor-\lceil\frac{l'}{2}\rceil}, i\nu_{m+\lceil\frac{l}{2}\rceil-\lceil\frac{l'}{2}\rceil}\Big)\Big]_{\tilde{n}\,\tilde{n}'}\end{aligned} \tag{2.56e}$$

$$\begin{aligned}\Big[\hat{P}_{ph\rightarrow\overline{ph}}[\mathbf{\Phi}_{ph}](\mathbf{q}, i\omega_l, i\nu_m, i\nu_{m'})\Big]_{n\,n'} &= \sum_{\tilde{n}\,\tilde{n}',\mathbf{l}} A^{\overline{ph},ph}_{n\,n',\tilde{n}\,\tilde{n}'}(\mathbf{q},\mathbf{l})\times \\ &\Big[\mathbf{\Phi}_{ph}\Big(\mathbf{l}, i\omega_{(m'-m)\equiv l'}, i\nu_{m-\lfloor\frac{l}{2}\rfloor+\lfloor\frac{l'}{2}\rfloor}, i\nu_{m'+\lceil\frac{l}{2}\rceil-\lceil\frac{l}{2}\rceil}\Big)\Big]_{\tilde{n}\,\tilde{n}'}\end{aligned} \tag{2.56f}$$

with the following projection matrices for the non-symmetrized notation

$$A^{pp,\overline{ph}}_{n\,n',\tilde{n}\,\tilde{n}'}(\mathbf{q},\mathbf{l}) = \sum_{\mathbf{R}\mathbf{R_1}\mathbf{R_2}} e^{i\mathbf{l}\mathbf{R}-i\mathbf{q}\mathbf{R}} f^*_n(\mathbf{R}_1-\mathbf{R}) f_{n'}(\mathbf{R}_2+\mathbf{R}) f_{\tilde{n}}(\mathbf{R}_1) f^*_{\tilde{n}'}(\mathbf{R}_2) \tag{2.57a}$$

$$A^{pp,ph}_{n\,n',\tilde{n}\,\tilde{n}'}(\mathbf{q},\mathbf{l}) = \sum_{\mathbf{R}\mathbf{R_1}\mathbf{R_2}} e^{i\mathbf{l}\mathbf{R}+i\mathbf{q}\mathbf{R}_2} f^*_n(\mathbf{R}_1-\mathbf{R}) f_{n'}(-\mathbf{R}_2-\mathbf{R}) f_{\tilde{n}}(\mathbf{R}_1) f^*_{\tilde{n}'}(\mathbf{R}_2) \tag{2.57b}$$

$$A^{\overline{ph},pp}_{n\,n',\tilde{n}\,\tilde{n}'}(\mathbf{q},\mathbf{l}) = \sum_{\mathbf{R}\mathbf{R_1}\mathbf{R_2}} e^{i\mathbf{l}\mathbf{R}-i\mathbf{q}\mathbf{R}} f^*_n(\mathbf{R}_1+\mathbf{R}) f_{n'}(\mathbf{R}_2-\mathbf{R}) f_{\tilde{n}}(\mathbf{R}_1) f^*_{\tilde{n}'}(\mathbf{R}_2) \tag{2.57c}$$

$$A^{ph,\overline{ph}}_{n\,n',\tilde{n}\,\tilde{n}'}(\mathbf{q},\mathbf{l}) = \sum_{\mathbf{R}\mathbf{R_1}\mathbf{R_2}} e^{i\mathbf{l}\mathbf{R}+i\mathbf{q}\mathbf{R}_2} f^*_n(\mathbf{R}_1-\mathbf{R}_2-\mathbf{R}) f_{n'}(-\mathbf{R}) f_{\tilde{n}}(\mathbf{R}_1) f^*_{\tilde{n}'}(\mathbf{R}_2) \tag{2.57d}$$

$$A^{ph,pp}_{n\,n',\tilde{n}\,\tilde{n}'}(\mathbf{q},\mathbf{l}) = \sum_{\mathbf{R}\mathbf{R_1}\mathbf{R_2}} e^{i\mathbf{l}(\mathbf{R_2}-\mathbf{R})+i\mathbf{q}\mathbf{R}} f^*_n(\mathbf{R}_1-\mathbf{R}) f_{n'}(\mathbf{R}-\mathbf{R}_2) f_{\tilde{n}}(\mathbf{R}_1) f^*_{\tilde{n}'}(\mathbf{R}_2) \tag{2.57e}$$

$$A^{\overline{ph},ph}_{n\,n',\tilde{n}\,\tilde{n}'}(\mathbf{q},\mathbf{l}) = \sum_{\mathbf{R}\mathbf{R_1}\mathbf{R_2}} e^{i\mathbf{l}\mathbf{R}+i\mathbf{q}\mathbf{R}_2} f^*_n(\mathbf{R}_1-\mathbf{R}_2-\mathbf{R}) f_{n'}(-\mathbf{R}) f_{\tilde{n}}(\mathbf{R}_1) f^*_{\tilde{n}'}(\mathbf{R}_2)\ . \tag{2.57f}$$

The patching of the bosonic momentum is in principle arbitrary as long as the fermionic excitation can be calculated on all patching points. As the latter are calculated through Fast-Fourier-Transform routines, they are known on a uniform grid of $N_{k_x} \times N_{k_x}$ patching points. The bubble can then be extracted on a less dense grid with $N_{q_x} \times N_{q_x}$ patching points, if $N_{k_x} = mN_{q_x}$ is an integer multiple of N_{q_x} (in this work usually $m = 5$).

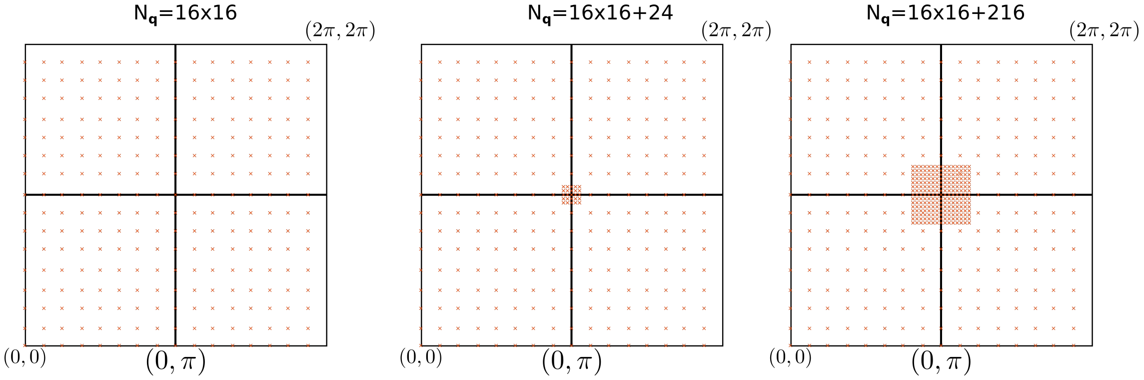

Figure 2.7: Patching points on the first Brillouin-zone with the same number of rough grid points $N_{q_x} = 16$, without (left), with small (central) and large (right) refined patching around $\mathbf{q} = (\pi, \pi)$.

Therefore, the bosonic momentum $\mathbf{q}$ of the vertices is also discretized on the regular grid defined by N_{q_x} which covers the whole Brillouin-zone. A more involved patching scheme is presented in the following.

Refined momentum grid for the antiferromagnetic peak

For the half-filled 2D Hubbard model, the magnetic susceptibility and vertex (or in the diagrammatic language ph- and $\overline{ph}$-vertex) exhibit a peak at the transfer momentum $\mathbf{q} = (\pi, \pi)$ (=M). When approaching pseudo-critical temperatures or interactions, the peak becomes higher and narrower while away from $\mathbf{q} = (\pi, \pi)$, the momentum dependency is rather flat. It is therefore convenient to sample the Brillouin-zone on a finer grid around the M-point. In the following, the possibility, implementation and impact of a refined momentum grid is discussed.

The flow equations in Eq. (2.16) allow for any selection of momentum patches as long as the fermionic bubbles and the full vertex are known on all points. The vertex involves the projection from one channel to another. The hence needed calculation of the projection matrices in Eq. (2.57) on an arbitrary momentum grid is possible as they depend analytically on the bosonic momentum. The only difference occurs in the momentum summation within the projection itself: Each contribution has to be accompanied by a corresponding weight factor depending on the size of the patch. The fermionic bubbles however can only be calculated on a regular momentum grid due the employment of Fast-Fourier-Transform routines (see Section 2.4.3). Usually, this grid is much finer than the bosonic patching grid. We can therefore add beneficial fine grid points to the list of bosonic patching points. For convenience, the refined patching region is chosen again rectangular, uniform, centered around $\mathbf{q} = (\pi, \pi)$ and with $(2l-1)m \times (2l-1)m$ patching points (where l is an integer and $m = N_{k_x}/N_{q_x}$). Patching points included in both the broad and fine grid are considered only once avoiding double counting. In Fig. 2.7, the momentum grids without refinement (left), with the smallest additional refinement defined by $l = 1$ and $m = 5$ (central) and an enlarged additional refinement defined by $l = 2$ and $m = 5$ (right) are presented.

The effect of the refined momentum grid can be observed in Fig. 2.8. For the 2D Hubbard model at half-filling, $t' = 0$, $U = 2$ and a relatively small temperature $T = 1/12$, the magnetic susceptibility was calculated using the smooth-frequency cutoff and the 1ℓ

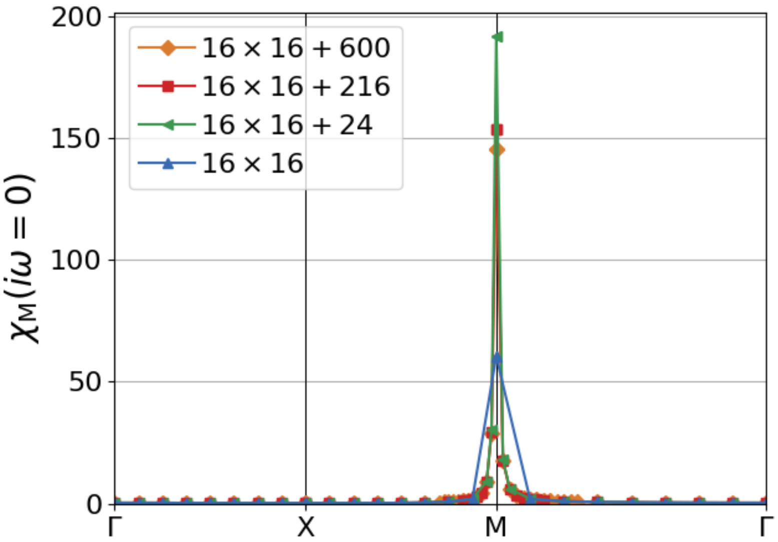

Figure 2.8: Magnetic susceptibility on the momentum path Γ-X-M-Γ as obtained using different patching refinements shown in Fig. 2.7 at half-filling, $t' = 0$, $U = 2$ and $1/T = 12$. The frequency-cutoff scheme and the 1ℓ-flow with Katanin substitution was applied.

flow with Katanin substitution. The peak at $\mathbf{q} = (\pi, \pi)$ is much higher with a better resolution. One can also observe that the narrow peak width is not correctly resolved without momentum refinement. With a larger refinement region (24 to 216 additional points), the peak shrinks again slightly. If the whole momentum structure is covered with the refined grid, an additional enlargement of the area (216 to 600 additional points) does not change the peak height substantially.

The effect of momentum discretization and in particular the size of the refined patching area, is discussed also in Section 5.2.1 in the framework of whether the pseudogap opening at the antinodal point occurs before the vertex diverges. The momentum grid dependence in Fig. 5.10 shows the importance of a versatile patching scheme.

Physical versus diagrammatic channels

The (m-)fRG equations for SU(2)-spin symmetric systems can be equally expressed in the physical and diagrammatic channels. Initially, the mfRG equations were obtained from argumentation in the diagrammatic channels [69] and shortly after from the derivation of the parquet equations again in the diagrammatic channels [66]. In Ref. [110], the mfRG equations are reported in the physical channels. The translation between diagrammatic and physical channels is shown explicitly in Appendix A.

In the implementation, the diagrammatic channels are used for the vertices and the physical channels for the response functions. In short, all vertex objects, including full, two-particle reducible and irreducible vertices, are translated from the diagrammatic to the physical channels via

$$\begin{aligned}\mathbf{V}_{\mathrm{D}}(q,i\nu_m,i\nu_{m'}) =&\mathbf{V}_{ph,\uparrow\uparrow,\uparrow\uparrow}(q,i\nu_m,i\nu_{m'})+\mathbf{V}_{ph,\uparrow\uparrow,\downarrow\downarrow}(q,i\nu_m,i\nu_{m'})\\ =&2\mathbf{V}_{ph}(q,i\nu_m,i\nu_{m'})-\mathbf{V}_{\overline{ph}}(q,i\nu_m,i\nu_{m'}) \qquad (2.58a)\\ \mathbf{V}_{\mathrm{M}}(q,i\nu_m,i\nu_{m'}) =&\mathbf{V}_{ph,\uparrow\uparrow,\uparrow\uparrow}(q,i\nu_m,i\nu_{m'})-\mathbf{V}_{ph,\uparrow\uparrow,\downarrow\downarrow}(q,i\nu_m,i\nu_{m'})\\ =&-\mathbf{V}_{\overline{ph}}(q,i\nu_m,i\nu_{m'}) \qquad (2.58b)\\ \mathbf{V}_{\mathrm{SC}}(q,i\nu_m,i\nu_{m'}) =&\mathbf{V}_{pp}(q,i\nu_m,i\nu_{m'}). \qquad (2.58c)\end{aligned}$$

where SU(2)-symmetry is used. In a second step, the singlet and triplet pairing vertices can obtained via [9]

$$\begin{aligned}\mathbf{V}_{\mathrm{singlet}} &= \mathbf{V}_{pp,\uparrow\downarrow,\downarrow\uparrow}(q,i\nu_m,i\nu_{m'})-\mathbf{V}_{pp,\uparrow\downarrow,\uparrow\downarrow}(q,i\nu_m,i\nu_{m'})\\ &= \mathbf{V}_{\mathrm{SC}}(q,i\nu_m,i\nu_{m'})+\hat{\mathbf{P}}^{\mathrm{crossing}}\mathbf{V}_{\mathrm{SC}}(q,i\nu_m,i\nu_{l-m'-1}) \qquad (2.59a)\\ \mathbf{V}_{\text{triplet-0}} &= \mathbf{V}_{pp,\uparrow\downarrow,\downarrow\uparrow}(q,i\nu_m,i\nu_{m'})+\mathbf{V}_{pp,\uparrow\downarrow,\uparrow\downarrow}(q,i\nu_m,i\nu_{m'})\\ &= \mathbf{V}_{\mathrm{SC}}(q,i\nu_m,i\nu_{m'})-\hat{\mathbf{P}}^{\mathrm{crossing}}\mathbf{V}_{\mathrm{SC}}(q,i\nu_m,i\nu_{l-m'-1}) \qquad (2.59b)\end{aligned}$$

where

$$\hat{\mathbf{P}}^{\mathrm{crossing}}_{n\,n',\tilde{n}\,\tilde{n}'}=\int d\mathbf{k}d\mathbf{k}'f^*_n(\mathbf{k})f_{n'}(\mathbf{k}')f_{\tilde{n}}(\mathbf{k})f^*_{\tilde{n}'}(\mathbf{q}-\mathbf{k}') \qquad (2.60)$$

and the matrix multiplication in Eq. (2.59) is over the second form-factor bilinear.

As explicitly seen in Appendix A, the projections from one channel to another is less complicated in the diagrammatic channels than in the physical channels. On the other hand, the instability analysis for diverging flows is more straightforward in the physical channels than in the diagrammatic ones.

2.4.3 Fermionic excitation

An efficient calculation of the (differentiated) fermionic particle-hole and particle-particle excitation defined in Eq. (2.17) and used in the flow equations of the vertex Eq. (2.16) is crucial for a fast fRG algorithm in particular when the self-energy feedback to the vertex is considered or a flow scheme different from the interaction flow is applied. In these cases, the calculation of the differentiated bubbles has to be performed at least for every Λ-step and, if included, once per self-energy iteration. When the self-energy feedback is neglected and the interaction flow is chosen, the bubbles reported in Eq. (2.26) at $\Lambda_f = 1$ can be calculated in advance and multiplied by the current scale Λ in order to obtain $\dot{\mathbf{\Pi}}^{\Lambda} = \Lambda\mathbf{\Pi}^{\Lambda_f}$. The full fermionic particle-hole and particle-particle excitation defined in Eq. (2.26) is used in the multiloop fRG and post-processing analysis. Contrary to the differentiated excitation, it is calculated only once per Λ-step. As the difficulties and solutions in the calculation are the same for the differentiated and full bubble, the following argumentation is only done on the latter. The differentiated bubble can be obtained by replacing $G(k)G(q\pm k)$ with $G(k)S(q\pm k)+S(k)G(q\pm k)$.

The fermionic bubbles in the symmetrized frequency notation read

$$\Big[\dot{\mathbf{\Pi}}_{ph}(\mathbf{q},i\omega_l,i\nu_m)\Big]_{n\,n'}=\int d\mathbf{p}f^*_n(\mathbf{p})f_{n'}(\mathbf{p})\;G(\mathbf{k},i\nu_{m-\lfloor\frac{l}{2}\rfloor})G(\mathbf{q}+\mathbf{k},i\nu_{m+\lceil\frac{l}{2}\rceil})\;, \qquad (2.61a)$$

$$\Big[\dot{\mathbf{\Pi}}_{pp}(\mathbf{q},i\omega_l,i\nu_m)\Big]_{n\,n'}=\int d\mathbf{p}f^*_n(\mathbf{p})f_{n'}(\mathbf{p})\;G(\mathbf{k},i\nu_{m+\lceil\frac{l}{2}\rceil})G(\mathbf{q}-\mathbf{k},i\nu_{\lfloor\frac{l}{2}\rfloor-m-1})\;. \qquad (2.61b)$$

At low temperatures, it is particularly important that the momentum summation is chosen to be fine enough. Recent works using the TUfRG [76, 87] have used an adaptive integration scheme for this purpose. They were able to reach both low temperatures and high wavevector resolutions.

For the present implementation, a refined adaptive integration turned out to be computationally challenging. Therefore it was replaced by an alternative efficient way of calculating the fermionic particle-hole and particle-particle bubbles exploiting the convolution theorem. Rewriting the Green's functions in real space, the bubbles can be calculated without momentum integration via

$$\Big[\dot{\mathbf{\Pi}}_{ph}(\mathbf{q}, i\omega_l, i\nu_m)\Big]_{n\,n'} = \sum_{\mathbf{R}} e^{i\mathbf{R}\mathbf{q}} W_{n\,n'}(\mathbf{R})\,\mathcal{F}\Big[G(-\tilde{\mathbf{R}}, i\nu_{m-\lfloor\frac{l}{2}\rfloor})G(\tilde{\mathbf{R}}-\mathbf{R}, i\nu_{m+\lceil\frac{l}{2}\rceil})\Big](\mathbf{q})\ , \tag{2.62a}$$

$$\Big[\dot{\mathbf{\Pi}}_{pp}(\mathbf{q}, i\omega_l, i\nu_m)\Big]_{n\,n'} = \sum_{\mathbf{R}} e^{-i\mathbf{R}\mathbf{q}} W_{n\,n'}(\mathbf{R})\,\mathcal{F}\Big[G(\tilde{\mathbf{R}}, i\nu_{m+\lceil\frac{l}{2}\rceil})G(\tilde{\mathbf{R}}+\mathbf{R}, i\nu_{\lfloor\frac{l}{2}\rfloor-m-1})\Big](\mathbf{q})\ , \tag{2.62b}$$

where $\mathcal{F}\Big[f(\tilde{\mathbf{R}})\Big](\mathbf{k})$ is the Fourier transform and the weight $W_{n\,n'}(R)$ is defined as

$$W_{n\,n'}(\mathbf{R}) = \sum_{\mathbf{R}'} f_n^*(\mathbf{R}')f_{n'}(\mathbf{R}+\mathbf{R}')\ . \tag{2.63}$$

The Green's function can be conveniently transformed to real space via Fast-Fourier-Transform (FFT) routines. The real-space expression of the form factors is provided in Table 2.1.

Eqs. (2.62) and (2.63) include an infinite sum over real space lattice points. Knowing that in TUfRG the real-space range of all form factors is finite, the sum can be truncated accordingly. The form-factor sum $f_n^*(\mathbf{R}')$ in Eq. (2.63) is zero when $\mathbf{R}'$ is outside of the form-factor range which defines the limit for the sum. Due to the form factor $f_{n'}(\mathbf{R}+\mathbf{R}')$, the weight $W_{n\,n'}(\mathbf{R})$ in Eq. (2.63) is zero for $\mathbf{R}$ larger than twice the range of the form factors. This information can be used in turn to constrain the summation in Eq. (2.62). For calculations including only the local form factor, all sums trivially reduce to a single contribution.

For a convenient translation to the bosonic momentum grid in the flow equations, the grid for the momentum and real space points used in the Fourier transformations should include the gridpoints on which the vertex is discretized. Nevertheless, especially at low temperatures, the Green's function momentum grid can and should be more dense in analogy to the adaptive integration. For converged results, the number of FFT-grid points $N_{\mathbf{k}}$ has to be examined in addition to the bosonic momentum grid size defined by $N_{\mathbf{q}}$ of the vertex.

3. Self-energy

The self-energy is an one-particle scattering amplitude describing the correction of the propagation of a particle due to interaction with other particles. It carries information on whether a material is conducting or insulating and is needed for a correct prediction of the spectral function which is proportional to the imaginary part of the Green's function and can be measured directly in with angleresolved photoemission spectroscopy (ARPES) and other scattering experiments.

From the functional viewpoint, the self-energy connects the free Green's function with the dressed Green's function through the Dyson-equation in Eq. (2.1). Through this dependency it enters in the calculation of the two-particle vertex and the response functions.

In fRG, the self-energy is calculated with the first flow equation of the hierarchy. Its contribution to the effective action is relevant, meaning that in a regularizing scheme, its importance increases during the flow of the scale Λ [82]. Of particular relevance is the self-energy induced shift of the Fermi-surface.

Firstly, the relation between the self-energy flow equation, as obtained by the fRG formalism, and the Schwinger-Dyson equation, which exactly connects the self-energy and the two-particle vertex (see Section 3.1), is discussed. As in the TU-fRG the form factor truncation destroys their equivalence even in the multiloop extension, a Schwinger-Dyson inspired flow scheme for the self-energy is introduced (see Section 3.2) in order to restore this property.

3.1 Relation of self-energy flow and Schwinger-Dyson equation

In the analysis of the conventional flow, the focus lies on the 1ℓ-truncation. The multiloop corrections, which contribute only to orders higher than $\mathcal{O}[U^3]$, do not change the following discussion. Assuming SU(2)-symmetry, the self-energy Σ^Λ is calculated via the differential equation

$$\dot{\Sigma}^\Lambda(k) = \sum_p \Big(2V^\Lambda(k,k,p) - V^\Lambda(p,k,k)\Big) S^\Lambda(p)\ . \tag{3.1}$$

In order to better understand its relation to the SDE, its computation in the TU-fRG scheme is specified subsequently. The Λ-dependent vertex is written in the purely fermionic notation as defined in Eq. (2.4). The summation over the momentum is performed over the finer momentum grid used also in the Fast-Fourier-Transform routines. For the bosonic momentum in Eq. (2.4), patching to the bosonic momentum grid of the vertex is needed, while the fermionic dependency is known analytically through the form factors in Table 2.1. This scheme only involves a single propagator, here the single-scale propagator S^Λ (and in the multiloop corrections Eqs. (2.32) and (2.34), the Green's function G^Λ).

On the other hand, the Schwinger-Dyson equation (SDE) for the self-energy

$$\begin{aligned}\Sigma(\mathbf{k}, i\nu_m) =& U \sum_{\mathbf{k}', i\nu_{m'}} G(\mathbf{k}', i\nu_{m'}) e^{\pm i\nu 0^+} \\ &- \sum_{\mathbf{k}',\mathbf{q}} \sum_{i\nu_{m'}, i\omega_l} V(\mathbf{k}, \mathbf{k}', \mathbf{k}'+\mathbf{q}, \mathbf{k}+\mathbf{q}, i\nu_m, i\nu_{m'}, i\nu_{m'+l}, i\nu_{m+l}) \\ &\quad G(\mathbf{k}', i\nu_{m'}) G(\mathbf{k}'+\mathbf{q}, i\nu_{m'+l}) G(\mathbf{k}+\mathbf{q}, i\nu_{m+l}) U \end{aligned} \tag{3.2}$$

is an exact self-consistent many-body relation connecting the self-energy and the vertex. In contrast to the conventional self-energy flow, it involves two fermionic loops over in total three Green's functions. It is used in the parquet approximation scheme [9, 95] for the self-consistent calculation of the self-energy alongside with the Bethe-Salpeter equations for the vertex (compare Section 4.3.1). In fRG, it is used as a consistency check for the results of the multiloop fRG flow (compare Section 4.2.3). In the so-called *post-processing* procedure, the vertex and self-energy at the final scale $\Lambda_{\text{fin.}}$ are inserted on the r.h.s. of Eq. (3.2) and the resulting self-energy is compared to the result of the flow. Formally, in the mfRG-scheme including also the multiloop self-energy corrections in Eqs. (2.32) and (2.34), the flowing self-energy and vertices fulfill the SDE at every scale Λ.

In TU-fRG, this is only true in the infinite form factor limit. In the following, the influence of the finite form factor truncation is explained and then an alternative scheme leading to finite form-factor SDE consistent solutions is proposed (see Section 3.2).

In TU-fRG, the SDE is best calculated by dividing it into different contributions through the insertion of the parquet decomposition Eq. (2.4) (with parquet approximation $V_{\text{2PIR}} \approx U$) leading to five different parts for the SDE

$$\Sigma(\mathbf{k}, i\nu_m) = \Sigma_G(\mathbf{k}, i\nu_m) + \Sigma_{GGG}(\mathbf{k}, i\nu_m) + \Sigma_{ph}(\mathbf{k}, i\nu_m) + \Sigma_{\overline{ph}}(\mathbf{k}, i\nu_m) + \Sigma_{pp}(\mathbf{k}, i\nu_m) \ , \tag{3.3}$$

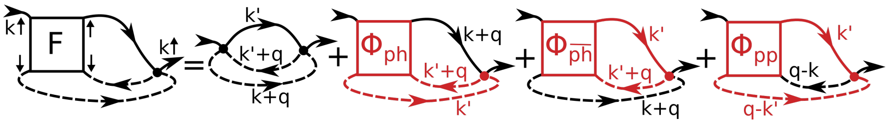

Figure 3.1: Second contributin on the r.h.s. of the Schwinger-Dyson equation (3.2) decomposed using the parquet approximation into channel specific parts. The first diagram on the r.h.s is calculated through Fast-Fourier-Transform. In the remaining three diagrams, the red colour indicates the principal channel. Solid (dashed) lines carry spin up (down).

where

$$\Sigma_G(\mathbf{k}, i\nu_m) = U \sum_{\mathbf{k}', i\nu_{m'}} G(\mathbf{k}', i\nu_{m'}) e^{\pm i\nu 0^+} \;, \tag{3.4a}$$

$$\Sigma_{GGG}(\mathbf{k}, i\nu_m) = -U^2 \sum_{\mathbf{k}'\mathbf{q}} \sum_{i\nu_{m'} i\omega_l} G^\Lambda(\mathbf{k}', i\nu_{m'}) G^\Lambda(\mathbf{k}+\mathbf{q}, i\nu_{m+l}) G^\Lambda(\mathbf{k}'+\mathbf{q}, i\nu_{m'+l}) \;, \tag{3.4b}$$

$$\Sigma_{ph}(\mathbf{k}, i\nu_m) = -\sum_{\mathbf{k}' i\nu_{m'}} \sum_n f_n^*(\mathbf{k}) f_0(\mathbf{k}) G^\Lambda(\mathbf{k}', i\nu_{m'}) \sum_{i\nu_{m''}} \Big[\mathbf{\Phi}^\Lambda_{ph}(\mathbf{k}'-\mathbf{k}, i\omega_{m'-m}, i\nu_{m+\lfloor \frac{m'-m}{2} \rfloor}, i\nu_{m''}) \mathbf{\Pi}^\Lambda_{ph}(\mathbf{k}'-\mathbf{k}, i\omega_{m'-m}, i\nu_{m''}) \mathbf{U} \Big]_{n\,0} \;, \tag{3.4c}$$

$$\Sigma_{\overline{ph}}(\mathbf{k}, i\nu_m) = -\sum_{\mathbf{k}' i\nu_{m'}} \sum_n f_n^*(\mathbf{k}) f_0(\mathbf{k}) G^\Lambda(\mathbf{k}', i\nu_{m'}) \sum_{i\nu_{m''}} \Big[\mathbf{\Phi}^\Lambda_{\overline{ph}}(\mathbf{k}'-\mathbf{k}, i\omega_{m'-m}, i\nu_{m+\lfloor \frac{m'-m}{2} \rfloor}, i\nu_{m''}) \mathbf{\Pi}^\Lambda_{ph}(\mathbf{k}'-\mathbf{k}, i\omega_{m'-m}, i\nu_{m''}) \mathbf{U} \Big]_{n\,0} \;, \tag{3.4d}$$

$$\Sigma_{pp}(\mathbf{k}, i\nu_m) = -\sum_{\mathbf{k}' i\nu_{m'}} \sum_n f_n^*(\mathbf{k}) f_0(\mathbf{k}) G^\Lambda(\mathbf{k}', i\nu_{m'}) \sum_{i\nu_{m''}} \Big[\mathbf{\Phi}^\Lambda_{pp}(\mathbf{k}'+\mathbf{k}, i\omega_{m'+m+1}, i\nu_{m-\lceil \frac{m'+m+1}{2} \rceil}, i\nu_{m''}) \mathbf{\Pi}^\Lambda_{pp}(\mathbf{k}'+\mathbf{k}, i\omega_{m'+m+1}, i\nu_{m''}) \mathbf{U} \Big]_{n\,0} \;, \tag{3.4e}$$

using the form factor expanded bare interaction $\mathbf{U}_{n\,n'} = U\delta_{n,0}\delta_{n',0}$.

The first term on the r.h.s. of the SDE in Eq. (3.2) is the so-called Hartree-term. It appears unchanged in Eq. (3.3) as it does only involve bare vertices. Its imaginary part is zero while the real part is constant in frequency and momentum. It can be absorbed in a shift of the chemical potential μ by $U\langle n\rangle/2$. Therefore, it is neglected in the calculations, although explicitly written down here.

The second term on the r.h.s of Eq. (3.2) is also represented graphically in Fig. 3.1. After the parquet decomposition of the vertex, the two-particle reducible vertices are accompanied by the corresponding fermionic bubble which substitutes two of the three Green's functions. The form factor truncation of the bubble does not introduce any further approximation. This decomposition is used also in the parquet and in Ref. [18] it is explicitly shown that although the same diagrams are summed up, a different combination of two-particle reducible vertices and fermionic excitations leads to different results.

The different approximation of equivalent diagrams is also the reason why the self-energy flow and the SDE lead to different results even in the multiloop extension of fRG (for numerical results see Sections 4.2.3 and 5.2.2). First, the form-factor approximation in the SDE-approach is studied. In order to see its effect, the vertex is expanded in the first orders of the bare interaction U and shown in Fig. 3.2. For simplicity, the self-energy corrections to the propagators are neglected. The first-order tadpole diagram (gray) on the r.h.s. is the Hartree-term. The second order diagram (red) is calculated using Fast-Fourier-transforms. This diagram is not associated to any specific channel. At third order, the colored boxes identify distinct diagrams coming from different channels (yellow for pp and green for $\overline{ph}$) for a better comparison with Fig. 3.3. The colored Green's functions show the order in which s-wave truncated excitations are inserted in the diagram. In this convention, the orange excitation is projected and inserted in the blue excitation which is finally closed by a single Green's function. The shown diagrams do not involve any inter-channel projection. Therefore, even the s-wave truncation is still completely correct and does not introduce approximations through translation. At higher order, the form factor truncation introduces quantitative approximations already on the vertex level.

For comparison, the corresponding diagrams produced by the conventional 1ℓ-flow of the self-energy are shown in Fig. 3.3. Here, the analysis is applied directly on the r.h.s. of the differential equations. For the full vertex, the parquet vertex is inserted, being aware that in the 1ℓ-approximation, this is only true up to second order. The diagrams are divided into contributions from the $V_{\uparrow\downarrow}$ (left) and $V_{\uparrow\uparrow}$ (right) vertex. This is more intuitive than presenting the same diagrams which can be obtained from the SU(2) symmetrized version of the flow equation. The gray boxes identify the tadpole diagrams, which are only partly shown in Fig. 3.2 but will be reproduced also there once the full self-energy correction to the Green's functions is inserted. The red diagrams correspond to the second order diagram in the SDE approach partly with inserted (gray) Katanin substitution for the single-scale propagator. There are three different form-factor approximations for the pure second order diagram, two on the first line of the $\uparrow\downarrow$- and one in the $\uparrow\uparrow$-contribution. Here, all three diagrams are still correctly approximated as the blue excitation has no other contribution than s-wave. At third order, there are five different from factor approximations contributing both to the pp-contribution (yellow) and the $\overline{ph}$-diagram (green). Here, only one of each group is approximated correctly with the s-wave truncation. For the pp-channel this would be the first yellow diagram and for the $\overline{ph}$-channel the last green diagram in the $\uparrow\downarrow$-collection.

In order to understand how the other diagrams are affected by approximations, the first green diagram of the $\uparrow\downarrow$-contribution in local s-wave form-factor truncation is considered. Here the yellow bubble is correctly approximated by the s-wave form factor while in the $\overline{ph}$-notation. But now it has to be translated into the pp-notation in order to be inserted into the blue bubble. In the s-wave truncation, this leads to averaging over the $\overline{ph}$-

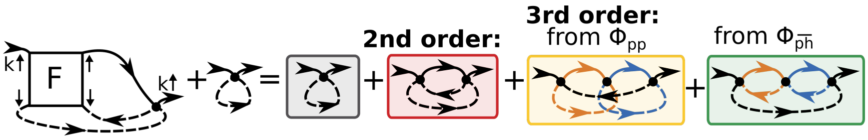

Figure 3.2: Lowest order diagrammatic contributions to the SDE self-energy flow. In order to facilitate the comparison to Fig. 3.3, the colored boxes group them into tadpole diagrams (gray boxes), 2nd order diagrams (red boxes) and two different types of 3rd order diagrams (yellow/green boxes). Self-energy corrections are neglected. Solid (dashed) lines carry spin up (down) and the orange bubbles are projected to the blue ones.

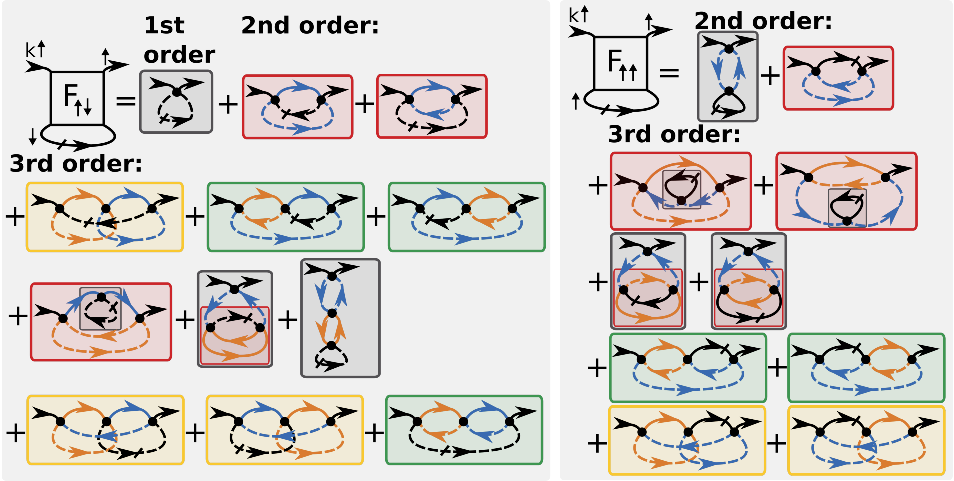

Figure 3.3: Conventional 1ℓ self-energy flow, with the $V_{\uparrow\downarrow}$ (left) and $V_{\uparrow\uparrow}$ (right) contribution. For the notation and color description, see Fig. 3.2. At third order, the form factor truncation approximates the diagrams from the same colour differently.

bosonic momentum and therefore information loss. In order to correctly resolve a peak in the bosonic momentum, a large number of form factors would have to be taken into account. Above all at perfect nesting (e.g. 2D Hubbard model, $t' = 0$ and half-filling), this convergence in form factor is impossible to achieve in practice.

3.2 Improved self-energy scheme for TU-fRG and TU-mfRG

Now, the second scheme for the calculation of the self-energy is introduced. It is inspired by the close relation of the Bethe-Salpeter equation for the vertex and the SDE for the self-energy to the multiloop fRG equations [66]. In particular, when deriving the SDE in Eq. (3.2) w.r.t. a flow parameter Λ, one can recover the 1ℓ-flow Eq. (3.1) together with the higher loop corrections in Eqs. (2.32) and (2.34). In this derivation the equivalence of different channel representations of the SDE-equation was used. As argued above, this is not possible in the TUfRG-approach. The restriction to a finite set of form factors in one channel will never allow to reproduce the full transfer momentum dependence in another channel.

Therefore, for the numerical equivalence between mfRG and parquet, it is convenient to retain the derivative of the SDE w.r.t. the scale Λ without further adaptation

$$\dot{\Sigma}(\mathbf{k}, i\nu_m) = \dot{\Sigma}_G(k, i\nu_m) + \dot{\Sigma}_{GGG}(k, i\nu_m) + \dot{\Sigma}_{ph}(k, i\nu_m) + \dot{\Sigma}_{\overline{ph}}(k, i\nu_m) + \dot{\Sigma}_{pp}(k, i\nu_m) \ , \tag{3.5a}$$

$$\dot{\Sigma}_G(\mathbf{k}, i\nu_m) = U \sum_{\mathbf{k}', i\nu_{m'}} \partial_\Lambda G^\Lambda(\mathbf{k}', i\nu_{m'}) \ , \tag{3.5b}$$

$$\dot{\Sigma}_{GGG}(\mathbf{k}, i\nu_m) = -U^2 \sum_{\mathbf{k}'\mathbf{q}} \sum_{i\nu_{m'} i\omega_l} \partial_\Lambda \Big(G^\Lambda(\mathbf{k}', i\nu_{m'}) G^\Lambda(\mathbf{k}+\mathbf{q}, i\nu_{m+l}) G^\Lambda(\mathbf{k}'+\mathbf{q}, i\nu_{m'+l}) \Big) \ , \tag{3.5c}$$

$$\dot{\Sigma}_{ph}(\mathbf{k}, i\nu_m) = -\sum_{\mathbf{k}' i\nu_{m'}} \sum_n f_n^*(\mathbf{k}) f_0(\mathbf{k}) \sum_{i\nu_{m''}} \partial_\Lambda \Bigg(G^\Lambda(\mathbf{k}', i\nu_{m'}) \Big[\mathbf{\Phi}_{ph}^\Lambda(\mathbf{k}'-\mathbf{k}, i\omega_{m'-m}, i\nu_{m+\lfloor \frac{m'-m}{2} \rfloor}, i\nu_{m''}) \mathbf{\Pi}_{ph}^\Lambda(\mathbf{k}'-\mathbf{k}, i\omega_{m'-m}, i\nu_{m''}) \mathbf{U} \Big]_{n\,0} \Bigg) \ , \tag{3.5d}$$

$$\dot{\Sigma}_{\overline{ph}}(\mathbf{k}, i\nu_m) = -\sum_{\mathbf{k}' i\nu_{m'}} \sum_n f_n^*(\mathbf{k}) f_0(\mathbf{k}) \sum_{i\nu_{m''}} \partial_\Lambda \Bigg(G^\Lambda(\mathbf{k}', i\nu_{m'}) \Big[\mathbf{\Phi}_{\overline{ph}}^\Lambda(\mathbf{k}'-\mathbf{k}, i\omega_{m'-m}, i\nu_{m+\lfloor \frac{m'-m}{2} \rfloor}, i\nu_{m''}) \mathbf{\Pi}_{ph}^\Lambda(\mathbf{k}'-\mathbf{k}, i\omega_{m'-m}, i\nu_{m''}) \mathbf{U} \Big]_{n\,0} \Bigg) \ , \tag{3.5e}$$

$$\dot{\Sigma}_{pp}(\mathbf{k}, i\nu_m) = -\sum_{\mathbf{k}' i\nu_{m'}} \sum_n f_n^*(\mathbf{k}) f_0(\mathbf{k}) \sum_{i\nu_{m''}} \partial_\Lambda \Bigg(G^\Lambda(\mathbf{k}', i\nu_{m'}) \Big[\mathbf{\Phi}_{pp}^\Lambda(\mathbf{k}'+\mathbf{k}, i\omega_{m'+m+1}, i\nu_{m-\lceil \frac{m'+m+1}{2} \rceil}, i\nu_{m''}) \mathbf{\Pi}_{pp}^\Lambda(\mathbf{k}'+\mathbf{k}, i\omega_{m'+m+1}, i\nu_{m''}) \mathbf{U} \Big]_{n\,0} \Bigg) \ , \tag{3.5f}$$

where the derivative w.r.t. Λ acts on the Green's function G^Λ, the two-particle reducible vertex Φ^Λ and the fermionic bubble Π^Λ. For each of Eqs. (3.5c) to (3.5f), three contributions are obtained, exemplified here by the ph-contribution

$$\begin{aligned}
&\dot{\Sigma}_{ph}(\mathbf{k}, i\nu_m) = \\
&\quad - \sum_{\mathbf{k}' i\nu_{m'}} \sum_{n} f_n^*(\mathbf{k}) f_0(\mathbf{k}) G^\Lambda(\mathbf{k}', i\nu_{m'}) \\
&\qquad\quad \sum_{i\nu_{m''}} \Big[\dot{\mathbf{\Phi}}^\Lambda_{ph}(\mathbf{k}'-\mathbf{k}, i\omega_{m'-m}, i\nu_{m+\lfloor\frac{m'-m}{2}\rfloor}, i\nu_{m''}) \mathbf{\Pi}^\Lambda_{ph}(\mathbf{k}'-\mathbf{k}, i\omega_{m'-m}, i\nu_{m''})\mathbf{U}\Big]_{n\,0} \\
&\quad - \sum_{\mathbf{k}' i\nu_{m'}} \sum_{n} f_n^*(\mathbf{k}) f_0(\mathbf{k}) G^\Lambda(\mathbf{k}', i\nu_{m'}) \\
&\qquad\quad \sum_{i\nu_{m''}} \Big[\mathbf{\Phi}^\Lambda_{ph}(\mathbf{k}'-\mathbf{k}, i\omega_{m'-m}, i\nu_{m+\lfloor\frac{m'-m}{2}\rfloor}, i\nu_{m''}) \dot{\mathbf{\Pi}}^\Lambda_{ph}(\mathbf{k}'-\mathbf{k}, i\omega_{m'-m}, i\nu_{m''})\mathbf{U}\Big]_{n\,0} \\
&\quad - \sum_{\mathbf{k}' i\nu_{m'}} \sum_{n} f_n^*(\mathbf{k}) f_0(\mathbf{k}) \dot{G}^\Lambda(\mathbf{k}', i\nu_{m'}) \\
&\qquad\quad \sum_{i\nu_{m''}} \Big[\mathbf{\Phi}^\Lambda_{ph}(\mathbf{k}'-\mathbf{k}, i\omega_{m'-m}, i\nu_{m+\lfloor\frac{m'-m}{2}\rfloor}, i\nu_{m''}) \mathbf{\Pi}^\Lambda_{ph}(\mathbf{k}'-\mathbf{k}, i\omega_{m'-m}, i\nu_{m''})\mathbf{U}\Big]_{n\,0} \,.
\end{aligned} \tag{3.6}$$

The first contribution of Eq. (3.6) depends on the Λ-derivative of the two-particle reducible vertex $\dot{\Phi}$. Therefore, it has to be evaluated after the flow equations for the channels. In the pure 1ℓ-scheme, $\partial_\Lambda G^\Lambda = S^\Lambda = \partial_\Lambda G^\Lambda|_{\Sigma=\text{const}}$ is the single-scale propagator and the self-energy change is not needed for the evaluation of the vertex flow. However, with the Katanin subsitution (or any higher loop order) the single-scale propagator is replaced by the scale derivative of the Green's function $\partial_\Lambda G^\Lambda = S^\Lambda + G^\Lambda \dot{\Sigma}^\Lambda G^\Lambda$. For the second part of $\partial_\Lambda G^\Lambda$, the self-energy change has to be known before the calculation of the vertex flow and, in the SDE-scheme, inside the self-energy flow itself. It is convenient to perform the first Katanin replacement with the self-energy change calculated via the 1ℓ-flow in Eq. (3.1). For a full feedback of the self-energy change, further iterations inside the Λ-step replacing Katanin with the self-energy change calculated Eq. (3.5a) should be performed. The number of the so-called self-energy iterations is specified by $N_{\Sigma\text{-iter}}$.

In principle, the argumentation why the conventional flow approximates the self-energy differently from the SDE in Section 3.1 applies also for the comparison of the Λ-derivative of the SDE and the conventional flow. The diagrams in Fig. 3.4 illustrate this directly on the level of the flow equation. The focus lies on two specific differentiated diagrams contributing to the flow of the self-energy. In the upper panel, the flow using the Λ-derivative of the SDE is represented. It is exemplified by the contribution of Eq. (3.5e) represented graphically in the second to last summand on the r.h.s. of Fig. 3.1. The lowest-order diagram for $\Phi_{\overline{ph}}$ is inserted, and the Λ-derivative is applied on the two spin-down propagators (dashed lines). The same contributions are part of the conventional fRG self-energy flow, shown in the lower panel of Fig. 3.4. The first diagram on the r.h.s. simply follows from a second-order $\Phi_{\overline{ph}}$ diagram with two $\overline{ph}$ bubbles, and the second diagram originates from the Φ_{pp} part of V, where the $\overline{ph}$ bubble (orange) is inserted into a pp bubble (blue). As argumented in Section 3.1, the r.h.s. of both panels are formally equivalent, but the form-factor truncation applies in a less favorable way on the right diagram in fRG (lower panel): Only the two diagrams in the upper panel and the first in the lower panel are exactly described by only s-wave form factors. However, when evaluating the lower right diagram in an s-wave form-factor truncation, the $\overline{ph}$ contribution is completely averaged in the process of translating it to the pp channel.

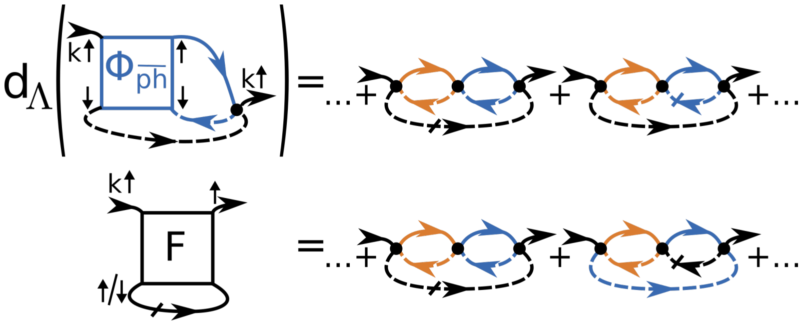

Figure 3.4: Illustration of the self-energy flows using the SDE-derivative, restricted to the part with $\Phi_{\overline{ph}}$ (upper panel), and conventional flow equations (lower panel). The r.h.s. shows two exemplary differentiated diagrams contributing to the self-energy flow at third order, where solid (dashed) lines carry spin up (down), and the diagonal dash symbolizes a scale-differentiated bare propagator. Using the SDE-derivative, two bubbles from the same channel (colored) are combined and then closed with the black line. By contrast, in the conventional flow, the second diagram requires to insert a $\overline{ph}$ (orange) into a pp (blue) bubble, before closing with the differentiated propagator (black).

It is emphasized that the two schemes, SDE-derivative and conventional flow, only give different results with a finite form-factor truncation. With a straight-forward patching of all three momentum dependencies on the very same grid, there is no loss of information in the projection from one channel to another. However, as the bosonic momentum needs a very fine grid close to the divergence of the magnetic channel, the numerical effort would be overwhelming. Also in TU-fRG, both schemes should converge to the same result with an increasing number of form-factors. This number might be as large as the bosonic patching points as it should describe correctly the projection of the magnetic peak to other channels. As the latter gets larger and narrower near the pseudocritical parameters, the SDE-flow scheme for the self-energy in the finite form-factor TU-fRG is the best compromise between accuracy and calculation effort.

When the SDE-flow scheme is used in the following, it is explicitly denoted either by fRG* in multiloop fRG (in contrast to fRG for the conventional self-energy flow) or by SDE in any loop truncation (in contrast to 1ℓ for the conventional self-energy flow).

4. Numerical consistency and results for the 2D Hubbard model

The following chapter is dedicated to the study of the convergence of the multiloop fRG and effect of the new SDE-like flow equation for the self-energy. The results presented here for the 2D Hubbard model can be taken as a guideline for applications of this method to different parameter regimes and models. It covers different aspects which should be taken into account to obtain quantitative predictions or, alternatively, help to estimate the accuracy of an approximate solution. Starting with the presentation of the 2D Hubbard model in Section 4.1, first the convergence of the fRG method is studied in Section 4.2.1. This is performed w.r.t. the parameters defining the description of the vertex, the loop number and self-energy iterations. Here, also the effect of different approximations is presented. The chapter is concluded with the comparison of fRG* w.r.t. PA and dQMC in Section 4.3, including different parameter regimes.

4.1 2D Hubbard model

Both for benchmark and the study of the pseudogap, the single-band Hubbard model in 2D is considered

$$\hat{\mathcal{H}} = \sum_{i,j,\sigma} t_{ij} \hat{c}^{\dagger}_{i\sigma} \hat{c}_{j\sigma} + U \sum_{i} \hat{n}_{i\uparrow} \hat{n}_{i\downarrow} - \mu \sum_{i,\sigma} \hat{n}_{i\sigma}, \tag{4.1}$$

where $\hat{c}^{(\dagger)}_{i\sigma}$ annihilates (creates) an electron with spin σ at the lattice site i, $t_{ij} = -t$ is the hopping between neighboring and $t_{ij} = -t'$ between next-nearest neighboring sites, μ the chemical potential, and U the on-site Coulomb interaction. The bare propagator is

$$G_0(\mathbf{k}, i\nu_m) = \Big(i\nu_m + \mu - \epsilon_{\mathbf{k}} \Big)^{-1} \tag{4.2}$$

with

$$\epsilon_{\mathbf{k}} = -2t(\cos k_x + \cos k_y) - 4t' \cos k_x \cos k_y \ . \tag{4.3}$$

It follows from Eq. (2.1) that the full propagator becomes

$$G(\mathbf{k}, i\nu_m) = \Big(i\nu_m + \mu - \epsilon_{\mathbf{k}} - \Sigma(\mathbf{k}, i\nu_m) \Big)^{-1}. \tag{4.4}$$

In the following the energy unit $t \equiv 1$ is used.

At half-filling, this model is known to generate large AF fluctuations with increasing correlation lengths for lower temperatures. Therefore, the following discussion focuses on the AF susceptibility in this case. For finite doping, other susceptibilities play a more important role. In particular at optimal doping and low temperatures, d-wave pairing is expected. The following calculations away from half-filling are therefore calculated with s- and d-wave form factors and the study of a larger variety of susceptibilities becomes interesting.

4.2 Convergence in internal parameters

Before turning to the benchmark w.r.t. other methods, we first study if the results are internally consistent.

The simplest check is to calculate a flow, first without and then with the exploitation of specific symmetries, then compare the final results. In order to save computation time, it is encouraged to approximate the interaction flow using the Euler integration with only few fixed steps. If the final result is equal, trivial mistakes spoiling the symmetries can be excluded.

In the following, the convergence of the multiloop fRG algorithm is studied w.r.t. the technical parameters. In Section 4.2.1, the focus lies on the vertex and self-energy parametrization through N_{f+} and $N_{\mathbf{q}}$ and in Section 4.2.3 on the parameters related to the multiloop extension of the fRG.

The convergence to a solution which does not change with a better parametrization is another indicator of internal consistency.

4.2.1 Convergence of vertex and self-energy parametrization

The parameterization of the vertex presented in Section 2.4 combines the TUfRG scheme [76] for the momentum dependence with the dynamical fRG implementation [129] for the extension to frequency dependent vertices. In order to illustrate its efficiency, a convergence study of the antiferromagnetic susceptibility χ_{AF} w.r.t. the number of Matsubara frequencies, momenta and form factors is shown here. The AF susceptibility was obtained by the 1ℓ-flow in Eq. (2.18b). As test system, the 2D Hubbard model at half-filling, $t' = 0$, $U = 2$ and a temperature far from pseudo-criticality $1/T = 4$ and of comparable value $1/T = 8$ is used.

In the left panel of Fig. 4.1 the convergence in the number of fermionic frequencies N_{f+} is shown. This number corresponds to the extension in positive fermionic frequencies of the rest-function $\mathcal{R}$ and all other frequency ranges are proportional to it. For $1/T = 4$ one observes no significant change of the susceptibility w.r.t. N_{f+}. The system at this temperature is only weakly correlated. Power counting arguments [31, 140] show that the frequency dependence of the vertex is less important. This is also shown numerically for small numbers of fermionic Matsubara frequencies, e.g., in Ref. [117]. At $1/T = 8$ the convergence w.r.t. N_{f+} is slower. According to our tolerance of 1% we obtain convergence at $N_{f+} = 8$.

In the right panel of Fig. 4.1, we analyze the dependence of the AF susceptibility on the number of bosonic patching points, $N_{\mathbf{q}}$. The data for $1/T = 4$ are already converged at $N_{\mathbf{q}} = 64$, while for $1/T = 8$ a large number of patches $N_{\mathbf{q}} = 256$ is needed. It can be concluded that near the pseudocritical temperature T_{pc}, the convergence is more sensitive to $N_{\mathbf{q}}$ than to N_{ν}. The reason are long-ranged AF fluctuations requiring an increasingly finer momentum resolution. An increase of the momentum patches is easier manageable than larger frequency windows, as the size of the objects to handle grows only linearly

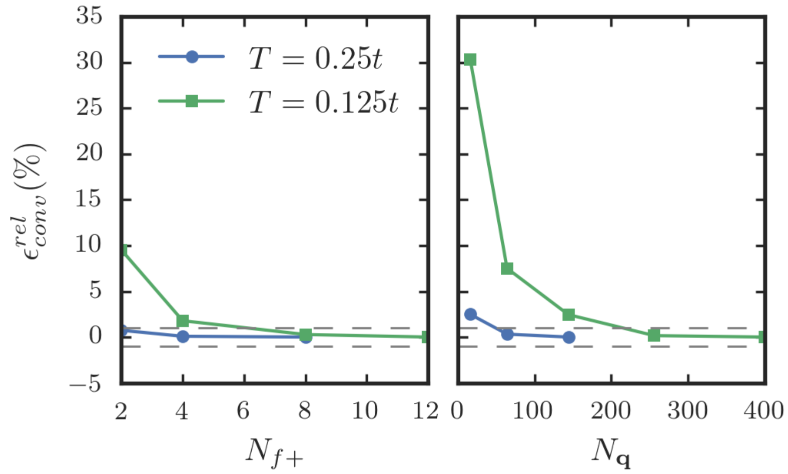

Figure 4.1: Convergence of the relative error $\epsilon_{conv}^{rel} = -(\chi - \chi_{conv})/\chi_{conv}$ of the (1ℓ) AF susceptibility for the half-filled 2D Hubbard model at $t' = 0$, $U = 2$ and different values of T. At $N_{\mathbf{q}}$=144 and $N_{\mathrm{FFT}} = 24 \times 24 = 576$ momentum patching points for the fast Fourier transform, the number of positive fermionic frequencies N_{f+} to obtain less than 1% deviation (dashed gray) is $N_{f+} = 4$ for $1/T = 4$ and $N_{f+} = 8$ for $1/T = 8$ (left). At $N_{FFT} = \max(576, 4 \times N_{\mathbf{q}})$ and $N_{f+} = 4$ for $1/T = 4$ and $N_{f+} = 8$ for $1/T = 8$, the number of bosonic momentum patches $N_{\mathbf{q}}$ needed for convergence is $N_{\mathbf{q}} = 8 \times 8$ for $1/T = 4$ and $N_{\mathbf{q}} = 16 \times 16$ (right).

with $N_{\mathbf{q}}$ while, at least for the rest-function $\mathcal{R}$, it scales with the third power in N_{f+} (compare Fig. 2.3). Moreover, the number of independent momentum patching points can be substantially reduced by exploiting point-group symmetries of the lattice.

The convergence w.r.t. the form factors is not explicitly shown here. It is expected for the half-filled 2D Hubbard model with $t' = 0$ and moderate coupling strength that only the s-wave form factor component of the vertex contributes strongly to the susceptibilities. Nevertheless, it was verified that, for all values of T considered, the AF response function does not change including also the first nearest neighbor form factors. Recent work with a Truncated Unity parquet solver [18] on the half-filled 2D Hubbard model with $U = 2$ and $1/T = 5$ shows that while the inclusion of the first nearest neighbor shell of form factors (5 form factors instead of 1) barely changes the AF susceptibility, the second nearest neighbor shell (9 form factors) leads to results changing by slightly more than 1%. While this convergence issue should be similar in fRG, the small quantitative correction does not justify the big additional computational effort (being $9 \times 9 \times 9 \times 9$ times larger).

4.2.2 Effect of different approximations

Before turning to the multiloop implementation it is worth to take a step back and study the effect of different vertex approximations already at the 1ℓ-level with conventional self-energy flow. Artificially suppressing the frequency dependence of the interactions or neglecting the self-energy allow to gain a better understanding of the interplay of the different interaction channels and the role of the self-energy.

Four approximation levels are shown in Fig. 4.2 in terms of the inverse AF susceptibility as a function of temperature. The "full fRG" refers to the TUfRG scheme with an efficient

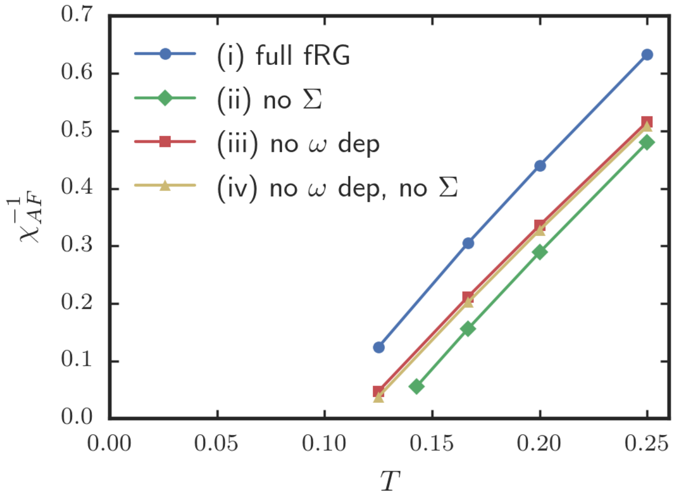

Figure 4.2: Inverse (1ℓ) AF susceptibility at $\mathbf{q} = (\pi, \pi)$ as a function of temperature, for $U = 2$. Besides the curve obtained using the full TU dynamical fRG scheme (blue dots), different approximations are shown: neglecting the self-energy feedback (green diamonds), using a frequency independent vertex (red squares) and the combination of the previous two approximations (yellow triangles).

inclusion of the vertex dynamics and self-energy inclusion. Approximation “no Σ” denotes the flow with a frequency-dependent effective interaction but without the feedback of the self-energy; “no ω dep” represents the static approximation for the effective interaction and the self-energy, in which the fermion-fermion, fermion-boson and boson-boson vertices are approximated by their value at zero frequency leading to frequency independent vertex; and “no ω dep, no Σ” combines the neglect of the self-energy feedback with a static approximation for the vertices.

In all approximations, the inverse AF susceptibility decreases quite linearly, i.e., Curie-Weiss-like, upon lowering T. The intersection of the curve with the abscissa marks the pseudocritical temperature. In the 1ℓ fRG scheme, it assumes a finite value, violating the Mermin-Wagner theorem. One can observe that the full TU-dynamic fRG approach leads to larger inverse AF susceptibilities, or smaller χ_{AF}, than the other three approximations, shifting T_{pc} to a smaller value.

It is to be expected, that the calculation without self-energy flow diverges at higher T_{pc} w.r.t. the full one as the self-energy renormalizes the leading vertices and therefore also susceptibilities, in accordance with the fRG studies in [24, 122]. The AF susceptibility is therefore smaller with self-energy feedback and T_{pc} becomes lower. For a detailed discussion on the pseudocritical temperatures on a wider range of parameters, we refer the reader to Ref. [24] and [52].

The flow variants with static interactions “no ω dep” differ only slightly upon neglecting the self-energy feedback. The reason for this is that using a static two-particle vertex also the self-energy becomes frequency independent. Considering that because of the complex conjugation relation $\Sigma^*(\mathbf{k}, i\nu_m) = \Sigma(\mathbf{k}, -i\nu_m)$ the imaginary part of the self-energy is antisymmetric in the frequency, the latter cancels. The only difference between “no ω dep” and “no ω dep, no Σ” is therefore the inclusion of a frequency independent real part of the self-energy. The increase in the pseudocritical temperature upon neglecting the self-energy feedback in a static calculation was already observed in Ref. [117]. The small difference may come from the real part of the self-energy that can be understood as upward-renormalization of the hopping parameter, or equivalently a downward-renormalization of the density of states. Furthermore, Ref. [16] shows that the effect of the self-energy inclusion in a static vertex approximation depends on the filling of a t-t' Hubbard model.

Compared to the fRG flow scheme with frequency dependent vertex, the AF tendencies in the static flow “no ω dep” are stronger. In the latter, the leading two-particle vertex is overestimated as its static component is the strongest. This leads to larger AF susceptibilities. Without self-energy feedback the picture is inverted. As the particle-particle process is approximated by its static and therefore strongest part its screening on the particle-hole susceptibilities increases and the static approximation leads to larger inverse AF susceptibilities in the self-energy neglecting approximation. This was found also by Ref. [52] and [24] for different next-to-nearest neighbor hoppings t'/t and van Hove filling. Another study including self-energy feedback in Ref. [16] observes that, with finite t' and over a large range of doping, the dynamic case yields higher pseudo-critical scales than the static one. In general, the two opposite effects described above are competing against each other if the frequency dependence is neglected. The net effect depends on the self-energy scheme and parameter regime.

In many previous works, the approximation without frequency dependence and self-energy feedback was used, as the frequency dependence perpendicular to the Fermi surface is irrelevant in the RG sense and neglecting the self-energy feedback simplies the fRG scheme [82]. Various other fRG works have already explored the changes occurring by using better approximations. Earlier studies of the self-energy without explicit frequency dependence of the effective interaction pointed to the possibility of non-Fermi liquid behavior first without [58] and later with self-energy feedback [92]. Channel-decomposed fRG [52, 24] and N-patch fRG [117] were used to explore the effects of a frequency-dependent effective interaction and of the self-energy feedback. Their results are consistent with the ones in Fig. 4.2.

The closest approach to the one denoted by full fRG can be found in Ref. [122]. They used a refined 1ℓ scheme and studied the role of the various frequency structures in the interaction, parametrized by three frequencies. They argued that a one-frequency parametrization can in some cases lead to spurious instabilities. The implementation used here, differs from this work by the possibility to extend the truncation to more form factors, a more economic description of the higher frequencies, and the implementation of the multiloop corrections.

4.2.3 Convergence in loop numbers and self-energy iterations

In the following, the convergence w.r.t. the number of loops as well as the effect of the self-energy iterations is studied. It is recalled that in fRG the conventional (multiloop) flow equations for the self-energy were used while in fRG* the SDE-flow scheme was adopted.

For a specific mfRG-calculation, the maximal number of loops can be fixed but an internal convergence condition allows to exit the loop also before. The advantage of this additional convergence check can be understood from Fig. 4.3 which shows the actual number of used loops $\#\ell$ as a function of the integration parameter t. In the frequency flow (left panel), few loops are sufficient at the beginning of the flow (large positive t) and the very end of the flow (large negative t). Around $\Lambda = e^t = 1$, the number of used loops increases rapidly. The number of maximally allowed loop orders 24 is hit for all shown interaction strengths. While the number of executed loops decreases for the

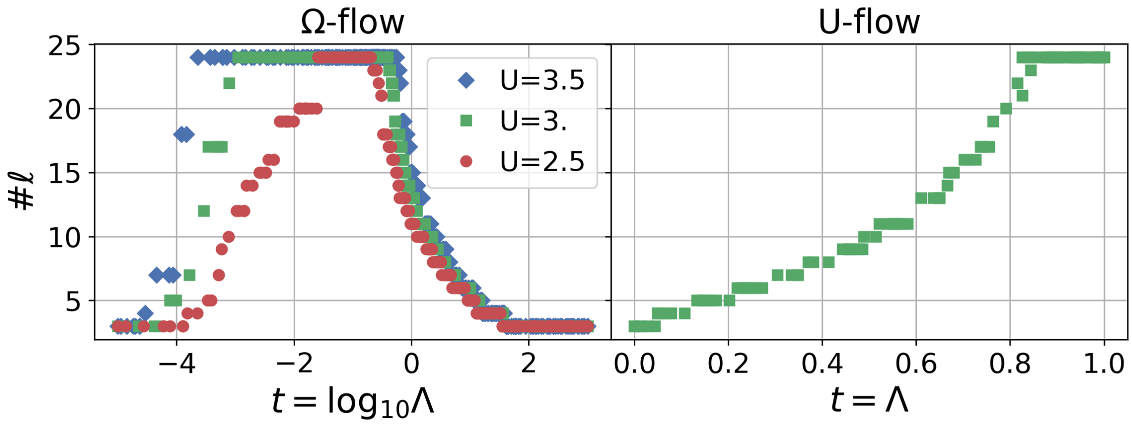

Figure 4.3: Number of loops used during the flow as a function of the integration parameter t. The smooth frequency cutoff (left panel, flow from right to left) needs many loop orders around $\Lambda = 1$ ($t = 0$) and the interaction cutoff (right panel, flow from left to right) towards the end of the flow $\Lambda \to 1$. The integration region in which the maximal number of loops allowed $N_\ell = 24$ is hit increases for higher interaction values.

smaller $U = 2.5$ already around $t = -2$ for the largest $U = 3.5$ considered here, the decrease occurs only at the very end of the frequency flow. It is clear from this plot, that for a full loop convergence, the maximally allowed number of loops N_ℓ should be increased even further even if the final result for the susceptibilities might be already very close to the converged one.

Also the interaction flow needs only few loops in the beginning (small integration parameters t). The number of executed loops grows almost linearly until the maximal value of loops is reached. Contrary to the frequency flow, it does not decrease at the end of the flow (large integration parameters t). This behavior could be expected as larger integration parameters translate into larger bare interactions U (see Appendix B).

In Fig. 4.4, the contribution to the r.h.s. of the Kernel function

$$\dot{\mathcal{K}}^{\Lambda,\ell}_{1,\mathrm{AF}} = \lim_{\nu_m,\nu_{m'}\to\infty} \left[\dot{\mathbf{\Phi}}^{\Lambda,\ell}(\mathbf{q} = (\pi,\pi), i\omega_l = 0, i\nu_m, i\nu_{m'})\right]_{0\,0} = 2\dot{\chi}^{\Lambda,\ell}_{\mathrm{AF}} U^2 \tag{4.5}$$

is shown as a function of loop order (starting with $\ell = 3$). Apart from the factor U^2, this functional corresponds to the AF susceptibility (see Appendix C in [110]). The different lines correspond to different scales. While in the lower panel, $\dot{\mathcal{K}}^{\Lambda,\ell}_{1,\mathrm{AF}}$ is shown for all scales, the top panels select specified values. The characteristic multiloop oscillations can be observed here already at the level of the differential equation. At the parameters considered, $U = 3$ and $1/T = 5$, the amplitude decreases quickly at low loop numbers and then converges slowly to zero. With increasing interaction, the initial amplitude is of a similar height, but its damping is much weaker (not shown). If the damping of the amplitude vanishes or the latter even increases, the multiloop fRG will not converge with loop order. At this point, a strong-coupling many-body method should be preferred.

It is remarkable, that the oscillation period does not depend much on the scale (see Fig. 4.4) or even the interaction strength (not shown). The reason for this is not yet discovered but if it proves to be a general feature, it might be used for a more efficient summation of the loop orders.

The final loop order study is shown in Fig. 4.5 where the AF susceptibility is shown for calculations with increasing maximally allowed loop order N_ℓ. The solid lines show

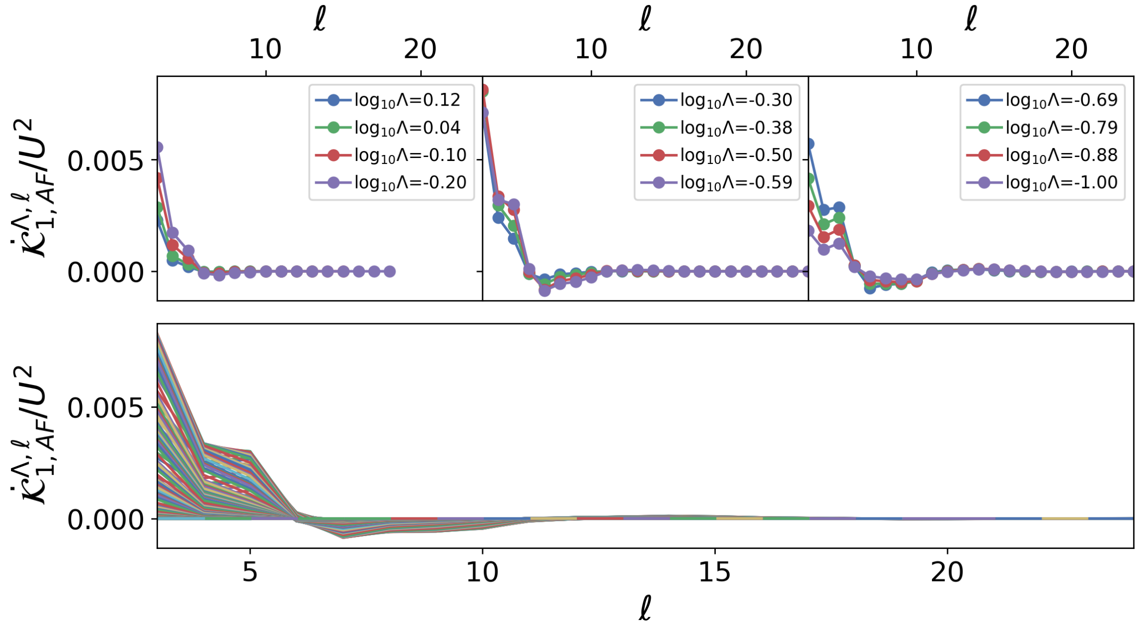

Figure 4.4: R.h.s of $\dot{K}^{\Lambda,\ell}_{1,AF}/U^2 = 2\dot{\chi}^{\Lambda,\ell}_{AF}$ as a function of the loop order plotted for different values of the integration parameter $t = \log_{10}\Lambda$ in the frequency flow with parameters $U = 3$, $1/T = 5$.

the result obtained through the frequency and interaction flow, respectively. In addition, the susceptibility was calculated in a post-processing procedure using Eq. (2.38). The full convergence in terms of loop orders is not yet reached at 8ℓ. Although this is far from the needed $N_\ell \approx 20$ (compare to Table 4.1), the final result is already a good estimate with only 4% deviation from the $U = 2$ result in Fig. 4.18. More importantly, the fact that

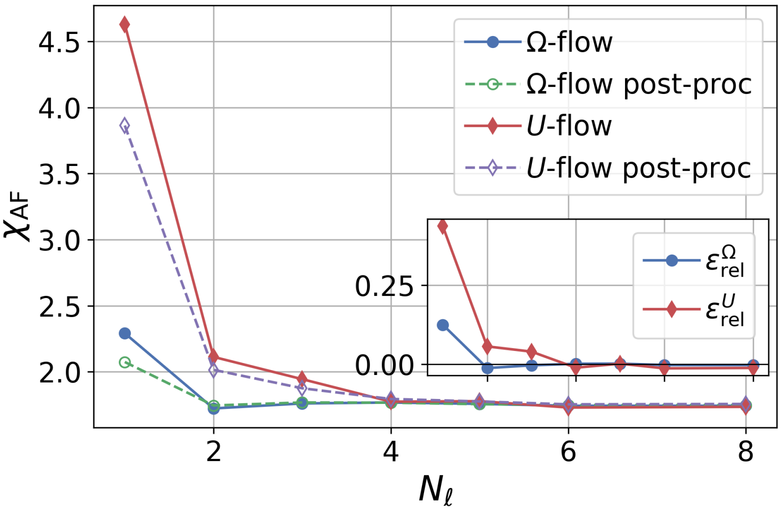

Figure 4.5: Comparison of the AF susceptibility calculated with the interaction flow and the Ω-flow as well as through their respective post-processing, as a function of the maximal number of loops, for $U = 2$ and $1/T = 5$. The inset shows the relative difference w.r.t. the 8ℓ value $(\chi_{AF}^{N_\ell} - \chi_{AF}^{\text{post-proc},N_\ell})/\chi_{AF}^{N_\ell=8}$.

all these calculation procedures converge to the same result indicates that the multiloop approach provides the full reconstruction of the derivative of Eq. (2.38). In other words, the vanishing relative difference (see also inset in Fig. 4.5) is the numerical verification of the derivation of the mutliloop equations from the parquet formalism in Ref. [67]. A more detailed analysis of this 8ℓ results revealed a persisting small discrepancy between the calculation schemes. Interestingly, this difference vanishes in absence of self-energy flow. Therefore, it can be attributed to the inconvenient application of the form-factors in the conventional self-energy flow. The newly introduced SDE-flow scheme in Section 3.2 solves this issue.

After the convergence in terms of loops, the effect of the self-energy iterations is studied. These are needed because the r.h.s. of both the vertex and the self-energy depend on each other through the single-scale propagator with Katanin substitution $S^K(\mathbf{k}, i\nu_m) = d_\Lambda G(\mathbf{k}, i\nu_m)$ and either the conventional mutliloop corrections of the self-energy Eqs. (2.32) and (2.34) or the first part of the SDE-flow equation Eq. (3.6). It was argued in Section 2.2.2 that in the conventional flow the multiloop corrections of the self-energy enter only at the third loop order. Therefore the correction due to the self-energy iterations is of the order $\mathcal{O}\big[U^3\big]$ for the self-energy and $\mathcal{O}\big[U^5\big]$ for the vertex. In the SDE-flow, the first term in Eq. (3.6) depending on $\dot{\mathbf{\Phi}}r$ prevents the insertion of the self-energy in the first Katanin-substitution. It enters the self-energy at order $\mathcal{O}\big[U^2\big]$ which leads to corrections in the vertex with $\mathcal{O}\big[U^4\big]$. In order to improve the SDE-flow scheme, the first self-energy iteration is performed with the Katanin-substitution from the conventional 1ℓ flow.

In Figs. 4.6 and 4.7, the effect of the self-energy iterations is studied both in the case with the conventional (fRG) and with the SDE flow (fRG*). For this aim, full multiloop calculations with first $N_{\Sigma-\mathrm{iter}} = 0$ (no Σ-iter.) and next $N_{\Sigma-\mathrm{iter}} = 5$ were calculated for both flow schemes. The resulting self-energy is shown in Fig. 4.6 for a momentum path along Γ-X-M-Γ restricting to the first Matsubara frequency and separating the real part in the left panel from the imaginary part in the right panel. In addition, Fig. 4.7 shows the imaginary part of the self-energy as a function of the frequency for the nodal (left

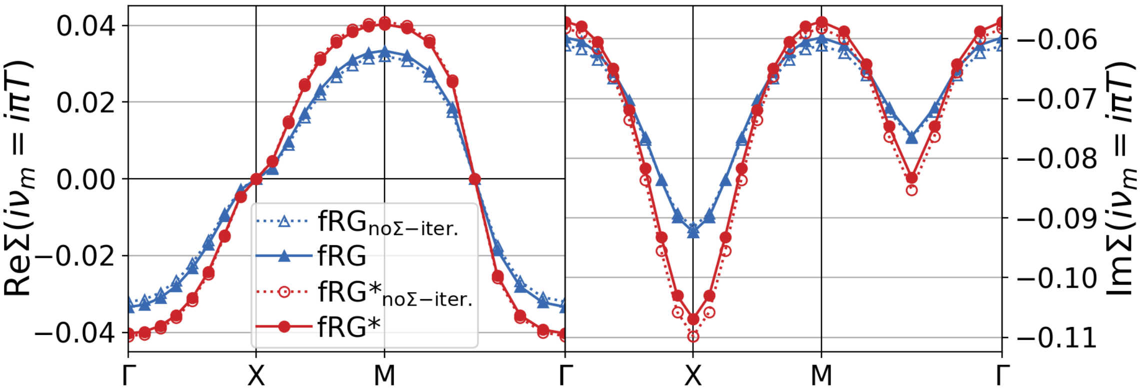

Figure 4.6: Real and imaginary part of the self-energy at the first Matsubara frequency with and without self-energy iterations as obtained by the conventional fRG (blue) and fRG* (red) for $U = 2$ and $1/T = 5$. The self-energy iteration (dotted line) has its strongest effect on the Fermi surface points of Im Σ in fRG*. It can be observed in the inset of Fig. 4.7 that the relative difference between the calculations with and without self-energy at the nodal and antinodal point lies below 1% in fRG and above in fRG*.

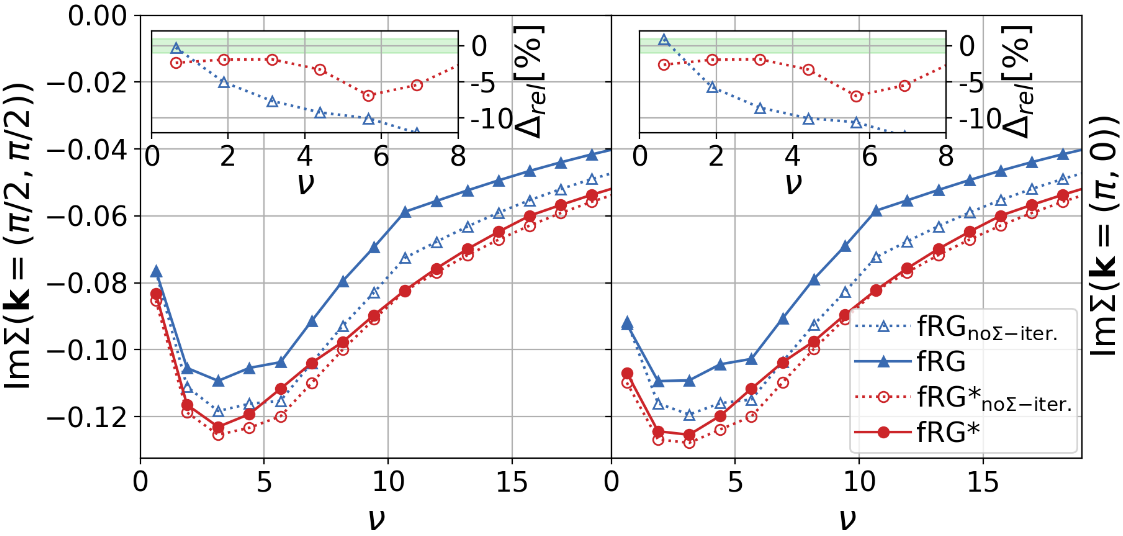

Figure 4.7: Imaginary part of the self-energy at the nodal and antinodal point with and without self-energy iterations as obtained by the conventional fRG (blue) and fRG* (red) for $U = 2$ and $1/T = 5$. The self-energy iteration (dotted line) has its strongest effect on the Fermi surface points of $\operatorname{Im}\Sigma$ in fRG*. The inset shows the relative difference between the calculations with and without, where the green shaded area marks 1%.

panel) and antinodal (right panel) point. At the first Matsubara frequency, there are no significant effects in fRG scheme and only slight differences can be observed in fRG*. With larger frequencies, the corrections due to the iterations remain constant at a few percent in fRG*, unlike in the fRG scheme, where the influence grows to $5 - 10\%$.

One can observe two slight kinks in the self-energy calculated using the fRG scheme in Fig. 4.7. They originate from the frequency treatment and more specifically from the crossing of the low frequency tensor range and the high frequency asymptotics of the two-particle vertex. As $N_{f+} = 4$, they occur between the 4th and 5th frequency and again between the 8th and 9th frequency. This effect is more pronounced in fRG than in fRG* since the channel reducible vertices entering the conventional flow in Eq. (2.11) have a richer frequency dependence than the bare interaction contracted channels in Eqs. (3.5d) to (3.5f) needed for the calculation of the SDE-inspired fRG* flow.

The effect of the self-energy iterations on the AF susceptibility is studied in Fig. 4.8 where the AF susceptibility is shown as a function of the transfer frequency. The results of the fRG (blue) and fRG* (red) flow with (solid line) and without (dotted line) are shown alongside with the post-processed fRG* one (dashed line) which will be discussed later. While the overall frequency structure is the same for both schemes and independent of the self-energy iterations, one can observe changes in the peak height displayed in the inset. Although in fRG, there are large effects at non-zero frequencies in the self-energy itself, they can not be observed in the χ_{AF}. On the other hand, the small correction in the self-energy in fRG* can be observed as a reduction of 2% of the AF-peak height.

As a last internal check, the post-processing procedure was applied. Applying exact relations on the final results of the flow, the convergence in all technical parameters can be tested without large effort. The agreement of a single observable calculated through the flow with the corresponding one obtained from post-processing, is not sufficient to claim convergence. But if all susceptibilities and the self-energy coincide, a strong hint towards

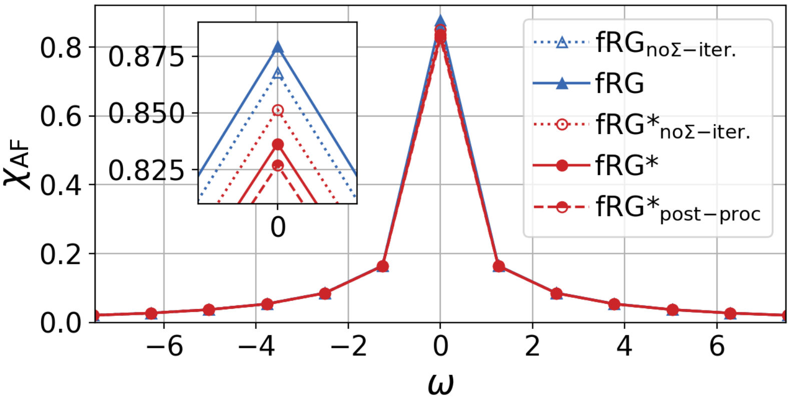

Figure 4.8: Antiferromagnetic susceptibility $\chi_{\mathrm{AF}}(i\omega)$ as obtained by conventional fRG (blue) and the fRG* flow (red), together with the respective post-processed results (dashed lines), for $U = 2$ and $1/T = 5$.

the satisfaction of the parquet equations is given. This test is performed in Figs. 4.5 and 4.8 for the susceptibilities. The scale in Fig. 4.5 is so big, that the small discrepancies due to loop convergence and conventional self-energy flow cannot be observed. It can be observed in Fig. 4.8 that in fRG* the post-processed result (red dashed line) lies only around 2% apart from the flowing AF-susceptibility (red solid line). Finally, the self-energy consistency is studied in Fig. 4.9 and in Fig. 4.10 showing the imaginary part as a function of frequency at the nodal (left panel) and antinodal point (right panel). The post-processed self-energy lies on the flowing one only in the fRG*-scheme. Even though the flowing self-energy calculated through the conventional flow equations differ from these results for the reason already explained in Section 3.1, the differences decrease significantly in the post-processing results due to a single application of the SDE.

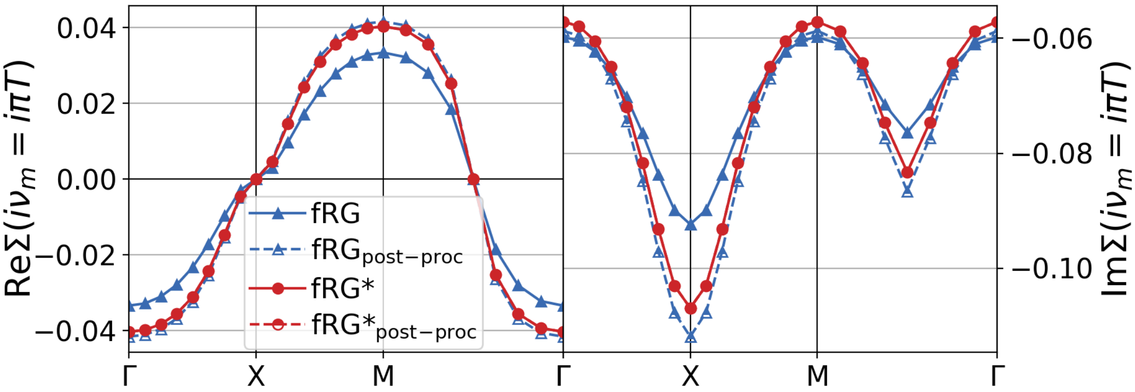

Figure 4.9: Real and imaginary part of the self-energy at the first Matsubara frequency as obtained by fRG (blue) and fRG* (red) compared to the respective post-processed results for $U = 2$ and $1/T = 5$. Within fRG*, the post-processed results (dashed red) lie exactly on top of the fRG* flow ones (red solid).

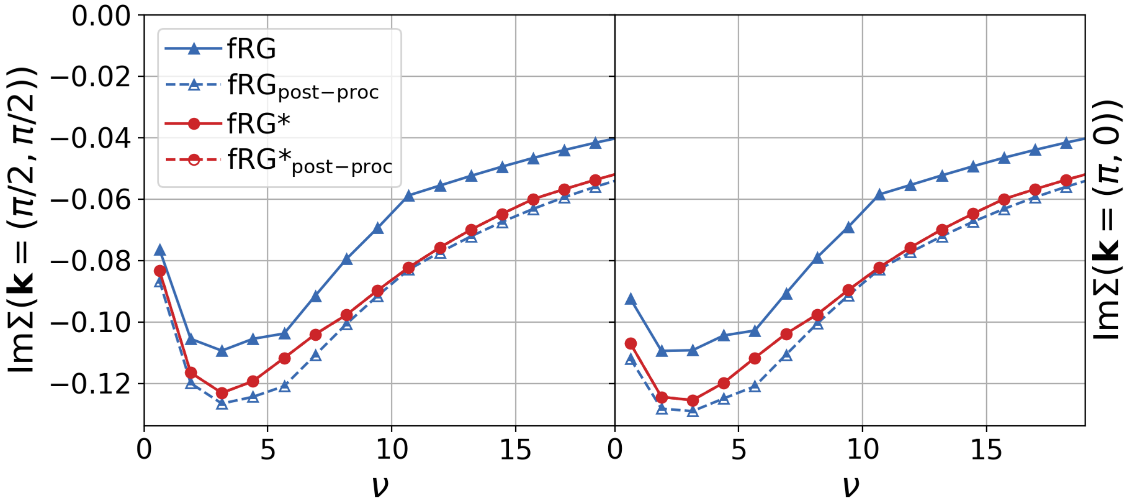

Figure 4.10: Imaginary part of the self-energy as a function at the nodal and antinodal point as obtained by fRG (blue) and fRG* (red) compared to the respective post-processed results for $U = 2$ and $1/T = 5$. Within fRG*, the post-processed (dashed red) lie exactly on top of the fRG* flow results (red solid).

4.3 External benchmark

After the internal convergence and consistency studies, the comparison of the fRG* results to other methods can be performed. For the latter, the PA and the dQMC are considered which are introduced in Section 4.3.1. In Section 4.3.2, numerical results as obtained by these methods are presented. As convergence in fRG* is easier to reach for small interaction strengths, first the comparison with PA at $1/T = 5$ and $U = 0.5$ and then at $1/T = 5$ and $U = 2$ is shown for the half-filled Hubbard model at $t' = 0$, including also dQMC results. Next, the interaction dependence is studied and finally the hole doped case with finite t' is considered. For all fRG* calculations in this section, the Ω-flow was adopted.

4.3.1 Benchmark methods

In this benchmark, two comparing methods were chosen. On the one hand, fRG* is formally equivalent to the PA if all approximation issues are overcome. In order to prove this numerically, all results in this section are compared to PA. On the other hand, the exact dQMC is used for comparison in order to test the validity of the parquet approximation. The difference between dQMC and PA or fRG*, is solely due to the completely two-particle irreducible diagrams like e.g. the right diagram of Fig. 2.1.

Parquet

The PA results are provided by Christian J. Eckhardt and Anna Kauch with the truncated-unity implementation of the parquet equations [18]. This method is based on the parquet equation already introduced in Eq. (2.4) with the parquet approximation for the two-particle irreducible part $V_{\mathrm{2PIR}}(k_1, k_2, k_3) \approx U$, the SDE in 3.2, and the Bethe-Salpeter equations. These equations are solved by iteration until self-consistency is reached. Due to the equivalence of the PA and the multiloop fRG formally shown [68] this method is closely related to fRG*. Many numerical challenges like the parametrization of the vertex are very similar. A substantial difference is the absence of a flow parameters of cutoff dependence in PA. Therefore, no differential equations are solved and the convergence to a fixed point is achieved iteratively. The initial guess for the vertices is given here by the lowest order diagrams.

The computational details can be found in [18] and only the most important aspects are presented here. As in TUfRG, the momentum dependence of the vertices is parametrized using the form-factor expansion [17]. The frequency dependence is evaluated on a the finite frequency box. Values outside of the box were recovered by the asympotics as introduced in Ref. [75] and also used in Ref. [74]. This leads to a different implementation of the frequency asymptotics w.r.t. the one used in the fRG calculations.

Also a detailed analysis of the convergence in the number of form factors was performed in Ref. [18]. From this follows that the single form factor approximation is justified at half-filling. Further, all results are converged in terms of the other vertex parameters: for the bosonic lattice momenta $N_q = 32 \times 32$ and for the frequencies $N_{f+} = 32$ were used.

Determinant quantum Monte Carlo

The dQMC calculations were performed by Yuan-Yao He. dQMC is an exact method from the quantum Monte Carlo family and as thus based on importance sampling. Applicable to finite-temperature Fermi systems, the method integrates out the fermionic degrees of freedom in order to obtain non-interacting fermions coupled to an auxiliary field [11, 99].

Yuan-Yao He describes the specific implementation in Ref. [38] referring also to Refs. [34, 35] for a detailed description of its most recent improvements. Here, just the technical parameters are provided for completeness: The width for the discretization of the inverse temperature is $\Delta\tau = 0.2$ in inverse units of t. Concerning the system size, the results are converged with $N = 28 \times 28$ for $t' = 0$ and half-filling and $N = 24 \times 24$ for $t' = -0.2$ and finite doping. Typically, 10^5 measurements samples are collected after the Markov Chain equilibrium process. These parameters yield error bars smaller than the dQMC symbol which are therefore not reported in the plots.

4.3.2 Results

In the following, fRG*, PA and dQMC are compared at $T = 1/5$ and different interaction strengths U and finally also doping. If convergence can be achieved, fRG* and PA yield in principle the same result. However, convergence in technical parameters related to the vertex or the mutliloop implementation becomes harder at larger interaction strengths, lower temperatures and away from half-filling when the channel competition sets in. While the fRG* and PA are bounded to the parquet approximation, dQMC is correct. Therefore a difference growing with U^4 related to the first two-particle irreducible diagram is expected. The following results are ordered according to their complexity. First self-energy and susceptibilities for $U = 0.5$, then for the computationally more challenging $U = 2$ are shown. Then, the interaction dependence for selected quantities is studied and finally, results for

Self-energy and magnetic susceptibility at $U = 0.5$

As a proof of principle, the equivalence between fRG* and PA is studied here for $1/T = 5$ and $U = 0.5$. At this weak interaction the AF peak is not so prominent and the system

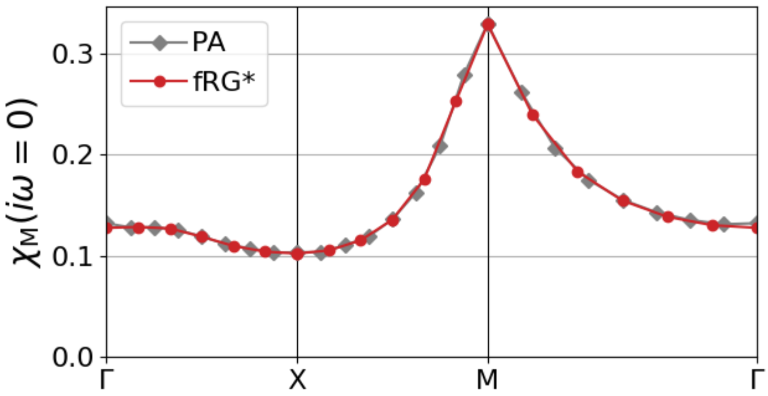

Figure 4.11: Magnetic susceptibility at zero Matsubara frequency along the Γ-X-M-Γ path as obtained by fRG* (red) and the PA (grey), for $U = 0.5$ and $1/T = 5$.

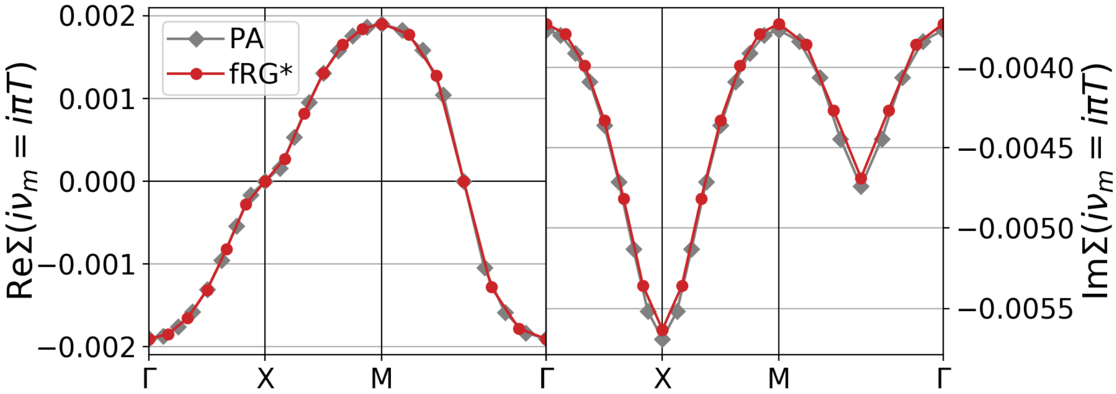

Figure 4.12: Real and imaginary part of the self-energy as a function of the momentum as obtained by fRG* (red) and the PA (grey), for $U = 0.5$ and $1/T = 5$.

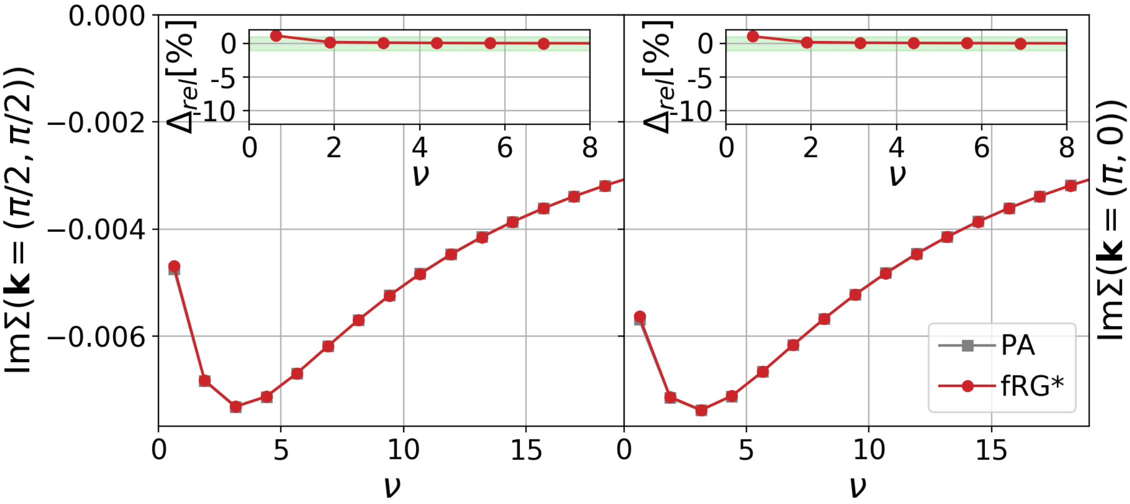

Figure 4.13: Imaginary part of the self-energy at the nodal and antinodal point as obtained by fRG* (red) and the PA (grey), for $U = 0.5$ and $1/T = 5$. The relative difference is always below 1%.

is only weakly correlated. Therefore the calculation requires only few momentum patches and a large frequency box with $N_{f+} = 8$ positive fermionic frequencies can be used. In Fig. 4.11, the magnetic susceptibility at zero transfer frequency is shown for the momentum path Γ-X-M-Γ. The fRG* and PA agree very nicely with the largest relative difference of 4% at the non-relevant Γ-point, and only $0,2\%$ at the M-point, describing the AF tendency. In Fig. 4.12, the real (left panel) and imaginary part (right panel) at the first Matsubara frequency are shown as a function of momentum. The real part is perfectly converged and the imaginary part has deviations at the nodal and antinodal point of only 1%. Fig. 4.13 shows the imaginary part of the self-energy as a function of frequency for the nodal and antinodal point. For the imaginary part at the nodal and antinodal point, the relative difference is below 1% for all frequencies. Besides the improved convergence, also the box effects are suppressed w.r.t. smaller N_{f+}.

Self-energy and susceptibilities at $U = 2$

With increasing interaction strength, it is more challenging to reach for convergence in all methods. Nevertheless, results for $1/T = 5$ and $U = 2$ are shown for all methods in Figs. 4.14 to 4.16. The technical parameters used are reported in Table 4.1 for fRG* and in Section 4.3.1 for PA as well as dQMC.

First, the momentum dependence of the magnetic susceptibility at zero frequency $\chi_{\mathrm{M}}(\mathbf{q}, i\omega_l = 0)$ is presented in Fig. 4.14. The results of fRG*, the PA, and dQMC exhibit quantitative agreement. The largest deviation is found at $M = (\pi, \pi)$ and results in 2% difference between fRG* and PA and 3% between fRG* and dQMC. The susceptibility at this momentum point corresponds to AF fluctuations. In the inset, the latter is shown as a function of frequencies as obtained by fRG* (red) and PA (grey).

From the momentum dependence of the magnetic susceptibility, the AF correlation length ξ can be extracted. For this scope, the ansatz

$$\chi(\mathbf{q}, i\omega_l = 0) \sim \frac{1}{4\sin^2(\frac{q_x - \pi}{2}) + 4\sin^2(\frac{q_y - \pi}{2}) + \xi^{-2}} \tag{4.6}$$

is fitted to all points of $\chi_{\mathrm{M}}(\mathbf{q}, i\omega_l = 0)$ within a distance of 0.3π from M. Eq. (4.6) reduces to the Ornstein–Zernike formula for small momentum differences $q_x - \pi$ and $q_y - \pi$ (see

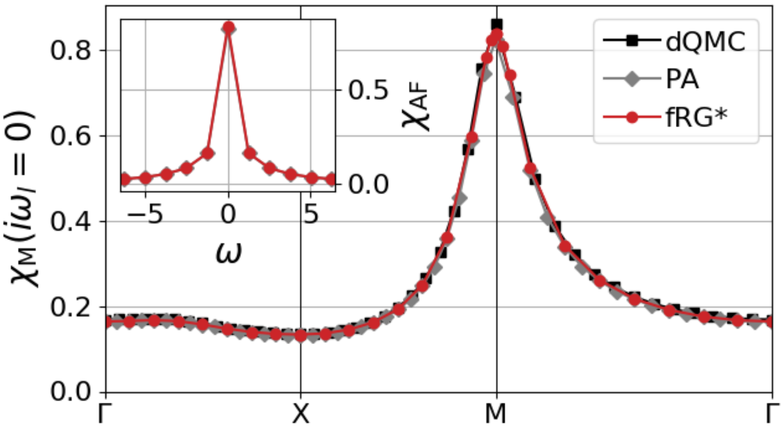

Figure 4.14: Magnetic susceptibility $\chi_{\mathrm{M}}(\mathbf{q}, i\omega_l = 0)$ as obtained by fRG* (red), the PA (grey), and dQMC (black), for $U = 2$ and $1/T = 5$. The inset shows the AF susceptibility as a function of frequency as obtained by fRG* (red) and PA (grey).

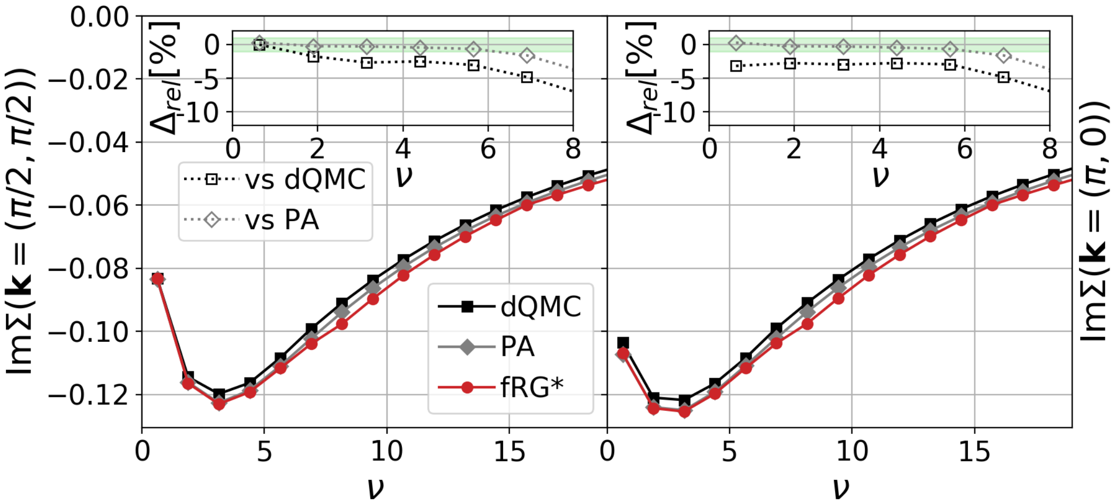

Figure 4.15: Imaginary part of the self-energy at the nodal and antinodal point as obtained by fRG* (red), the PA (grey), and dQMC (black), for $U = 2$ and $1/T = 5$. Inset: relative difference, with the green region indicating a deviation of less than 1%.

Ref. [93, 104]). For $U = 2$ and $1/T = 5$, the number of momenta taken into account for the fit is 45 in fRG*, 69 in PA, and 57 in dQMC and the standard deviation error is 0.019 in fRG*, 0.022 in PA, and 0.022 in dQMC. The resulting $\xi = 1.38$ in fRG*, $\xi = 1.32$ in PA, and $\xi = 1.36$ in dQMC, show deviations under 5%. In particular the agreement between fRG* and dQMC is astonishing, considering that the AF peak height is less accurate.

Next, Fig. 4.15 is discussed, comparing the behavior of the self-energy at the nodal and antinodal point as a function of frequency using the different methods. The inset shows the relative difference of fRG* w.r.t. dQMC (black) and PA (grey). The latter is below 1% for all frequencies not affected by the box effects. The difference between fRG* (or PA) w.r.t. dQMC is below 1% for the first frequency at the nodal point and within few percents otherwise. The self-energy shows typical Fermi-liquid behavior, $\text{Im}\Sigma(i\nu \to 0) \to 0$, both at the nodal and the antinodal point. The antinodal point is affected more strongly by correlations, manifesting itself through an increased absolute value for the lowest Matsubara frequencies. While this momentum anisotropy is present, no clear signature of a pseudogap is observed.

The deviations between fRG* and the PA are slightly larger at Matsubara frequencies larger than N_{f+}. As the fRG* self-energy agrees perfectly with its post-processing result (see also Fig. 4.10), these differences are not related to convergence issues but due to the specific implementation of the high-frequency asymptotics of the the two-particle vertex [129]. In fRG* the asymptotic functions are calculated and stored explicitly [110]. This allows to retain smaller frequency tensors w.r.t. the PA for converged low frequency results but on the other hand it evokes box effects in the intermediate frequency range. In the PA implementation a large tensor over many fermionic and bosonic frequencies is used and the values outside are constructed from the ones at the edges [75, 18].

On a quantitative level, in the full Green's function $G(\mathbf{k}, i\nu_m)$ the differences between the frequency dependence of fRG* and the PA self-energy are almost negligible w.r.t. the large $i\nu_m$ contribution in the denominator, see Eq. (4.4).

In Fig. 4.16, the comparison of the self-energy is performed as a function of momentum. In the real part of the self-energy (left panel), fRG* compares nicely to PA while there is

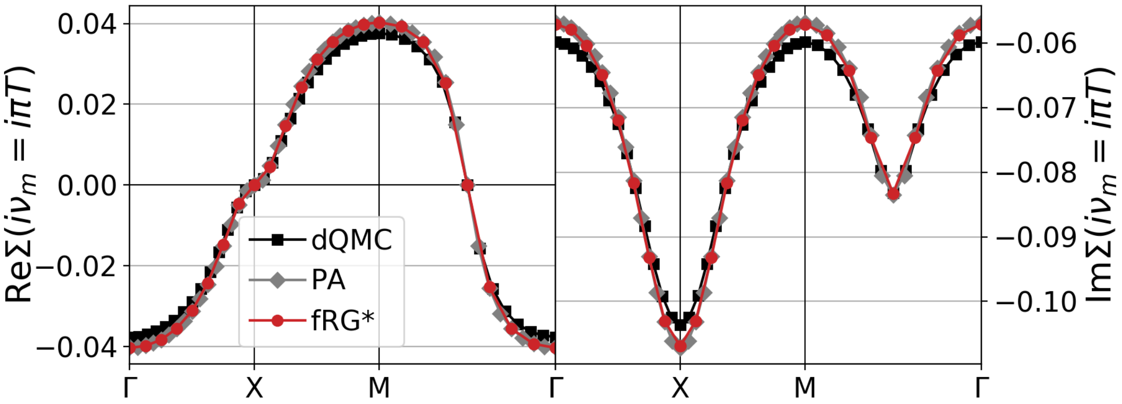

Figure 4.16: Real and imaginary part of the self-energy at the first Matsubara frequency as obtained by fRG* (red), the PA (grey), and dQMC (black), for $U = 2$ and $1/T = 5$.

a difference of 7% at the Γ- and M-point w.r.t. dQMC. The differences in the imaginary part of the self-energy between fRG* (red) and the PA (grey) are largest at momenta far away from the Fermi surface (see right panel). Since it is the Green's function and not the self-energy that directly enters the calculation of observables, these momenta have little influence. Moreover, the relative difference between the methods for the Green's function at the Γ and M points is less than 3‰. The physically more important momenta X and M/2 show only 1% difference between fRG* and PA which can also be observed in the inset of Fig. 4.15.

Interaction dependence

In the following, selected quantities for a range of interaction values between $U = 0$ and $U = 3$ and $1/T = 5$ are shown. From this data, one can obtain information on the validity of the parquet approximation with increasing interaction. Also limitations due to numerical complexity are discussed. The latter can be overcome by further numerical optimizations. The technical parameters used in this study are summarized in Table 4.1.

First, the results for the leading AF susceptibility, χ_{AF} are presented as a function

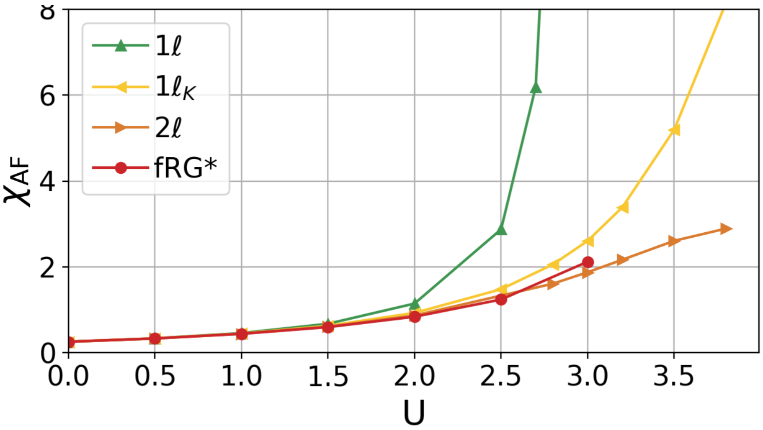

Figure 4.17: Antiferromagnetic susceptibility χ_{AF} as a function of the bare interaction U, for $1/T = 5$.

U	$N_{\mathbf{q}}$	$N_{\mathbf{k}}$	N_{f+}	N_{ℓ}	$N_{\Sigma\text{-iter}}$
0.0	$12\times 12+24$	60×60	4	1	1
0.5	$12\times 12+24$	60×60	4	16	5
1.0	$16\times 16+24$	80×80	4	16	5
1.5	$16\times 16+24$	80×80	4	16	5
2.0	$16\times 16+24$	80×80	6	24	5
2.5	$16\times 16+24$	80×80	6	28	5
3.0	$16\times 16+24$	80×80	6	28	5

Table 4.1: fRG* parameters used in Section 4.3.2. The additional 24 bosonic patching points in $N_{\mathbf{q}}$ are distributed around $\mathbf{k} = (\pi, \pi)$. $N_{\mathbf{k}}$ is the number of points in the momentum integration of the fermionic bubble. The frequency ranges of the vertex and vertex asymptotics are proportional to the number of positive fermionic frequencies N_{f+} of the low-frequency object with three dependencies. Due to computational limits, the calculations for $U > 2$ are not converged w.r.t. the number of loops N_{ℓ} and self-energy iterations $N_{\Sigma\text{-iter}}$.

of the bare interaction strength U using different loop truncations of fRG*. In Fig. 4.17, the 24ℓ-fRG* scheme (red) is compared to the 1ℓ (green), 1ℓ extended by Katanin substitution (yellow) and 2ℓ flow scheme (orange) with conventional self-energy flow. The 1ℓ scheme strongly overestimates the peak at momentum transfer $\mathbf{q} = (\pi, \pi)$ leading to an AF ordering at finite interaction strength in violation of the Mermin–Wagner theorem [81]. With increasing loop order, the AF peak is reduced. At an inverse temperature of $1/T = 5$, the differences in the susceptibility between the 2ℓ result and fRG* become very small. In the loop truncations between the 2ℓ and 24ℓ, multiloop oscillations around the 24ℓ result take place which are not shown here but can be observed in Fig. 4.5. We note that for $U = 3$ fRG* is not fully converged w.r.t. loop order and for this reason no results for larger values of U are displayed. The convergence threshold we use is of 1% for χ_{AF}, $\operatorname{Im}\Sigma(\mathbf{k} = (\pi, 0), i\nu_{0/1})$ and $\operatorname{Im}\Sigma(\mathbf{k} = (\pi/2, \pi/2), i\nu_{0/1})$.

Next, χ_{AF} as obtained by fRG* (red), PA (grey), and dQMC data (black) is shown in Fig. 4.18 as a function of U, together with the relative difference of fRG* w.r.t. PA and dQMC shown in the inset. Up to $U = 1.5$, fRG* and PA coincide with a relative difference of $\leq 1\%$ (indicated by the green shaded area) and at $U = 2$ the difference is still less than 2%. For larger values of U, the convergence of fRG* in frequencies and also in loop numbers and self-energy iterations becomes numerically challenging and is not reached yet leading to deviations from the PA solution. This can be seen also in the comparison with the post-processed result (dashed line) shown in the upper left panel of Fig. 4.21, which differs from the flowing one (solid line). Concerning the comparison between the PA and the numerically exact dQMC data, the deviation grows monotonously with U due to the increasingly importance of the fully two-particle irreducible diagrams. These diagrams contribute to fourth order in U. A fitting of the relative difference yields the dependence $\Delta_{\mathrm{rel}} \simeq 0.003\, U^4$. A second source of the differences between the PA solution and dQMC is given by the form-factor expansion of the two-particle vertex which accounts only for the local s-wave part. Due to perfect nesting, the physics at half-filling is dominated by magnetic fluctuations peaked at $\mathbf{q} = (\pi, \pi)$ and at small coupling, there is only a small quantitative correction due to the form-factor truncation [18].

Also the correlation length ξ, reported in Fig. 4.19, shows a very good agreement for small U. For the fit of ξ Eq. (4.6) was used. The number of momenta taken into account

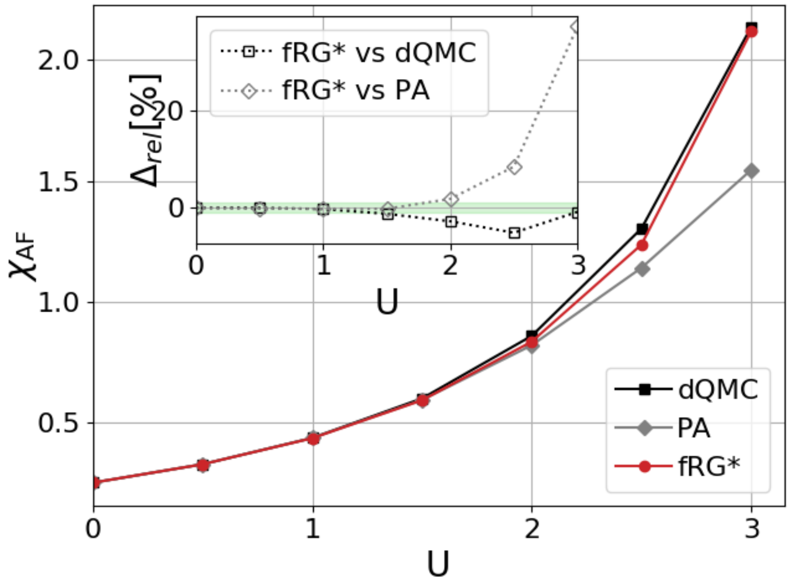

Figure 4.18: Antiferromagnetic susceptibility χ_{AF} as a function of U, as obtained by fRG* (red), the PA (grey), and dQMC (black), for $1/T = 5$. The inset shows the relative difference of fRG* w.r.t. the benchmark methods.

are between 33 and 45 in fRG*, 69 and 161 in PA, and 57 in dQMC. The maximal standard deviation error is 0.027 in fRG*, 0.025 in PA, and 0.028 in dQMC.

The subleading susceptibilities κ, χ_{CDW}, $\chi_{\text{SC},s}$ and $\chi_{\text{SC},d}$ are shown as a function of U in Fig. 4.20. In fRG*, the s-wave susceptibilities κ, χ_{CDW} and $\chi_{\text{SC},s}$ are obtained through the flow while the d-wave susceptibility $\chi_{\text{SC},d}$ has been calculated using the post-processing procedure. It was explicitly checked that $\chi_{\text{CDW}} = \chi_{\text{SC},s}$. This property follows from the simultaneous $SU(2)$ spin and charge (particle-hole) symmetry present in the 2D Hubbard model with $t' = 0$ at half-filling and its analytical proof can be found in Appendix D of Ref. [38]. The quantitative agreement between fRG*, PA and dQMC results for the subleading susceptibilities is again very good for small U. The relative difference of fRG* w.r.t. the PA at $U = 3$ is 14% for κ, 12% for χ_{CDW}, and 2% for $\chi_{\text{SC},d}$, and w.r.t. dQMC

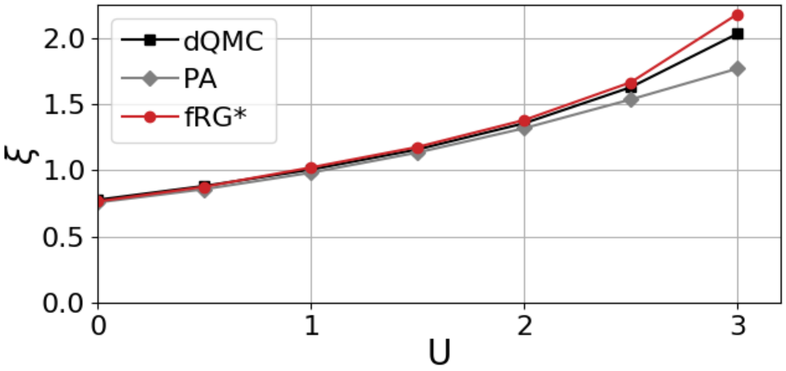

Figure 4.19: Correlation length ξ extracted from $\chi_{\text{M}}(\mathbf{q}, i\omega_l = 0)$ as a function of U as obtained by fRG* (red), the PA (grey), and dQMC (black), for $1/T = 5$. See text for the details of the fitting procedure.

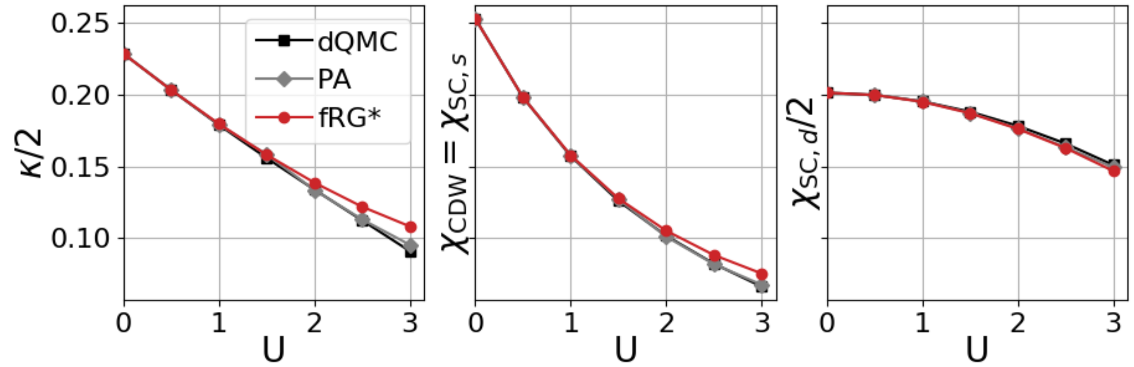

Figure 4.20: Compressibility κ, charge density wave $\chi_{\text{CDW}} = \chi_{\text{SC},s}$, and superconducting susceptibility $\chi_{\text{SC},d}(i\omega_l = 0)$ (determined by post-processing) as a function of U, as obtained by fRG* (red), the PA (grey), and dQMC (black), for $1/T = 5$.

18% for κ, 14% for χ_{CDW}, and 3% for $\chi_{\text{SC},d}$. The compressibility κ is also consistent with Ref. [60]. The good agreement between fRG* and PA, taking into account only the s-wave form factor, and the exact dQMC indicates that the d-wave vertices are very small. This justifies justifies in retrospect the truncation to a single s-wave form factor.

In contrast to χ_{AF}, all subleading susceptibilities in Fig. 4.20 decrease with U as they are screened by the growing AF fluctuations. For a more detailed analysis, the flowing susceptibilities are shown in Fig. 4.21 alongside with post-processing results and

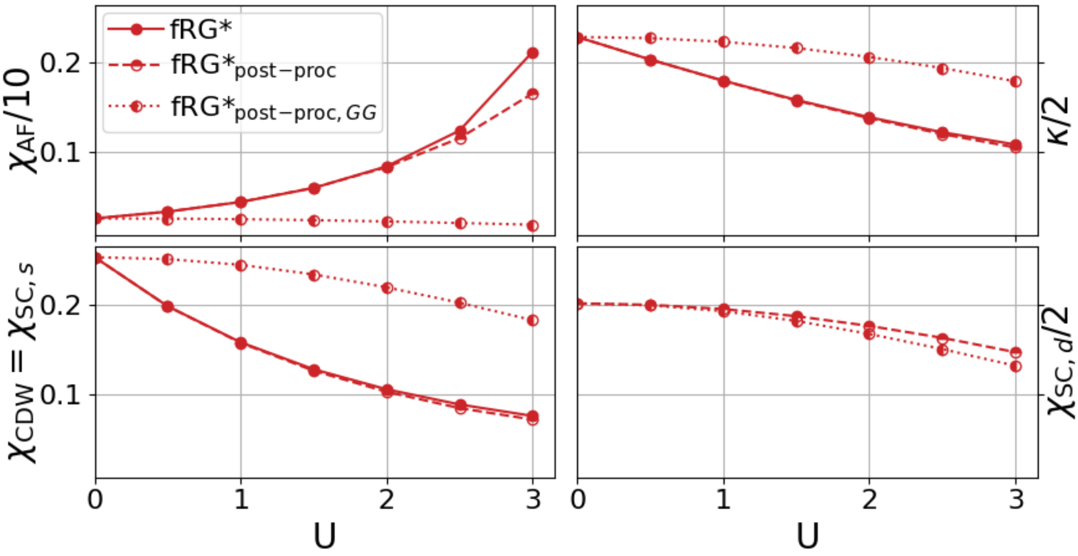

Figure 4.21: Antiferromagnetic susceptibility χ_{AF}, compressibility κ, charge density wave $\chi_{\text{CDW}} = \chi_{\text{SC},s}$ (for $t' = 0$ and half-filling) and d-wave superconducting susceptibility χ_{SC} as a function of U, as obtained by fRG* flow (solid lines) and the post-processed result (dashed lines), with and without vertex corrections, for $1/T = 5$.

the ‘uncorrelated’ susceptibilities

$$\begin{aligned}\chi_{\mathrm{AF},GG} &= \chi_{\mathrm{CDW},GG} \\ &= \frac{1}{2}\sum_{i\nu}\Pi_{ph,0\,0}(\mathbf{q}=(\pi,\pi), i\omega_l=0, i\nu_m) \qquad (4.7\mathrm{a})\end{aligned}$$

$$\kappa_{GG} = 2\sum_{i\nu}\Pi_{ph,0\,0}(\mathbf{q}=(0,0), i\omega_l=0, i\nu_m) \qquad (4.7\mathrm{b})$$

$$\chi_{\mathrm{SC},d,GG} = \frac{1}{2}\sum_{i\nu}\Pi_{pp,1\,1}(\mathbf{q}=(0,0), i\omega_l=0, i\nu_m)\ , \qquad (4.7\mathrm{c})$$

where the form-factor index 0 stands for s-wave and 1 for d-wave. The latter are calculated using the dressed Green’s functions and are therefore affected by the self-energy but not by two-particle vertex corrections.

Comparing the post-processed susceptibilities to the ones obtained from the flow, provides an indication of the fRG* convergence w.r.t. momenta, frequencies, and loop number. The difference in χ_{AF} for $U > 2$ shows that convergence in frequencies and loop numbers is difficult to achieve for the fRG* calculations at these parameters. On the other hand, the agreement is within numerical accuracy for the subleading susceptibilities. The effect of the vertex contribution can be studied comparing the post-processed susceptibility with the ‘connected’ post-processed susceptibilities. For χ_{AF}, the connected part decreases with U as self-energy effects lead to enhanced screening. However, the vertex contribution overcompensates this effect, leading to overall increasing AF fluctuations. In the subleading susceptibilities $\chi_{\mathrm{SC},s}$ and κ the decreasing tendency in the connected part is further

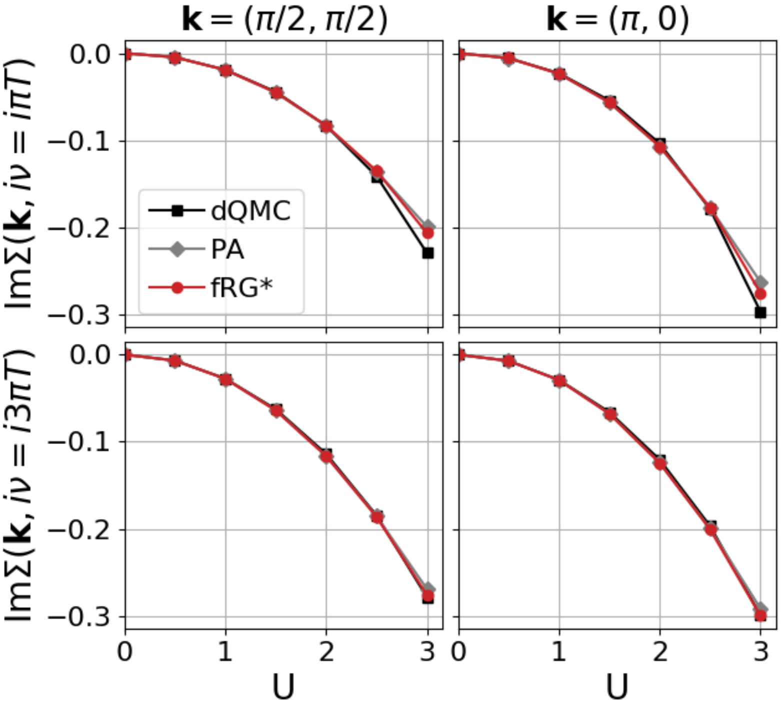

Figure 4.22: Imaginary part of the self-energy at the nodal and antinodal point as a function of U, as obtained by fRG* (red), the PA (grey), and dQMC (black), for $1/T = 5$.

enhanced by the vertex contributions. Finally, in $\chi_{\mathrm{SC},d}$ the connected part is enhanced by vertex corrections but unlike in χ_{AF} these are not strong enough to induce an overall increasing susceptibility.

Finally the comparison of the self-energy as obtained from the different methods is performed in Fig. 4.22. For this purpose, the imaginary part at the nodal $\mathbf{k} = (\pi/2, \pi/2)$ (left panels) and antinodal $\mathbf{k} = (\pi, 0)$ (right panels) point is shown as a function of U, for $1/T = 5$. Only the first (upper panel) and second (lower panel) frequencies are studied. For the comparison at other frequencies, it is referred to Fig. 4.15 for $U = 2$ and Fig. 4.13 for $U = 0.5$. The agreement between fRG* and the PA is almost perfect for small values of U, with slightly increasing deviations for larger U. In particular, at $U = 2$, fRG* and PA agree within 0, 2% for all shown quantities. For $U = 3$, the relative difference is only 3% for the second Matsubara frequency (lower panels) while the deviations at the first Matsubara frequency (upper panels) are more pronounced, reaching 5%. However,the dQMC results at $U = 3$ for the first Matsubara frequency differ considerably from those of fRG* and PA. Moreover, in dQMC the self-energy at $\mathbf{k} = (\pi, 0)$ yield quasi-identical results for the the first and second Matsubara frequency. The crossing of these values indicates an important physical process: the onset of the pseudogap opening [101, 103, 107] which is discussed in more detail in Chapter 5. The neglected fully two-particle irreducible diagrams prevents the opening of the pseudogap in PA and fRG* at $U \leq 3$ where the difference between the first and second Matsubara frequency is still 11% for PA and 9% for fRG*.

Results away from half-filling

The following comparison between fRG*, PA, and dQMC is performed for the next-nearest neighbor hopping $t' = -0.2$ and different chemical potentials $\mu = -0.35$, -0.7, -1.4, -2, again for the inverse temperature $1/T = 5$ and interaction $U = 2$. In presence of a finite doping and an additional next-nearest neighbor hopping t', the physical behavior is much richer and not exclusively driven by AF fluctuations any more. The channel coupling is expected to increase and in particular superconducting d-wave components become relevant. Therefore the form-factor truncation is extended to both s- and d-wave. The other technical parameters used in this study are reported in Table 4.2.

δ	$N_{\mathbf{q}}$	$N_{\mathbf{k}}$	N_{f+}	N_ℓ	$N_{\Sigma\text{-iter}}$
-0.012	18×18	90×90	2	22	5
0.087	18×18	90×90	2	26	5
0.301	18×18	90×90	2	26	5
0.484	18×18	90×90	2	26	5

Table 4.2: fRG* parameters used in Section 4.3.2. The calculations are converged w.r.t. $N_{\mathbf{q}}$, $N_{\mathbf{k}}$, N_ℓ and $N_{\Sigma\text{-iter}}$. As the calculations with an additional d-wave form factor are numerically challenging, the frequency range was fixed to $N_{f+} = 2$.

Due to the self-energy flow in fRG*, the Fermi-surface shifts. Therefore the filling changes in the flow and the final filling cannot be predicted a priori unless some additional mechanism is included [82] e.g. through a counterterm [85] or an adaptive scheme [48]. Here, the fixed chemical potential approach is chosen which is both consistent and transparent and has no need for further numerical evaluations. The Fermi-surface shift is very small close to half-filling and increases with doping $\delta = 1 - \langle \hat{n} \rangle$. In the representation of the result in Figs. 4.23 and 4.24 the final doping is reported.

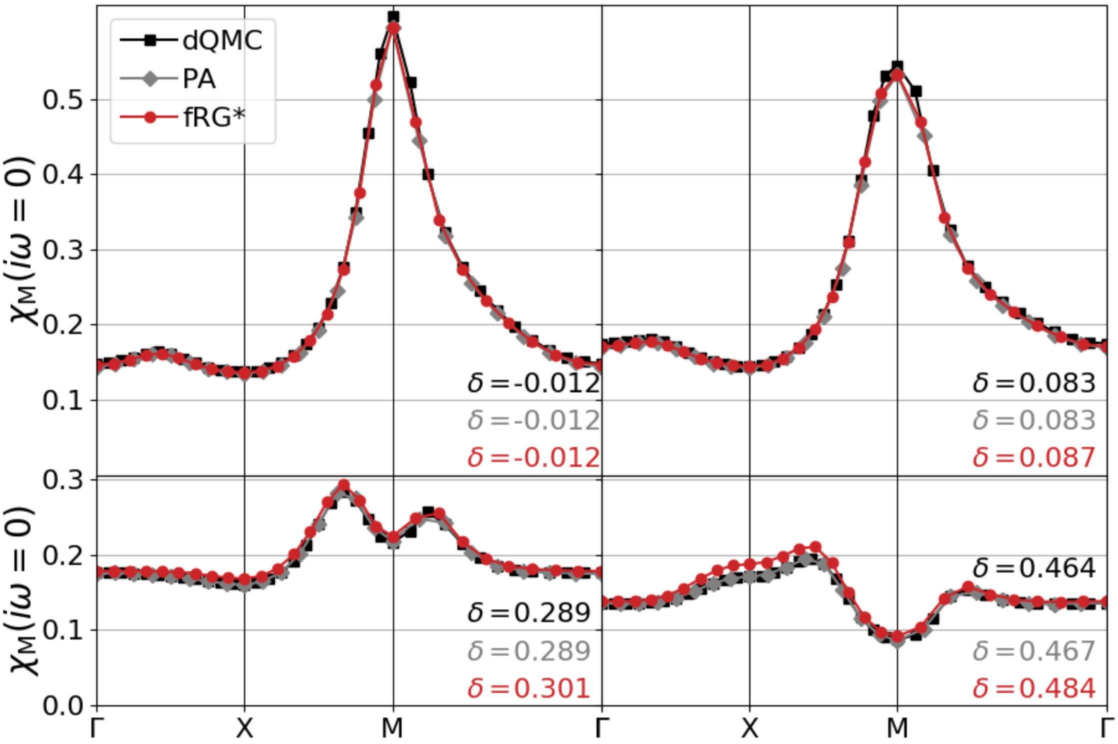

Figure 4.23: Magnetic susceptibility $\chi_{\mathrm{M}}(i\omega_l = 0)$ as obtained by fRG* (red), the PA (grey), and dQMC (black), for $U = 2$, $1/T = 5$ and different values of the doping δ.

In Fig. 4.23, it can be observed how the structure of the magnetic susceptibility $\chi_{\mathrm{M}}(\mathbf{q}, i\omega_l = 0)$ in momentum space is changed with the doping. Other susceptibilities like the compressibility κ, the charge density wave χ_{CDW}, and superconducting χ_{SC} (s- and d-wave) susceptibility are shown in Fig. 4.24 as a function of doping. Note that the system is no longer particle-hole symmetric and therefore χ_{CDW} and $\chi_{\mathrm{SC},s}$ are not equivalent any more.

The magnetic susceptibility dominates for all dopings. It is maximal at the commensurate antiferromagnetic wave vector (π, π) for $\mu = -0.35$ and $\mu = -0.7$ (upper two panels), and at incommensurate wave vectors for larger values of the doping (lower two panels), consistent with previous fRG findings [121, 120].

There is no large superconducting susceptibility or even pairing instability found with any of these parameters as the temperature $1/T = 5$ is still very high. Also charge susceptibilities are still reduced w.r.t. to $\chi_{\mathrm{M}}(\mathbf{q}, i\omega_l = 0)$. However, the (in-)commensurate peak in $\chi_{\mathrm{M}}(\mathbf{q}, i\omega_l = 0)$ decreases for increasing δ and the subleading susceptibilities gain importance in relation to the (in-)commensurate AF fluctuations. For the maximal doping considered in Fig. 4.23, the maximum of $\chi_{\mathrm{M}}(\mathbf{q}, i\omega_l = 0)$ is only half as large as $\chi_{\mathrm{SC},d}$.

From Refs. [30, 53, 57, 120] it can be understood, that while the AF susceptibility gradually evolves from the beginning of the flow, the superconducting d-wave susceptibility emerges only in proximity of the critical scale. It is followed that the AF fluctuations are responsible for the d-wave pairing. The parameter regime presented here is far away from any instability. Hence, for a finite doping a large and diverging d-wave pairing susceptibility is expected only at lower temperatures. These temperatures cannot be accessed in the moment due to the high computational cost of low-T calculations. The

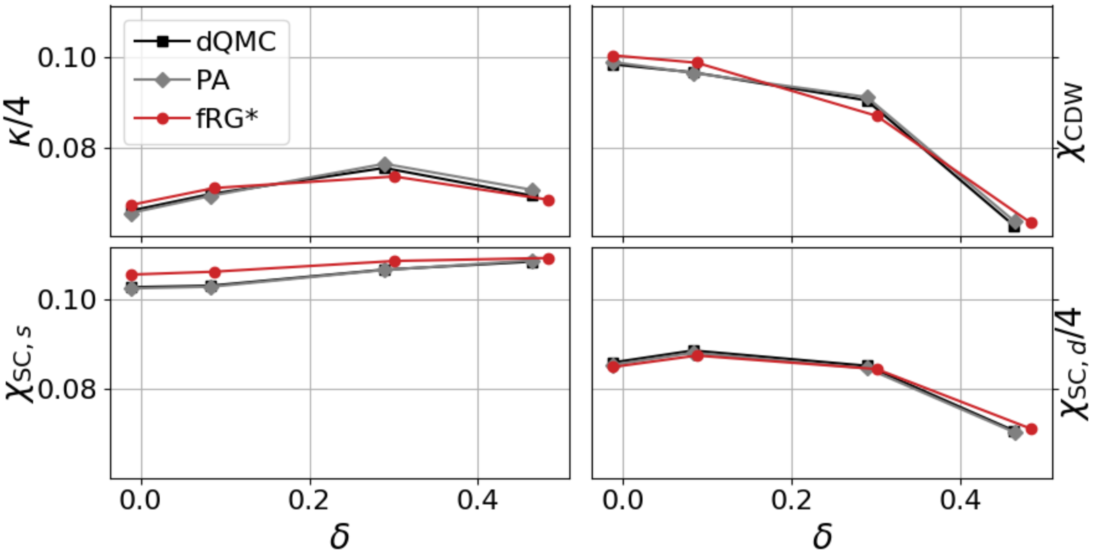

Figure 4.24: Compressibility κ, charge density wave χ_{CDW}, and superconducting susceptibility χ_{SC} in s- and d-wave (both from the flow) as obtained by fRG* (red), the PA (grey), and dQMC (black), for $U = 2$, $1/T = 5$ and different values of the doping δ.

key challenge is to achieve an accurate parametrization of the frequency dependence of the two-particle vertex.

The agreement of fRG* with the PA and the numerically exact dQMC data is very good also away from half-filling. No relative differences are shown because a comparison at different fillings is not meaningful. Moreover, due to the high numerical cost, the present fRG* calculation including s- and d-wave form factors is not fully converged in frequencies. This hardly affects the susceptibilities, while the quantitative accuracy of the self-energy appears to be more sensitive.

5. Pseudogap

In the following, the new flow scheme of the self-energy is applied to the 2D-Hubbard model in order to study whether a pseudogap can be observed with fRG. In contrast to the conventional self-energy flow scheme, the new one actually is able to open a gap in the spectral function at the antinodal point. Therefore the introduction of the improved self-energy flow scheme is essential for future investigations of the pseudogap and the physics related to it.

5.1 Pseudogap in the Cuprates

The pseudogap is a feature of the hole-doped cuprates observed between the antiferromagnetic instability and the superconducting dome. Experimentally it can be observed by ARPES [14, 138] and was confirmed by scanningtunneling spectroscopy (STM) [40]. One observes that the spectral function is gapped at the antinodal momentum $\mathbf{k} = (\pi, 0)$ at zero frequency while the quasiparticle weight along the Brillouin-zone diagonal persists. Recent experiments using angle-dependent magnetoresistance suggest that nodal hole pockets constitute the Fermi surface [19]. The underlying mechanism is object of many experimental [113, 111] and theoretical [115, 98] studies.

As a theoretical model for the cuprates, the 2D Hubbard model at small but finite next-to-nearest neighbor hopping t'. In some studies, an additional next-to-next-nearest neighbor hopping t'' is equally included.

In hole-doped cuprates, the bare onsite interaction U is considered to be large. This strong-coupling scenario was studied in many different methods a selection of those being: DCA [51, 77, 27, 25, 28], cluster perturbation theory (CPT) [106], (cellular) CDMFT [71]. A comparison between TPSC, DCA, and CDMFT was performed in [115] including also considerations about weak coupling. Also at weak to intermediate coupling, the momentum selective gap opening could be observed in TPSC [123, 106, 32, 115], diagrammatic Monte Carlo (DiagMC) [136]. On the other hand, no gap could be found in CDMFT at weak coupling even at low temperatures. Only with increasing the interaction strength, pseudogap opened [26].

At the electron doped side, the coupling is considered to be less strong. Explicit studies of this case were performed with TPSC [70] and CPT [106].

Apart from these material driven calculations with realistic long-range hopping parameters t' and t'', the 2D Hubbard model at $t' = 0$ is often studied in order to gain insight in the performance of specific methods and general mechanisms for gap-opening tendencies. In this model, the half-filled case is particularly special as it provides perfect nesting. It was studied by TPSC [123] and through a comparison of DΓA, lattice QMC and VCA [101] mostly at weak to intermediate coupling. In the latter it was also proposed that the physics of spectral gap opening changes from Slater-like at weak to intermediate coupling to Heisenberg-like at strong coupling. In other works [123, 106, 72, 70, 32, 101, 136], the nature of the gap opening mechanism was studied using different model parameters. In summary, it was found that while at strong coupling the actual antiferromagnetic correlation length is less important, the weak-coupling mechanism requires this correlation to be long ranged. Even more generally, there are strong indications that the pseudogap originates from the antiferromagnetic correlations. The fluctuation diagnostics [29] of the self-energy through a channel selective application of the Schwinger-Dyson equation validates this theory. In the following study, the 2D Hubbard model at $t' = 0$, half-filling and weak coupling strength is considered.

In the fRG studies [139, 43, 41, 47, 58, 92, 117, 122], the pseudogap opening and momentum dependence of the quasiparticle weight depends on the specific parameter regime. Mostly a finite next-to-nearest neighbor hopping t' was considered. In this case, the gap could be observed at hole-doping, van Hove filling and only on the hot spots (momentum at which the Fermi-surface crosses the squared Fermi-surface of $t' = 0$ and half-filling) or antinodal points of the Fermi surface [92, 43, 58]. Moving away from van Hove filling or to other momenta on the Fermi-surface, the gap closes fastly. On the other hand, the study by Vilardi [122] which is the most similar to our implementation, does not find any gap opening or strong momentum dependence of the self-energy at any filling.

At electron doping, no reduction of the spectral weight was found [41] in direct contrast to the hole-doped case [43].

Without next-to-nearest neighbor hopping there are contradicting results: the quasiparticle weight is renormalized strongly at the antinodal and less at the nodal point according to Ref. [139] but no strong gap opening tendencies were found in Refs. [47] and [117]. The latter also reports that in the less nested case with $t' \neq 0$, there is no break-down of the Fermi-liquid, but the anisotropy in the quasiparticle weight increases.

The inconsistency in the findings can be explained by the different implementations. In particular, only in two cases a frequency dependent vertex was used [117, 122]. In the other works, the vertex is considered frequency independent and a straightforward application of the flow equations in the one-particle irreducible fRG scheme leads to a frequency independent self-energy. As conclusions regarding the opening of a gap can only be obtained from the frequency dependence of the self-energy, either the Wick-ordered fRG [92] was used, or the flow equation of the self-energy was altered by the insertion of the vertex flow [43, 41, 47, 58]. In all of these schemes, the flow equation is constructed by a fermionic two-loop diagram. Another approach for frequency independent calculations is the direct solution of a flow equation for the quasi-particle weight [139]. With frequency dependence, the straightforward one-loop diagram for the self-energy flow was used [117, 122] in both cases leading to a gap-less Fermi-surface. Furthermore, all studies except [122] are performed using an N-patch fRG. The former and this work are inspired by the TUfRG spirit, although only few form factors were considered.

Here, the TUfRG approach is used because it can describe long-range antiferromagnetic correlations enabling the weak-coupling mechanism for pseudogap physics. For a good resolution of the sharp antiferromagnetic peak in the magnetic vertex in momentum space, a fine transfer momentum grid is needed. This is provided in the TUfRG, where the transfer grid can be refined ad libitum while the fermionic momentum dependencies are described by fewer form factors. A previous study with full frequency dependence of the vertex and truncation to s-wave formfactors and additional d-wave form factor for the pairing channel did not find a significant momentum dependence in the quasiparticle weight [122]. This work is the first to find pseudogap physics in the framework of TUfRG.

It is observed that a gap can actually be found in TUfRG but this depends strongly on the actual implementation of the self-energy flow. In contrast to the convention self-energy flow, used also in Ref. [122], the SDE-inspired flow scheme leads to the observation of a pseudogap. This is also supported by a post-processing analysis of the self-energy by Vilardi [119]. While the flowing self-energy indicates Fermi liquid behaviour, he could observe a gap at the hot spot calculating the SDE at the end of the flow.

In addition, this study confirms the importance of the magnetic channel for pseudogap physics through the calculation of low-order $\overline{ph}$-diagrams and their contribution to the self-energy.

5.2 Pseudogap with different self-energy flow schemes

In the following, the fRG formalism is used to study the opening of a pseudogap in the 2D Hubbard model at half-filling. While the study does not claim quantitative correctness, it shows how a different flow scheme for the self-energy completely changes the qualitative behavior.

The following calculations are therefore restricted to one or few loops in the multiloop extension. Moreover, for the two-particle vertex only a single local s-wave form factor and a small number of frequencies were considered, verifying that an additional d-wave form factor as well as more frequencies do not qualitatively affect the results in the considered parameter regime. Specifically, the low frequency object depending on all three frequencies is restricted to 8 fermionic and 17 bosonic frequencies. The same numbers are used in the high-frequency asymptotics of one of the fermionic frequencies for the remaining bosonic and fermionic frequencies. The asymptotic of both fermionic frequencies is described by 513 bosonic frequencies. The transfer momentum parametrization follows the spirit of Fig. 2.7, where in addition to 16×16 momentum patches distributed on an equally spaced grid in the Brillouin zone, an finer 5×5 grid around the AF peak at $\mathbf{q} = (\pi, \pi)$ was taken into account. A more detailed convergence analysis is shown in Fig. 5.10.

In this qualitative study, it is convenient to use the interaction cutoff. As shown in Appendix B, the result at every scale Λ can be translated to the solution of a specific bare interaction U and the interaction dependence can be read off directly from one run. In the following, results and discussions are always presented through the rescaled self-energy $\Sigma(\Lambda^2 \tilde{U}) = \Lambda \Sigma_\Lambda(\tilde{U})$ and vertices $\Phi(\Lambda^2 \tilde{U}) = \Lambda^2 \Phi_\Lambda(\tilde{U})$ for an arbitrary $\tilde{U} = 4$. The flow is stopped at $\Phi_{\Lambda_{pc}}(\tilde{U}) >= 10^3$ and the pseudo-critical interaction is obtained through $U_{pc} = \Lambda_{pc}^2 \tilde{U}$.

In Sections 5.2.1 and 5.2.2, it is shown how the SDE-derivative approach favors the pseudogap opening, while the conventional flow does not. Explanations for this difference are finally given in Section 5.2.3.

5.2.1 Self-energy flow versus Schwinger-Dyson equation

In this section, results for the self-energy comparing the 1ℓ flow from Eq. (3.1) w.r.t. the derivative of the SDE in Eq. (3.5a) are shown. The flow of the two-particle vertices is explicitly restricted to the 1ℓ-truncation and also the multiloop corrections for the self-energy flow are neglected. In particular it is shown that using the SDE-derivative the long-range AF fluctuations lead to a gap opening.

For both schemes, the flow of the self-energy w.r.t. the flowing interaction U is displayed in Fig. 5.1, for an inverse temperature of $1/T = 10$. The left panel with the green data

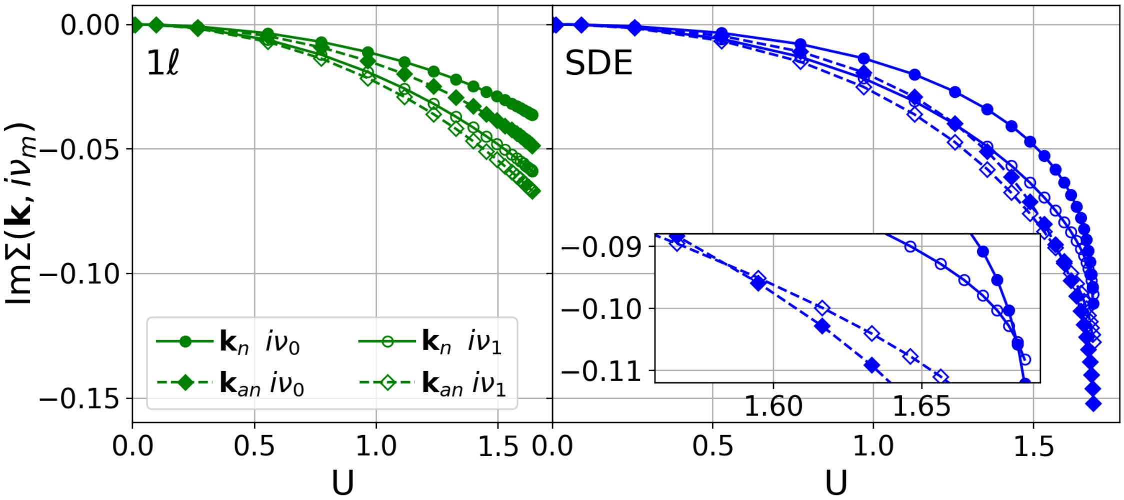

Figure 5.1: Self-energy as a function of the flowing interaction U for $1/T = 10$. Comparison of the nodal (solid lines) and antinodal directions (dashed lines) for the first two Matsubara frequencies in the conventional 1ℓ scheme (left panel) with the derivative of the SDE for the self-energy (right panel and inset). The crossings in the latter indicate the gap opening, occurring first in the antinodal and then in the nodal direction.

corresponds to the fRG calculation with the 1ℓ flow of the self-energy and the right one with the blue data to the scheme with the derivative of the SDE. The flow of the imaginary part of the self-energy is shown at the nodal $\mathbf{k}_n = (\pi/2, \pi/2)$ (circle symbols in the plot) and antinodal $\mathbf{k}_{an} = (\pi, 0)$ (diamond symbols) momentum point, both for the first (filled symbols, full lines) and second (open symbols, dotted lines) Matsubara frequencies.

The last data point on the right defines the so-called pseudo-critical interaction at which the flowing maximal component of all two-particle reducible vertices exceeds $\text{Max}\,\Phi_{r,\Lambda_{pc}}(\tilde{U} = 4) = 10^3$. In the 2D Hubbard model at half-filling, the diverging channel is $\Phi_{\overline{ph}}$ (compare also Section 4.3.2). In Fig. 5.2 this contribution to the vertex is plotted as a function of U. On a qualitative level, there are no big differences between the two schemes. The curves differ only at large U. In the conventional flow scheme, $\Phi_{\overline{ph}}$ grows

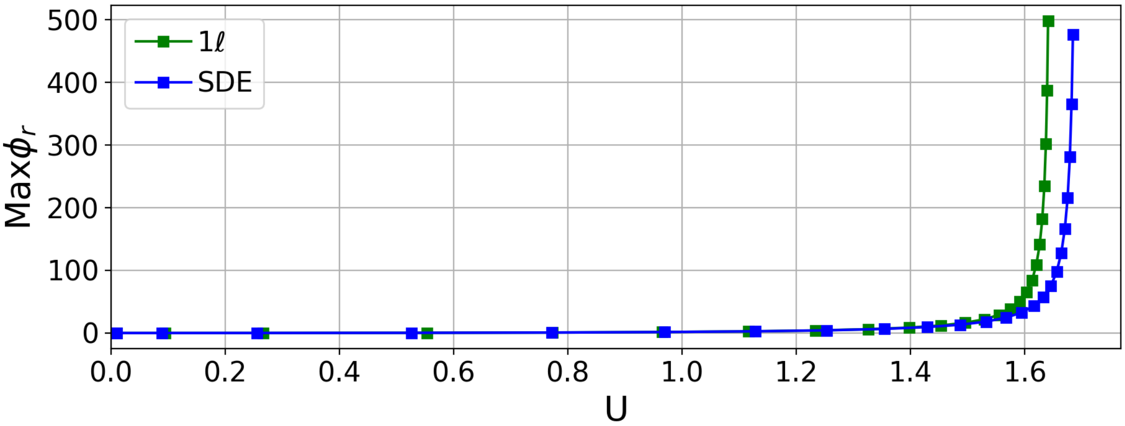

Figure 5.2: Maximal two-particle reducible channel $\text{Max}\,|\Phi_r| = |[\mathbf{\Phi}_{\overline{ph}}(\mathbf{q} = (\pi, \pi), i\omega_l = 0)]_{0\,0}|$ as a function of the flowing interaction U for $1/T = 10$.

first, leading to smaller pseudo-critical interaction $U = 1.64$ in the conventional flow than in the SDE scheme $U = 1.68$. This is consistent as the larger self-energy in the SDE scheme increases the screening of the $\overline{ph}$-excitations. In the SDE-scheme, crossings of the imaginary parts of the self-energy at the first and second Matsubara frequency can be observed which are not present in the conventional self-energy flow. At sufficiently low temperatures this is associated with a smooth, non-critical transition between a Fermi-liquid and an insulating behavior [107]. From the zoom in the inset of the right panel the bare interaction values of the crossing $U_n = 1.58$ for the nodal point and $U_{an} = 1.68$ for the antinodal point can be read out. The transitions occur only close to the pseudo-critical temperature and the order in which the pseudo gap opens first at the nodal and then at the antinodal point is consistent with the physics of the pseudogap regime. In the following the evolution and robustness of this feature in fRG is studied.

Restricted to the kinetic part, the model describes a Fermi-liquid of free quasi-particles. With increasing interaction, the quasi-particles become more and more correlated and the quasi-particle weight $Z(\mathbf{k}) \leq 1$ decreases in the coherent part of the spectral function

$$A(\mathbf{k}, \nu) = 2Z(\mathbf{k}) \frac{\Gamma(\mathbf{k}, \nu)}{(\nu + \mu - \epsilon_{\mathbf{k}})^2 + \Gamma(\mathbf{k}, \nu)^2} \tag{5.1}$$

where ν is a real frequency and $\Gamma(\nu, \mathbf{k}) \equiv Z(\mathbf{k}) \operatorname{Im} \Sigma(\mathbf{k}, \nu)$ is the scattering rate [73]. In the limit of vanishing imaginary part of the self-energy, $Z(\mathbf{k})$ describes the strength of the delta-peak of the spectral function at momentum $\mathbf{k}$ [78]. If the spectral function vanishes at the Fermi surface, a gap is opened. In two dimensions without true long range interaction, the full gap with exactly zero spectral weight is associated with long range ordering and is therefore only reached at zero temperature.

The quasiparticle weight [78]

$$Z(\mathbf{k}) = \left(1 - \frac{\partial \operatorname{Re} \Sigma(\nu, \mathbf{k})}{\partial \nu}\bigg|_{\nu \to 0}\right)^{-1}, \tag{5.2}$$

is related to the low real frequency behavior of the self-energy. Calculating in Matsubara frequencies, the self-energy on real frequencies has to be extracted through analytic continuation. Being an ill-posed problem, this is a hard and ambiguous task.

Avoiding analytic continuation, the distinction between gapped and Fermi-liquid solution is made directly using the imaginary part of the self-energy on Matsubara frequencies. The latter is antisymmetric around zero and negative for positive Matsubara frequencies. Note that the spacing between Matsubara frequencies is proportional to the temperature, making a low frequency analysis only meaningful for small enough temperatures. In order to illustrate the different behavior, the bare interaction U was fixed just below and just above the crossing points from Fig. 5.1 and the imaginary part of the self-energy as a function of the Matsubara frequency was analyzed in Fig. 5.3. The data for $U = 1.55$ show a Fermi-liquid behavior with a clear upturn towards zero at low frequencies in both the 1ℓ-scheme and the SDE-scheme. At the antinodal point in the SDE-scheme (blue diamonds), the self-energy is already bent away from the characteristic low frequency Fermi-liquid behaviour. The interaction value $U = 1.6$ is just above the one which opens a gap in the SDE-scheme and a slight downturn at the first frequency in the antinodal point of the SDE-scheme appears. The nodal point and the 1ℓ-scheme remain in the Fermi-liquid behaviour. At $U = 1.65$ the gap feature is even stronger. Note that for the observation of a gap at the nodal point in the SDE-scheme, one would have to tune the bare interaction very close to the pseudocritical scale.

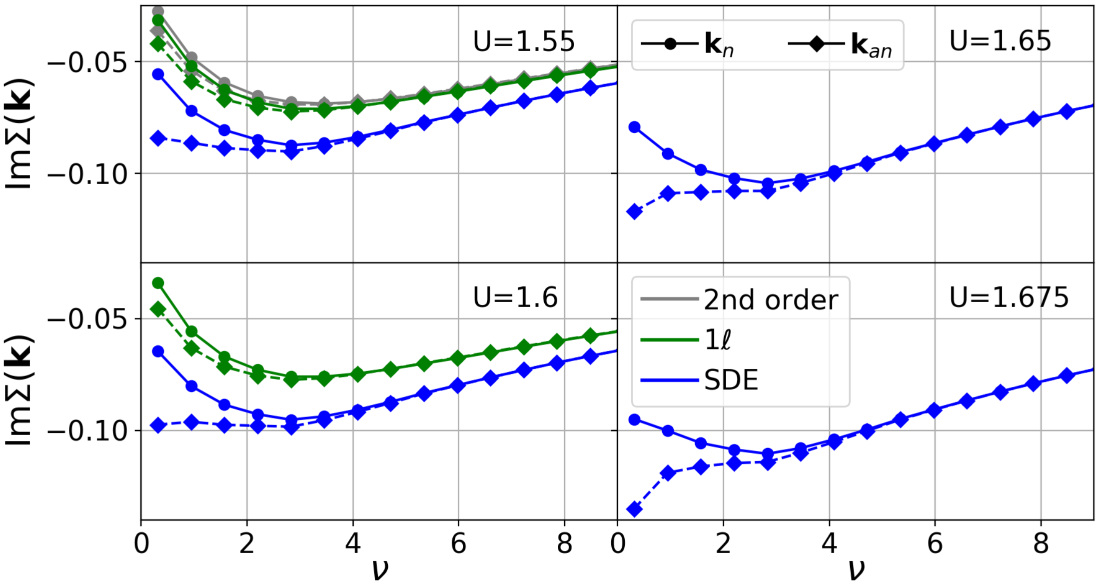

Figure 5.3: Self-energy as a function of the Matsubara frequency $i\nu_m$ for $1/T = 10$ and $U = 1.55$, $U = 1.6$, $U = 1.65$ and $U = 1.675$ just below and above the gap opening at the nodal (circles) and antinodal (diamonds) points. The results obtained in the conventional 1ℓ flow are shown in green, the ones from the derivative of the SDE in blue. Note that for $U = 1.65$ the 1ℓ flow is already diverged. For comparison, also the second-order perturbation theory for $U = 1.55$ is shown in gray.

The onset of a pseudogap can hence be detected by the crossing of the imaginary parts of the self-energy at the first and second Matsubara frequency (see also Refs. [101, 100, 107, 104]). Therefore, the difference between the latter is studied via

$$\partial_\nu \operatorname{Im}\Sigma(\mathbf{k}, i\nu_m)|_{i\nu_m = i\pi T} = \frac{\operatorname{Im}\Sigma(\mathbf{k}, i3\pi T) - \operatorname{Im}\Sigma(\mathbf{k}, i\pi T)}{2\pi T} \,, \tag{5.3}$$

with $\partial_\nu \operatorname{Im}\Sigma(\mathbf{k}, i\nu_m) \leq 0$ corresponding to the Fermi-liquid-like regime and

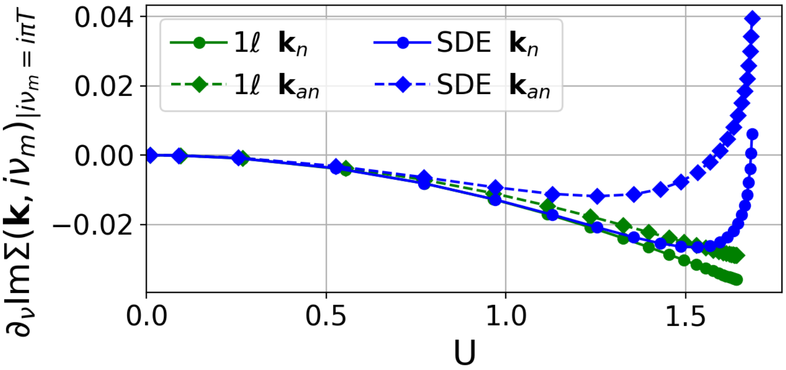

Figure 5.4: $\partial_\nu \operatorname{Im}\Sigma(\mathbf{k}, i\nu_m)$ evaluated at $i\nu_m = i\pi T$ as a function of the flowing effective interaction U for $1/T = 10$. The conventional 1ℓ self-energy flow (green) is compared to the one of the derivative of the SDE (blue). The latter crosses zero for both momentum points indicating the opening of a gap, while the conventional flow exhibits a monotonous behavior.

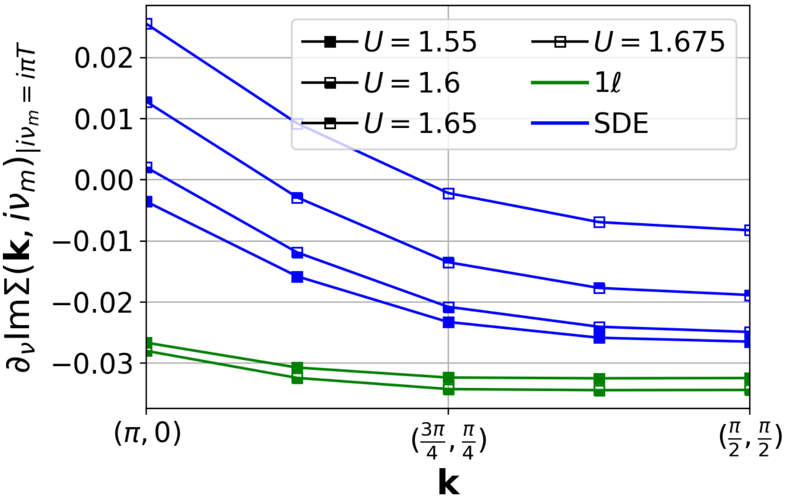

Figure 5.5: $\partial_\nu \operatorname{Im} \Sigma(\mathbf{k}, i\nu_m)$ evaluated at $i\nu_m = i\pi T$ as a function of the momentum on the Fermi surface.

$\partial_\nu \operatorname{Im} \Sigma(\mathbf{k}, i\nu_m) > 0$ to a (pseudo-)gap at momentum **k**.

In Fig. 5.4, the difference between the two flow schemes is plotted for the same parameters but this time using $\partial_\nu \operatorname{Im} \Sigma(\mathbf{k}, i\nu_m)_{|i\nu_m = i\pi T}$ as a function of U. The zeros in this quantity corresponds to the crossings of first and second Matsubara frequency in Fig. 5.1.

The momentum anisotropy, resulting in different gap opening interaction values for different momenta, is studied in Fig. 5.5. When leaving the antinodal and approaching the nodal momentum point $\partial_\nu \operatorname{Im} \Sigma(\mathbf{k}, i\nu_m)$ decreases monotonously. With increasing bare interaction, the factor is increased such that with $U = 1.6$, it finally crosses the zero value at the antinodal point. All together, the momentum dependence is very soft in the conventional flow scheme and only slightly more pronounced around the antinodal point in the SDE-flow scheme.

In Fig. 5.6, $\partial_\nu \operatorname{Im} \Sigma(\mathbf{k}, i\nu_m)$ is shown as a function of U and for different temperatures where $1/T = 10$ (dark red) is the temperature considered in Figs. 5.1 and 5.3 to 5.5 and $1/T = 18$ (yellow) is the lowest temperature used. The behavior is qualitatively the same: There is no gap in the 1ℓ-scheme while in the SDE-scheme, first a pseudogap opens at the antinodal point and shortly before the pseudo-critical interaction, the gap opens also at the nodal point.

The difference of the self-energy shape is shown again in Fig. 5.7 for different temperatures and at the temperature dependent pseudo-critical interaction $U_{pc}(T)$. In the conventional scheme (left panel), the self-energy tends towards small values at small frequencies and the form and size changes only slightly with temperature. More temperature dependence can be observed in the SDE-flow scheme (right panel). Note that because of the higher pseudo-critical interaction, the highest temperature shows the largest imaginary part of the self-energy.

From the zero-crossing of $\partial_\nu \operatorname{Im} \Sigma(\mathbf{k}, i\nu_m)$ in Fig. 5.6, the gap opening bare interaction can be extracted. The dependence of the latter from the temperature is reported in the left panel of Fig. 5.8. Dashed line and diamond symbols represent the gap opening interaction at the antinodal point and full line and blue dots at the antinodal point. Gray squares which lie just below the gap opening at the nodal point indicate the pseudo critical interaction, at which the $\overline{ph}$-channel exceeds the critical value and the flow has

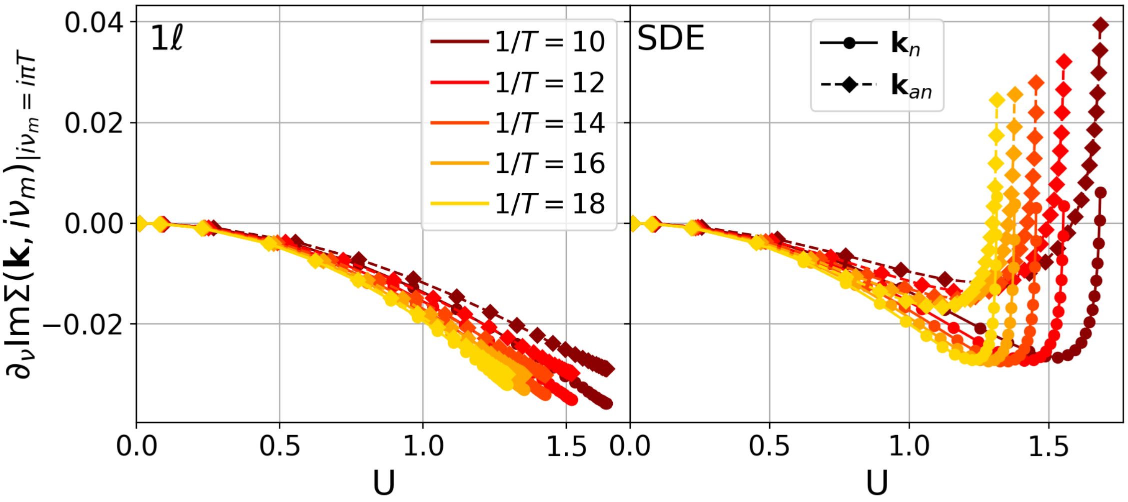

Figure 5.6: $\partial_\nu \operatorname{Im}\Sigma(\mathbf{k}, i\nu_m)$ evaluated at $i\nu_m = i\pi T$ as a function of the flowing interaction U for different temperatures. Using the conventional 1ℓ self-energy flow (left panel), no gap opening occurs for any temperature, while the SDE-flow scheme (right panel) yields a gap opening. The pseudo-critical and gap opening interactions decrease with decreasing T.

been stopped. The gap opening at the antinodal point is fairly stable. It approaches the pseudo-critical interaction for smaller temperatures but it is bending such that it does not cross the pseudo-critical line. On the other side, the nodal gap opening occurs just below the pseudo-critical scale for all interactions. Considering that the exact position of the gap opening interaction is still depending on the exact parametrization of the vertex (compare Fig. 5.10), no final conclusion for the nodal gap opening can be deduced from this data alone. However, as the parquet solution predicts a gap opening for the nodal point at $U = 2$ and $1/T = 30$ even for one local form factor [18], one expects also a gap at

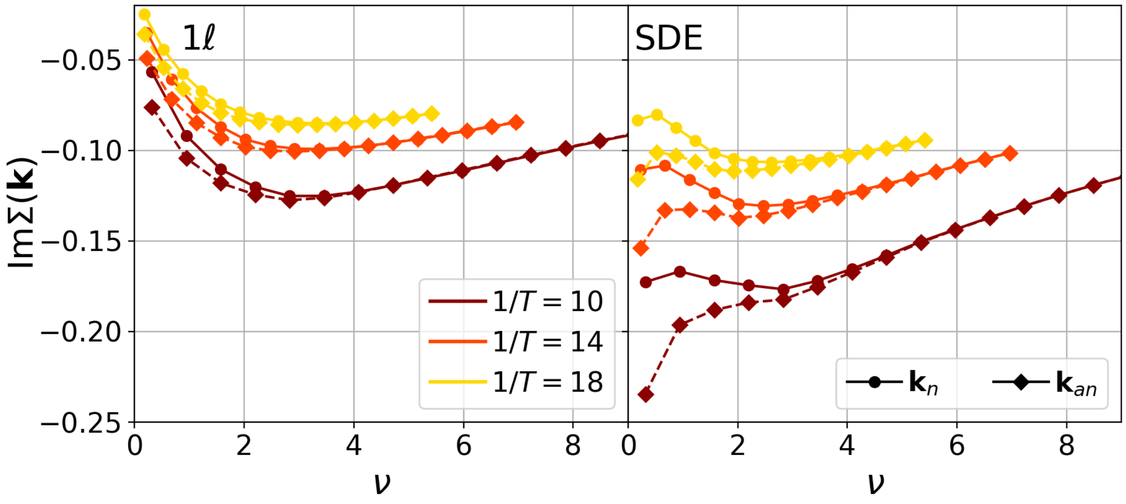

Figure 5.7: Self-energy as a function of the Matsubara frequency $i\nu_m$ for selected temperatures at the pseudo-critical interaction $U_{pc}(T)$. The left panel shows the results obtained in the conventional 1ℓ flow and the right one in the SDE-approach.

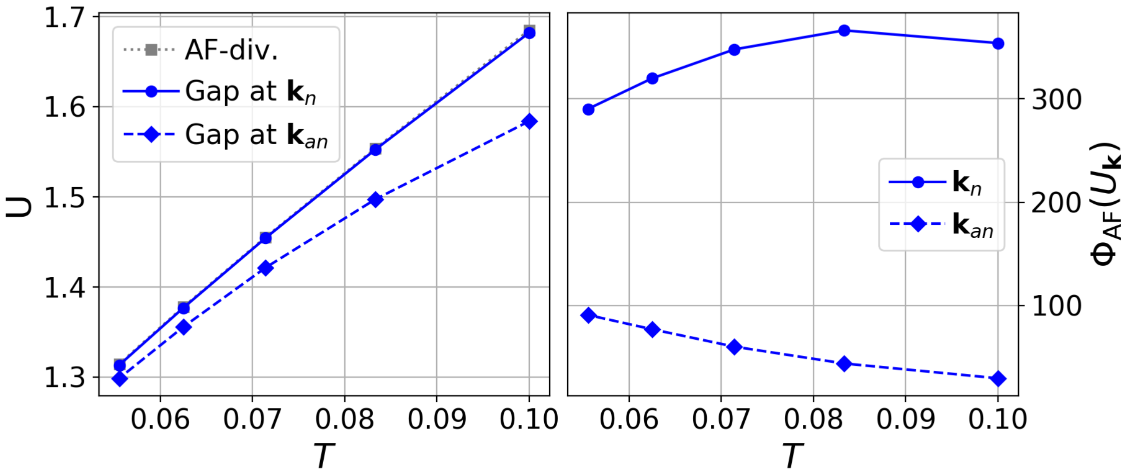

Figure 5.8: Flowing effective interaction U at which the gap opens (left panel) and $\overline{ph}$-reducible vertex at $\mathbf{k} = (\pi, \pi)$ and $i\omega_l = 0$ at the gap opening interaction (right panel) as a function of the temperature. The antinodal point (blue diamonds) and the nodal one (blue dots) are shown. The gap opening interaction of the latter is almost on top of the AF-divergence (grey squares).

the nodal point for fully converged results in momentum, frequency and loop order and suitable physical parameters.

In the right panel of Fig. 5.8 the maximum two-particle reducible channel is shown at the interaction at which the gaps at the antinodal (blue diamonds) and the nodal (blue dots) open. At half-filling considered here, this is always the $\overline{ph}$-channel at $\mathbf{k} = (\pi, \pi)$ and $i\omega_l = 0$ denoted Φ_{AF} due to its close relation to the antiferromagnetic vertex. The effective interaction needed for the gap opening at the antinodal point is almost two orders of magnitude higher than the bare interaction and increases for smaller temperatures. The

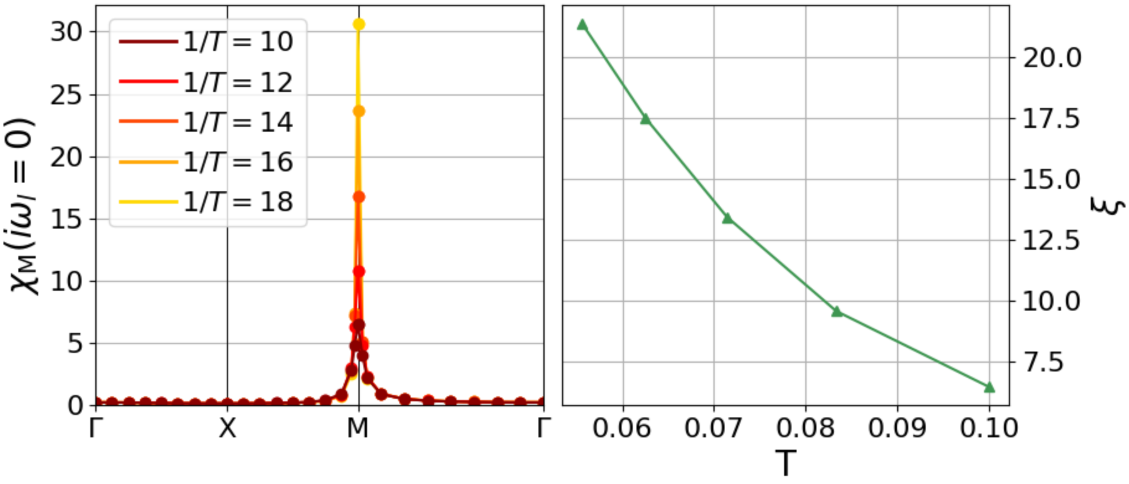

Figure 5.9: Magnetic susceptibility (left panel) and AF correlation length (right panel) at different temperatures and the bare interaction at which the gap at the antinodal point opens $U_{\mathrm{an}}(T)$. For lower temperatures, a large AF peak and longer correlations are needed to open the pseudogap.

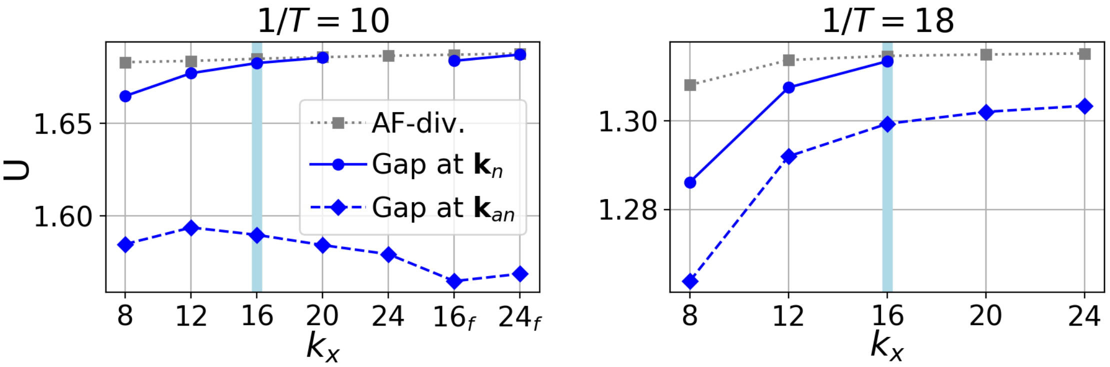

Figure 5.10: Flowing effective interaction U at which the gap opens as a function of the number of momenta k_x (with $k_y = k_x$) accounted for in the two-particle vertex, for $1/T = 10$ (left panel) and $1/T = 18$ (right panel). The gap at the antinodal point (blue diamonds) always opens before the AF-divergence (grey squares) sets in, while the gap at the nodal point (blue dots) vanishes with increasing resolution of the Brillouin-zone. All other calculations are performed for $k_x = 16$ (light blue line).

same conclusion is obtained from the peak of the magnetic susceptibility shown in the left panel of Fig. 5.9. For this comparison, the calculations were performed at the temperature T and with the interaction $U_{\mathrm{an}}(T)$ which opens the antinodal gap and depends on temperature according to Fig. 5.8. A strong AF peak can be observed for all temperatures and for lower temperatures, the strength of the AF susceptibility is much larger at the gap opening. Also the correlation length obtained through fitting of Eq. (4.6) on χ_{M} (also here within the distance of 0.3π from M) is shown in the right panel of Fig. 5.9. Also ξ increases at the gap opening interaction for lower temperatures. It follows that the gap opening mechanism is not only related to the strength and correlation length of the antiferromagnetic channel but, much more subtle.

Finally, the robustness of the pseudogap w.r.t. the technical parameters is discussed. While no qualitative difference is observed including more frequencies or form factors, the convergence in terms of momentum points is more subtle as shown in Fig. 5.10. The results shown previously are always calculated with 16×16 bosonic momentum patches distributed on an equally spaced grid over the entire Brillouin-zone. In addition, a finer patching around the antiferromagnetic peak at $q = (\pi, \pi)$ is applied analogously to Fig. 2.7. This configuration is indicated by the light blue vertical line in Fig. 5.10. For this study, first the number of bosonic patching points is increased, leading at the same time to a shrinking fine patching region. At $1/T = 10$ it seems that with more patching points the gap opening at the nodal point shifts to higher scales than the pseudo-critical scale. But a more extended refinement (subscript f), including 15×15 patching points and covering a 3×3 larger area, brings back the gap opening. The reason therefore is that the peak is still quite large at $1/T = 10$ but the region covered by fine patching decreases with increasing k_x such that it becomes smaller than the peak width. Also the value of interaction, at which the gap opens at the antinodal point, varies with the patching. Still, the difference is within a few percent and remains distant to the pseudo-critical interaction. While at $1/T = 10$, with single refinement, the scale even decreases with the patch number, it has a monotonous behaviour at $1/T = 18$. At these low temperatures, the AF peak is so thin that the fine patching region still covers all of it even with $k_x = 24$.

Therefore, the question whether in the low-temperature regime the gap opening at the nodal point is stable would require a more refined convergence analysis.

5.2.2 Towards full multiloop fRG

In the 1ℓ truncation, the conventional flow of the self-energy and the SDE-flow scheme differ in two main aspects. The first consists of the form factor truncation explained in Chapter 3 and reconsidered in Section 5.2.3 below and the second is the loop truncation of the flow equations. Extending the calculation to more loops, the same qualitative picture of the gap opening suggests that the loop truncation is not the main reason for the self-energy flow scheme difference. Another reason to study the multiloop extension is the decreasing pseudo-critical interaction giving in principal more space to the pseudogap to develop. At least for the parameter range considered here, a larger pseudogap region is not confirmed.

The precise form of the multiloop equations is reported in Chapter 2. In the SDE-flow for the self-energy, both the 1ℓ-equation and multiloop corrections of the self-energy are replaced by Eq. (3.5a) according to the scheme presented in Chapter 3. The loop order N_ℓ is specified for every calculation and the self-energy iterations are neglected ($N_{\Sigma\text{-iter}} = 0$) as they lead only to quantitative corrections. This means that the Katanin-substitution in the SDE-flow scheme is always performed with the conventional 1ℓ-flow for the self-energy.

Also in the multiloop extension of the flow equations, the scale at which the interaction flow diverges can be translated into a pseudo-critical interaction. The proof for this can be found in Appendix B. This allows to plot $\partial_\nu \operatorname{Im}\Sigma(\mathbf{k}, i\nu_m)$ from one single run as a function of the bare interaction.

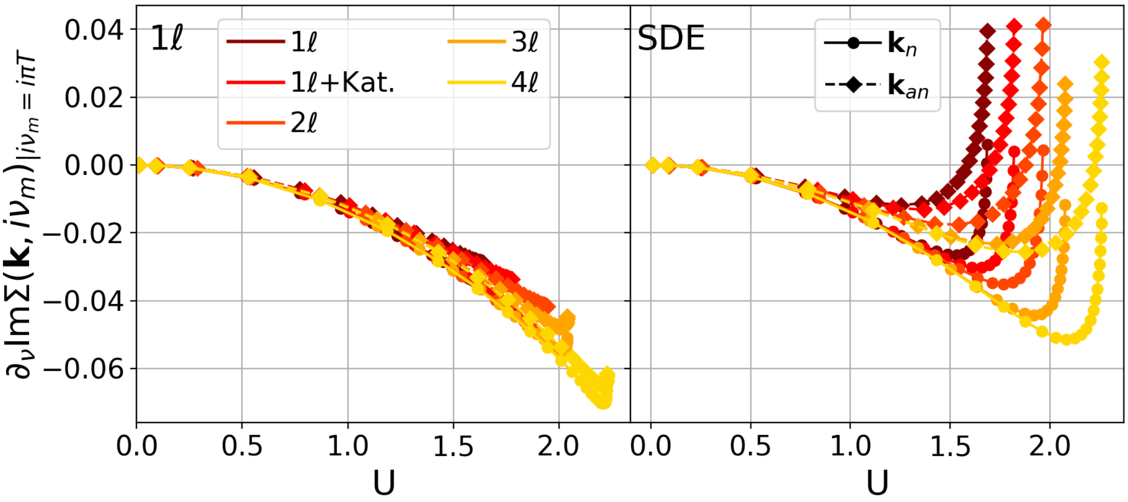

Figure 5.11: $\partial_\nu \operatorname{Im}\Sigma(\mathbf{k}, i\nu_m)$ evaluated at $i\nu_m = i\pi T$ as a function of the flowing interaction U, for $1/T = 10$ and different loop orders ℓ, both in the conventional fRG (left panel) and the SDE-flow scheme (right panel). In the conventional fRG no zero crossing is observed but there is a tendency towards gap opening very close to the pseudo-critical temperature. In the SDE-approach, the gap opening at the antinodal point is observed also at higher loop order, while the gap at the nodal point vanishes with increasing ℓ. The gap opening scales and the onset of the AF divergence are directly compared in Fig. 5.12 including higher loop orders.

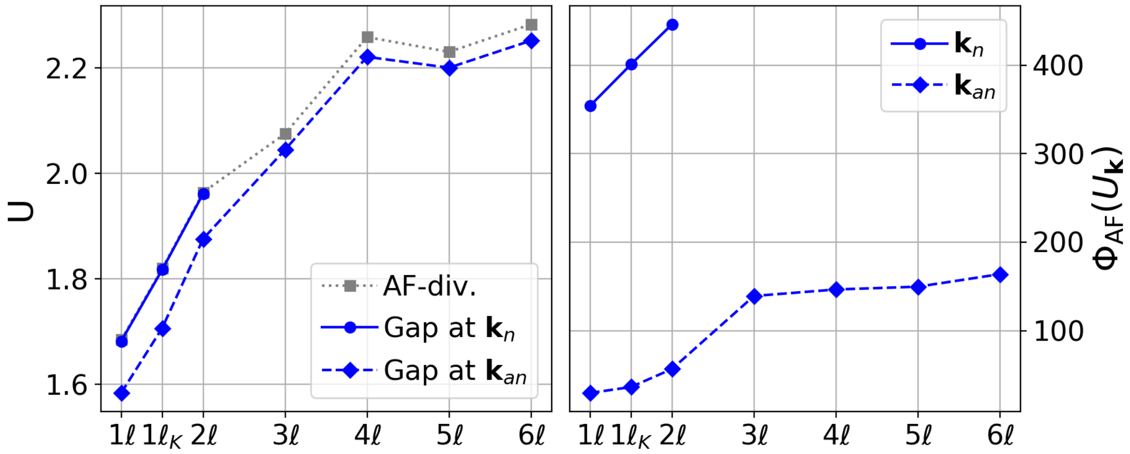

Figure 5.12: Flowing interaction U at which the gap opens (left panel) and $\overline{ph}$-reducible vertex at $\mathbf{k} = (\pi, \pi)$ and $i\omega_l = 0$ at the gap opening interaction (right panel) as a function of the loop order ℓ, for $1/T = 10$. The gap opening at the antinodal point (blue diamonds) always occurs before the AF divergence (grey squares), while the gap opening at the nodal point (blue dots) disappears into the pseudo-ordered phase at higher loop order. The pseudo-critical interaction shows the characteristic oscillatory behavior at high loop order.

In Fig. 5.11, $\partial_\nu \operatorname{Im} \Sigma(\mathbf{k}, i\nu_m)$ is shown as a function of the flowing interaction U, at fixed temperature $T = 1/10$ and different loop orders ℓ. The pseudo-critical scale increases with loop order in both self-energy flow schemes in accordance to the results in Chapter 4. While in the conventional fRG no gap opens at any loop order, in the SDE-flow scheme, the gap opening at the antinodal point persists and is shifted to higher interaction values with higher loop order. In the SDE scheme and at 3ℓ, the gap at the nodal point disappears in the pseudo-ordered regime and does not recover at higher loop orders. A direct comparison of the gap opening interaction and the onset of the AF divergence is shown in the left panel of Fig. 5.12, as a function of the loop order. The trend towards higher pseudo-critical interactions can again be observed already. Also higher loop orders are displayed, showing the characteristic oscillatory behavior of the loop convergence [110]. Also the expectation that larger pseudo-critical interactions would leave more space for the pseudogap to develop, can be disproved for these parameters. The gap at the nodal point vanishes at higher loop order, while at the antinodal point sets in at a rather small but constant distance from the pseudo-critical line. The fact that the gap opening at the antinodal point persists shows that the gap opening tendency is not loop-order dependent. Therefore the only remaining difference between the 1ℓ and SDE scheme is the form-factor truncation. In the right panel of Fig. 5.12, the maximal two-particle reducible channel at the gap-opening interaction is shown. There is a jump between 2ℓ and 3ℓ, while for higher loop orders the strength remains virtually constant.

The gap-opening interaction was also studied directly in PA in Ref. [18] and does not contradict the fRG findings in this work. In PA, a pseudogap occurs at $1/T = 26$ and a full gap at $1/T = 30$ for the only studied bare interaction $U = 2$. These temperatures are presently difficult to access within a multiloop fRG calculation, due to the required refinement of the momentum and frequency dependence of the two-particle vertex and the high number of loop orders needed for convergence. From Fig. 5.8 it can be deduced that the pseudo-critical and the gap opening interactions decrease with temperatures and from Fig. 5.12 that the latter increases with loop order. The combination of the two effects should lead to the pseudogap opening interactions in parquet.

5.2.3 Analysis of approximation in TUfRG

In the following, the effect of the form factor truncation on the opening of a pseudogap is studied. The difference of the conventional self-energy flow and the SDE-flow in the TUfRG was already discussed in Chapter 3. Those insights are used also here together with a very simple analysis on the gap opening mechanism.

As a first step, it is argued that the $\overline{ph}$-channel drives the gap opening. Due to the channel separation in fRG, the contributions of the other channels can be easily suppressed. The result is shown in Fig. 5.13. Setting the particle-particle channel to zero (orange) or setting both the direct particle-hole and particle-particle channel to zero does not open a gap in the 1ℓ scheme and preserves the gap at the antinodal point in the SDE scheme. If only the $\overline{ph}$-channel is taken into account, no gap occurs at the nodal point. However, it was argued in Section 5.2.1 that the gap opening at this momentum is unstable w.r.t. the momentum patching points and the loop order.

The role of the $\overline{ph}$-channel $\Phi_{\overline{ph}}$ for the gap opening is analyzed in the following simplified study. For a more detailed discussion, see also Refs. [123, 1] and [84]. At half-filling, the $\overline{ph}$-channel, which is closely related to the magnetic channel according to Eq. (2.58), dominates the physics. In a finite loop flow it diverges at a pseudo-critical interaction. In

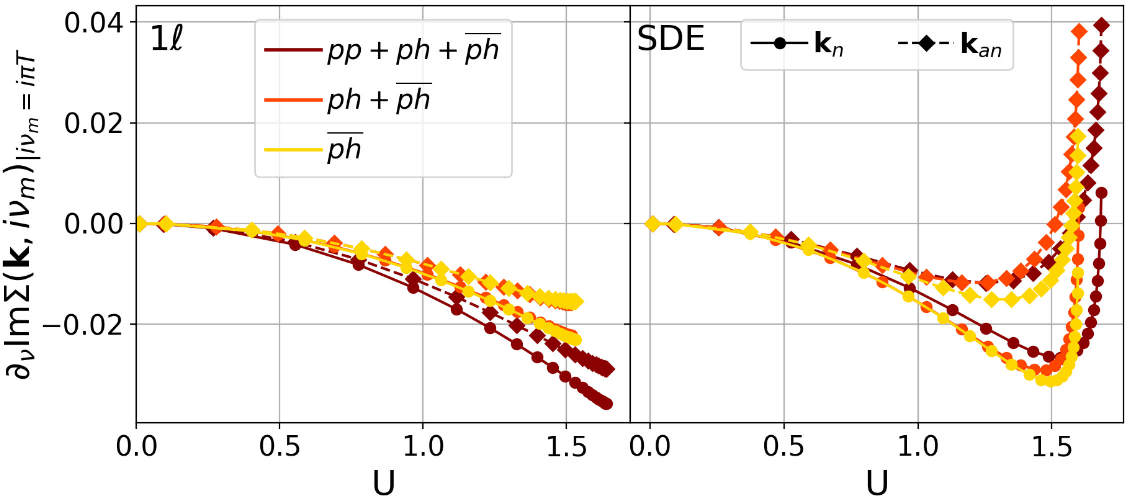

Figure 5.13: $\partial_\nu \operatorname{Im} \Sigma(\mathbf{k}, i\nu_m)$ evaluated at $i\nu_m = i\pi T$ as a function of the flowing interaction U for $1/T = 10$ and different channel approximations, both with the conventional fRG (left panel) and the SDE-approach for the self-energy flow (right panel). Neglecting the pp- and ph-channels does not qualitatively affect the appearance of the gap opening at the antinodal point. At the nodal point, the gap opening is unstable and depends on the parametrization.

this limit, the contribution

$$
\begin{aligned}
\Sigma_{\overline{ph}}(\mathbf{k}, i\nu_m) = &- \sum_{\mathbf{k}' i\nu_{m'}} \sum_{n} f_n^*(\mathbf{k}) f_0(\mathbf{k}) G^{\Lambda}(\mathbf{k}', i\nu_{m'}) \\
&\times \sum_{i\nu_{m''}} \Big[\mathbf{\Phi}^{\Lambda}_{ph}(\mathbf{k}' - \mathbf{k}, i\omega_{m'-m}, i\nu_{m+\lfloor \frac{m'-m}{2} \rfloor}, i\nu_{m''}) \mathbf{\Pi}^{\Lambda}_{ph}(\mathbf{k}' - \mathbf{k}, i\omega_{m'-m}, i\nu_{m''}) \mathbf{U} \Big]_{n\,0}
\end{aligned}
\tag{5.4}
$$

dominates over all others in Eq. (3.3). Close to the divergence, $\Phi_{\overline{ph}}$ exhibits a very strong s-wave component such that other form-factor contributions can be neglected, yielding

$$
\begin{aligned}
\Sigma_{\overline{ph}}(\mathbf{k}, i\nu_m) \approx &- \sum_{\mathbf{k}' i\nu_{m'}} G(\mathbf{k}', i\nu_{m'}) U \\
&\times \sum_{i\nu_{m''}} \Big[\mathbf{\Phi}_{\overline{ph}}(\mathbf{k}' - \mathbf{k}, i\omega_{m'-m}, i\nu_{m+\lfloor \frac{m'-m}{2} \rfloor}, i\nu_{m''}) \Big]_{0\,0} \Big[\mathbf{\Pi}_{ph}(\mathbf{k}' - \mathbf{k}, i\omega_{m'-m}, i\nu_{m''}) \Big]_{0\,0} .
\end{aligned}
\tag{5.5}
$$

This equation can be written in a more compact form

$$
\begin{aligned}
\Sigma_{\overline{ph}}(\mathbf{k}, i\nu_m) \approx &- \sum_{\mathbf{k}' i\nu_{m'}} \Big[\Big[\boldsymbol{\mathcal{K}}_{2,\overline{ph}}(\mathbf{k}' - \mathbf{k}, i\omega_{m'-m}, i\nu_{m+\lfloor \frac{m'-m}{2} \rfloor}) \Big]_0 + \mathcal{K}_{1,\overline{ph}}(\mathbf{k}' - \mathbf{k}, i\omega_{m'-m}) \Big] \\
&G(\mathbf{k}', i\nu_{m'}) ,
\end{aligned}
\tag{5.6}
$$

using the high frequency asymptotics of the two-particle vertex [129]. Here, $\mathcal{K}_{1,\overline{ph}}$ which is proportional to the crossed-particle hole or to the (negative) magnetic susceptibility, yields the strongest contribution and is further approximated by

$$
\begin{aligned}
\mathcal{K}_{1,\overline{ph}}(\mathbf{k}' - \mathbf{k}, i\omega_{m'-m}) &\approx \delta_{\mathbf{k}'-\mathbf{k}=(\pi,\pi)} \delta_{m,m'} \mathcal{K}_{1,\overline{ph}}((\pi,\pi), 0) \\
&\approx -2 \delta_{\mathbf{k}'-\mathbf{k}=(\pi,\pi)} \delta_{m,m'} \chi_{AF} ,
\end{aligned}
\tag{5.7}
$$

leading to the following expression for the self-energy

$$
\Sigma_{\overline{ph}}(\mathbf{k}, i\nu_m) \approx 2\chi_{AF} G(\mathbf{k} + (\pi,\pi), i\nu_m) \approx 2\chi_{AF} \frac{1}{i\nu_m + \epsilon_{\mathbf{k}+(\pi,\pi)}} .
\tag{5.8}
$$

For momenta on the Fermi surface $\epsilon_{\mathbf{k}+(\pi,\pi)} = 0$, the $\overline{ph}$-contribution to the imaginary part of the self-energy is $-2\chi_{AF}/(\pi T)$ for the first and $-2\chi_{AF}/(3\pi T)$ for the second Matsubara frequency. For all these momenta, this approximation leads to $\partial_\nu \operatorname{Im} \Sigma(\mathbf{k}, i\nu_m) = 2\chi_{AF}/(3\pi^2 T^2) > 0$. For comparison, $\operatorname{Im} \Sigma(\mathbf{k}, i\nu_m = i\pi T) = -2\pi T \chi_{AF}/(\pi^2 T^2 + 16)$ and $\operatorname{Im} \Sigma(\mathbf{k}, i\nu_m = i3\pi T) = -6\pi T \chi_{AF}/(9\pi^2 T^2 + 16)$ is estimated for the momenta $\mathbf{k} = (0,0)$ and $\mathbf{k} = (\pi,\pi)$, with $\epsilon_{(0,0)} = -\epsilon_{(\pi,\pi)} = -4$. In this simplified analysis, $\partial_\nu \operatorname{Im} \Sigma$ at these momenta is negative for $T > \frac{4}{\sqrt{3}\pi} = 0.735$. At higher temperatures, the qualitative form of the self-energy differs strongly for momenta on and far away from the Fermi surface already in this very simplified analysis. Note that this analysis does not explain the anisotropy between momenta on the Fermi surface like the nodal and antinodal point.

The self-energy in Eq. (5.8) basically coincides with the phenomenological ansatz of Eq. (7) in Yang, Rice and Zhang [137]. This indicates that the phenomenology arising from the numerical study here may indeed be useful to explain pseudogap features in correlated materials like high-temperature superconductors.

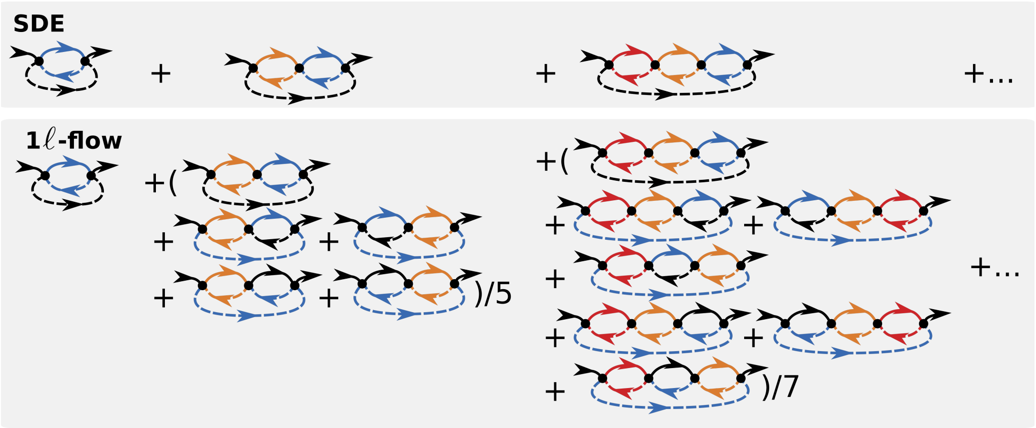

Figure 5.14: Comparison of lowest order diagrams describing the contribution of the $\overline{ph}$-channel to the self-energy, in the SDE-approach (above), and in the conventional 1ℓ-approach (below). The result up to 4th (7th) order is displayed in the left (right) panel of Fig. 5.15, while the gap opening as a function of order in U is provided in Fig. 5.16.

This explanation is supported by the following low order analysis of selected diagrams. Those contributing to the self-energy in the SDE scheme through the $\overline{ph}$-channel (green boxes in Fig. 3.2) are confronted to the ones of the same topology in the conventional self-energy flow (green boxes in Fig. 3.3). The latter are in part badly approximated because of the form-factor truncation. The diagrams are summarized in Fig. 5.14 up to forth order and are weighted such that the total weight of diagrams belonging to the same topology is the same as in the SDE-scheme. Higher orders are straightforward to obtain. The calculation of these diagrams can be performed for $U = 1$ and the dependency on the

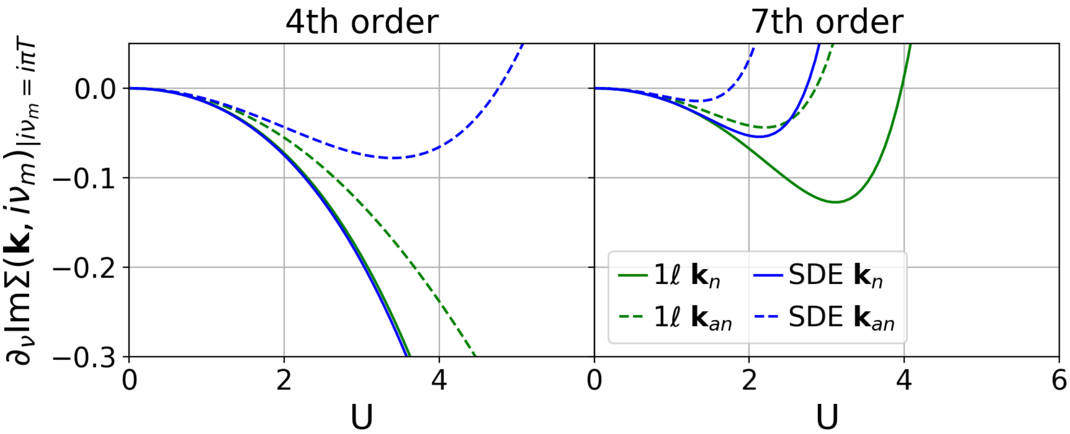

Figure 5.15: $\partial_\nu \, \mathrm{Im}\, \Sigma(\mathbf{k}, i\nu_m)$ evaluated at $i\nu_m = i\pi T$ resulting from the contributions of the $\overline{ph}$-channel up to the 4th and 7th order in U, as illustrated in Fig. 5.14. While at the second order no gap opens, starting from the 3rd both approaches lead to a gap opening at the nodal and antinodal point at some large value of U (not shown). At the 4th order, the SDE-approach opens a gap at the antinodal point first. At the 7th order, one can already see that both approaches open a gap first at the antinodal point and later at the nodal one. In SDE-approach both gaps open before the first gap opening in the conventional 1ℓ flow. For a study of the gap opening as a function of order in U see Fig. 5.16.

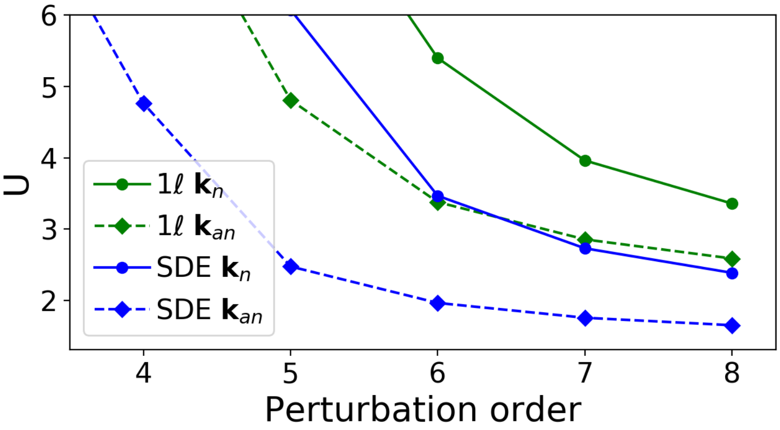

Figure 5.16: Gap opening as a function of order in U as extracted from $\partial_\nu \operatorname{Im}\Sigma(\mathbf{k}, i\nu_m)$ evaluated at $i\nu_m = i\pi T$, resulting from the contributions of the $\overline{ph}$-channel only. With increasing order, the gap opening occurs at lower values of U. The gap at the antinodal point in the SDE-approach opens first and then the gap at the nodal point, consistently with the full calculation in Fig. 5.4. The gaps in the 1ℓ-approach open even later. The pseudo-critical interaction cannot be shown in this approach as a divergence of the vertex occurs only at infinite order.

interaction is then recovered by the multiplication of the correct order in U.

In Fig. 5.15, $\partial_\nu \operatorname{Im}\Sigma(\mathbf{k}, i\nu_m)$ is shown as a function of U summing the diagrams reported in Fig. 5.14 up to 4th (left panel) and 7th order (right panel). The shape resembles the one of the full fRG calculation in Fig. 5.4 with an initial downturn and a rapid upturn at high interactions. Due to the separated calculation of the different orders in U, the downturn of $\partial_\nu \operatorname{Im}\Sigma(\mathbf{k}, i\nu_m)$ can be related to the second order diagram. The higher order contributions act against the downturn such that $\partial_\nu \operatorname{Im}\Sigma(\mathbf{k}, i\nu_m)$ always crosses the zero value.

The diagrams with the correct form-factor approximation show the strongest upturn tendency. Further, the antinodal point has more tendency to open a gap than the nodal point. Therefore at 4th order, one can observe the zero crossing in the SDE-scheme at the antinodal point at $U = 4.7$, while all other lines cross only at higher interaction U. Going to higher orders, the zero crossing shifts to smaller interactions. At 7th order the gap is first opened in the SDE-scheme starting from the antinodal and then at the nodal point. In the 1ℓ-scheme, where the correct form-factor approximation is mixed with less favorable ones, the gap is opened at higher U, again first at the antinodal and then at the nodal point. The gap opening interaction according to the simplified 4th to 7th order analysis is reported in Fig. 5.16. Note that the gap opening here sets in at much higher interactions because in fRG diagrams are summed up to infinite order. Also, no pseudo-critical interaction can be obtained at any finite order in perturbation theory. Despite these limitations, the low interaction order analysis illustrates the order in which the gap opening occurs surprisingly well.

This analysis also explains why some fRG studies find strongly reduced quasi-particle weight or even a pseudogap and others do not. Ref. [117, 122] used the conventional flow for the self-energy for which it is more difficult to open a gap. As it can be expected from the explanation above, the post-processing application of the SDE in Ref. [119] found a gap feature. Reduced quasi-particle weight could also found in Ref. [47, 58], where the vertex flow is reinserted in the self-energy flow equation in order to recover a frequency dependent self-energy from a static vertex. This leads to an equation with three fermionic Green's functions, formally very similar to the SDE. Also in the Wick-ordered flow of the self-energy applied in [92], a nested fermionic loop appears reminding of the structure of the SDE. However, for future quantitative studies of the pseudogap, the here presented dynamic multiloop fRG approach should be applied with SDE-like flow equation for the self-energy.

6. Conclusion and Outlook

In this work, the fRG has been developed from a qualitative to a quantitative method. The first important step for the quantitative improvement has been the realization of an efficient parametrization of the vertex simultaneously in frequencies and momenta. In practice, this has been realized by a combination of the high-frequency asymptotics and the TUfRG. Time consuming parts of the code have been optimized, in particular the calculation of the fermionic excitation and the projection from one channel to another. The freed capacities have been used to include the self-energy flow equation as well as its feedback to the vertices. At this point, a convergence study on the 2D Hubbard model has been performed leading to the observation that, at $t' = 0$ and half-filling, the results converge fast in frequencies and sufficiently fast in momenta. From the study of different common approximations, it has been concluded that the full fRG approach with converged vertex parametrization and feedback of the self-energy leads to the lowest pseudo-critical temperatures.

Next, the multiloop extension has been implemented both for the vertices and self-energy. The evolution of intermediate and final results w.r.t. to the loop order has been studied finding convergence to a flow scheme independent result and susceptibilities satisfying exact relations. Concerning the self-energy, a new flow equation was introduced in order to fulfil the corresponding exact relation, namely the SDE, in TUfRG. It allows to obtain convergent results with a finite number of form factors, unlike the conventional flow equation.

With these tools, a benchmark study was performed in which fRG was compared to PA and dQMC. With the new flow equation for the self-energy, deviations between the antiferromagnetic susceptibility obtained by PA and fRG were below 1% up to an interaction strength $U = 1.5$ (for $t' = 0$ and half-filling). The increasing difference between these formally equivalent methods for larger U is a consequence of different technical implementation details which become more prominent near critical parameters. Considering the comparison of several susceptibilities and of the self-energy, fRG and PA compare also very well with dQMC which was verified at half-filling and at finite doping for interaction strengths below $U \leq 3$. The deviation between PA and dQMC scaling as $\mathcal{O}\big[U^4\big]$ is predicted by the parquet approximation $V_{2\mathrm{PIR}}(k_1, k_2, k_3) \approx U$.

Besides the validation of the presented implementation and a proof of principle of convergence towards other methods, the presented study provides a guideline for the parameter setup in future realistic calculations. When setting up a new system, convergence tests for the parametrization in frequencies, momenta and form-factors as well as the number of loops and self-energy iterations should be performed. A rough estimate of those can be deduced from the study here. For the calculation of spectral properties, the SDE-like flow scheme for the self-energy above all when spectral properties is essential. However, quantitative model studies are not always in need and sometimes a perfect vertex parametrization and convergence in loops is numerically out of reach. This is in particular the case for more complex systems involving additional quantum numbers or for more challenging parameter regimes at lower temperatures. For instance, a simple instability study could be restricted to the 1ℓ-approach with conventional self-energy flow. The resulting pseudo-critical scale should however be presented with care as the here presented results indicate that it is further suppressed by the full multiloop extension.

On top of this successful technical development, this work also addresses fundamental physical questions. Among those is the improved fulfilment of the Mermin-Wagner theorem [81] which states that there is no spontaneous symmetry breaking at finite temperature in a two-dimensional system without long-range interactions. First of all, the implementation of the full frequency dependence and feedback of the self-energy leads to a smaller pseudo-critical scale than any approximation without one of those features. Secondly, this scale decreases even further in the multiloop implementation. In principle it should be possible to obtain vanishing pseudo-critical scales in the scheme with converged parametrization and in the infinite multiloop as well as self-energy iteration limit as the PA obeys this theorem. The numerical verification for the latter is discussed in Ref. [18] in which the inverse AF susceptibility deviates from its linear Curie-Weiss behavior and bends towards a vanishing pseudo-critical scale. This study is currently not feasible in fRG as the number of bosonic patches needed for the correct description of the long-range AF fluctuations increase rapidly for lower temperatures.

Another vividly discussed physical phenomenon is the pseudogap which is observed experimentally in high-T_c superconductors and which could be found with several methods in the 2D Hubbard model with finite next-nearest neighbor hopping t' and doping. While contradicting predictions concerning gap opening obtained through the fRG exist, the presented comparison of the conventional with the SDE-inspired flow revealed the strong influence of the actual vertex parametrization in combination with the self-energy scheme. The discrepancy between the finding of previous implementations could be explained underlining the crucial importance of the new self-energy flow for the prediction of spectral properties. In conclusion, fRG with the proposed SDE self-energy scheme allows for a gap opening even at $t' = 0$ and half-filling while no gap opening was observed in the conventional scheme. This difference was analysed using diagrammatic arguments leading also to the confirmation that long-range AF correlations are indeed the mechanism responsible for the gap opening [106, 101].

The benchmark and qualitative pseudogap study provide the foundation for many possible applications and improvements. The efficient implementation of the multiloop fRG with a smart vertex parametrization and feedback of the self-energy satisfying the SDE can be easily applied to the Hubbard model with finite t' and any doping. While in Section 4.3.2 the benchmark away from half-filling was performed at rather high temperatures, the qualitative physical aspect becomes more exciting in the regime of strong correlations e.g. at lower temperatures. Quantitative predictions become increasingly difficult due to the required parameter resolution of the vertex and multiloop order but the renormalizing nature of this methods allows to study trends and relations between different physical observables. For instance, the influence of the pseudogap opening on the superconducting instability (connecting to Refs. [113, 126, 111, 26]) can be studied. While leaving the rest of the flow scheme unaltered, the pseudogap opening tendency can be suppressed by the use of the conventional self-energy flow equation and allowed by the SDE-inspired one. If the pseudogap has an effect on the superconducting instability, the latter should come out differently depending on which scheme is used.

Further, the fRG implementation can extended to include non-local bare interactions. When the next-nearest neighbor interaction dominates over the local one, charge ordering is expected in the 2D Hubbard model at $t' = 0$ and half-filling. This improved fRG scheme is the perfect tool to complement the FLEX study in Ref. [86] on the competition between the spin and charge instabilities in the intermediate regime or at finite t' and doping.

As the fRG is intrinsically not restricted to geometry or complexity of the systems, it is possible to apply it to all kind of models e.g. the triangular lattice, multi-orbital systems [46, 49] and spin-orbit coupling [21].

In a second step, the implementation can be further optimized or MPI (Message Passing Interface) parallelized. This is in particular important for quantitative results in strongly correlated regimes. For instance, for the proof of the Mermin-Wagner theorem, the solution should be obtained for temperatures approaching zero. However, the spacing between the Matsubara frequencies decreases linearly with the temperature and therefore the window for the low-frequency vertex should include many more frequency points. In addition, the AF-peak becomes stronger and narrower for smaller temperatures. As the exponentially growing AF correlation length is the key ingredient for the verification of the Mermin-Wagner theorem [123], a good resolution of this peak is required. This is only possible by increasing the size of the vertex elements calculated and stored and therefore requires more computational power. Also the improvement from qualitative to quantitative predictions on the exact opening scale of the pseudogap is only possible with further numerical optimizations.

Finally, the combination of different methods allows to access a larger parameter regime, speed up calculations and overcome conceptual and technical difficulties. One promising approach to combine the strength of DMFT and fRG is the so-called DMF^{2}RG [112, 120]. It is recalled that DMFT takes into account only local excitations. In DMF^{2}RG, the DMFT solution is taken as a starting point and fRG is used in order to include non-local excitations. This allows to solve the model even for stronger interactions. While this methods appears to be very similar to the DΓA approach, there is no need for the use of the two-particle irreducible vertex. Therefore, non-physical vertex divergences [102, 100, 94, 124] can be avoided. The modular setup of this code allows for a straightforward adaption for an externally produced initial vertex and the implementation of the DMFT-conserving flow regulator.

In the overall search for a method which can be both accurate and applicable on general model systems, the fRG has become a promising candidate also through the developments developed and shown in this work.

A. Translation of mfRG equations from diagrammatic to physical channels

In the following, the translation of the mfRG equations from the diagrammatic channels $r = \{ph, \overline{ph}, pp\}$ to the physical ones $\eta = \{\mathrm{D}, \mathrm{M}, \mathrm{SC}\}$ is performed. The shifting of frequencies and projection in momentum and form factor space is indicated by the projection operation $\hat{P}_{r\to r'}$ for the translation from channel r to r'. For better readability, the Λ-dependence is omitted in this derivation.

As a starting point, the form-factor projected 1ℓ-equations in the physical channels from Eq. (2.16) are reported

$$\begin{aligned}
\dot{\mathbf{\Phi}}_{ph}(q, i\nu_m, i\nu_{m'}) = \sum_{i\nu_{m''}} \dot{\mathbf{\Pi}}_{ph}(q, i\nu_{m''}) \Big[& 2\mathbf{V}_{ph}(q, i\nu_m, i\nu_{m''})\mathbf{V}_{ph}(q, i\nu_{m''}, i\nu_{m'}) \\
& - \mathbf{V}_{\overline{ph}}(q, i\nu_m, i\nu_{m''})\mathbf{V}_{ph}(q, i\nu_{m''}, i\nu_{m'}) \\
& - \mathbf{V}_{ph}(q, i\nu_m, i\nu_{m''})\mathbf{V}_{\overline{ph}}(q, i\nu_{m''}, i\nu_{m'}) \Big] \qquad \text{(A.1a)} \\
\dot{\mathbf{\Phi}}_{\overline{ph}}(q, i\nu_m, i\nu_{m'}) = - \sum_{i\nu_{m''}} & \mathbf{V}_{\overline{ph}}(q, i\nu_m, i\nu_{m''})\dot{\mathbf{\Pi}}_{ph}(q, i\nu_{m''})\mathbf{V}_{\overline{ph}}(q, i\nu_{m''}, i\nu_{m'}) \qquad \text{(A.1b)} \\
\dot{\mathbf{\Phi}}_{pp}(q, i\nu_m, i\nu_{m'}) = - \sum_{i\nu_{m''}} & \mathbf{V}_{pp}(q, i\nu_m, i\nu_{m''})\dot{\mathbf{\Pi}}_{pp}(q, i\nu_{m''})\mathbf{V}_{pp}(q, i\nu_{m''}, i\nu_{m'}) \; , \qquad \text{(A.1c)}
\end{aligned}$$

where

$$\mathbf{V}_r(q, i\nu_m, i\nu_{m'}) = \mathbf{U} + \mathbf{\Phi}_r(q, i\nu_m, i\nu_{m'}) + \sum_{r'} \hat{P}_{r'\to r}\big[\mathbf{\Phi}_{r'}\big](q, i\nu_m, i\nu_{m'}) \qquad \text{(A.2)}$$

is the full vertex projected to the channel r. $\dot{\mathbf{\Pi}}_r$ denotes the diagrammatic fermionic excitation bubble proportional to $GS + SG$ for pure 1ℓ-fRG defined in Eq. (2.17) or $G\dot{G} + \dot{G}G$ when the Katanin substitution is applied corresponding to the Λ-derivative of Eq. (2.26).

The translation to the physical channels is defined via

$$\begin{aligned}\mathbf{V}_{\mathrm{D}}(q,i\nu_m,i\nu_{m'}) =&\mathbf{V}_{ph,\uparrow\uparrow\uparrow\uparrow}(q,i\nu_m,i\nu_{m'})+\mathbf{V}_{ph,\uparrow\uparrow\downarrow\downarrow}(q,i\nu_m,i\nu_{m'})\\ =&2\mathbf{V}_{ph}(q,i\nu_m,i\nu_{m'})-\mathbf{V}_{\overline{ph}}(q,i\nu_m,i\nu_{m'})\end{aligned}\tag{A.3a}$$

$$\begin{aligned}\mathbf{V}_{\mathrm{M}}(q,i\nu_m,i\nu_{m'}) =&\mathbf{V}_{ph,\uparrow\uparrow\uparrow\uparrow}(q,i\nu_m,i\nu_{m'})-\mathbf{V}_{ph,\uparrow\uparrow\downarrow\downarrow}(q,i\nu_m,i\nu_{m'})\\ =&-\mathbf{V}_{\overline{ph}}(q,i\nu_m,i\nu_{m'})\end{aligned}\tag{A.3b}$$

$$\begin{aligned}\mathbf{V}_{\mathrm{SC}}(q,i\nu_m,i\nu_{m'}) =&\mathbf{V}_{pp,\uparrow\uparrow\downarrow\downarrow}(q,i\nu_m,i\nu_{m'})\\ =&\mathbf{V}_{pp}(q,i\nu_m,i\nu_{m'})\end{aligned}\tag{A.3c}$$

where the SU(2)-spin symmetry was used [94]. In the back transformation

$$\mathbf{V}_{ph}(q,i\nu_m,i\nu_{m'}) =\frac{1}{2}(\mathbf{V}_{\mathrm{D}}(q,i\nu_m,i\nu_{m'})-\mathbf{V}_{\mathrm{M}}(q,i\nu_m,i\nu_{m'}))\tag{A.4a}$$

$$\mathbf{V}_{\overline{ph}}(q,i\nu_m,i\nu_{m'}) =-\mathbf{V}_{\mathrm{M}}(q,i\nu_m,i\nu_{m'})\tag{A.4b}$$

$$\mathbf{V}_{pp}(q,i\nu_m,i\nu_{m'}) =\mathbf{V}_{\mathrm{SC}}(q,i\nu_m,i\nu_{m'})\ ,\tag{A.4c}$$

the spin-dependence was omitted with $\mathbf{V}_r$ denoting the $\uparrow\uparrow\downarrow\downarrow$-contribution of the diagrammatic channel r. The two-particle reducible channels are translated analogously via

$$\boldsymbol{\Phi}_{\mathrm{D}}(q,i\nu_m,i\nu_{m'}) =2\boldsymbol{\Phi}_{ph}(q,i\nu_m,i\nu_{m'})-\boldsymbol{\Phi}_{\overline{ph}}(q,i\nu_m,i\nu_{m'})\tag{A.5a}$$

$$\boldsymbol{\Phi}_{\mathrm{M}}(q,i\nu_m,i\nu_{m'}) =-\boldsymbol{\Phi}_{\overline{ph}}(q,i\nu_m,i\nu_{m'})\tag{A.5b}$$

$$\boldsymbol{\Phi}_{\mathrm{SC}}(q,i\nu_m,i\nu_{m'}) =\boldsymbol{\Phi}_{pp}(q,i\nu_m,i\nu_{m'})\tag{A.5c}$$

and its corresponding back transformation. Substituting Eq. (A.4) in Eq. (A.1) and using this in the scale derivative of Eq. (A.5), the 1ℓ-flow equations in the physical channels are obtained

$$\dot{\boldsymbol{\Phi}}_{\mathrm{D}}(q,i\nu_m,i\nu_{m'})=-\sum_{i\nu_{m''}}\mathbf{V}_{\mathrm{D}}(q,i\nu_m,i\nu_{m''})\dot{\boldsymbol{\Pi}}_{D}(q,i\nu_{m''})\mathbf{V}_{\mathrm{D}}(q,i\nu_{m''},i\nu_{m'})\tag{A.6a}$$

$$\dot{\boldsymbol{\Phi}}_{\mathrm{M}}(q,i\nu_m,i\nu_{m'})=-\sum_{i\nu_{m''}}\mathbf{V}_{\mathrm{M}}(q,i\nu_m,i\nu_{m''})\dot{\boldsymbol{\Pi}}_{M}(q,i\nu_{m''})\mathbf{V}_{\mathrm{M}}(q,i\nu_{m''},i\nu_{m'})\tag{A.6b}$$

$$\dot{\boldsymbol{\Phi}}_{\mathrm{SC}}(q,i\nu_m,i\nu_{m'})=-\sum_{i\nu_{m''}}\mathbf{V}_{\mathrm{SC}}(q,i\nu_m,i\nu_{m''})\dot{\boldsymbol{\Pi}}_{SC}(q,i\nu_{m''})\mathbf{V}_{\mathrm{SC}}(q,i\nu_{m''},i\nu_{m'})\ ,\tag{A.6c}$$

where the bubbles in the physical channels are defined through the ones in the diagrammatic channels according to Eq. (2.19).

In order to obtain the full vertices directly from the two-particle reducible vertices in the channel description without passing through the diagrammatic channels, Eq. (A.2) is first substituted in Eq. (A.3) leading e.g. for the density vertex to Eq. (A.7a). Then the $\boldsymbol{\Phi}_r$ in the diagrammatic channels are replaced with the back transformation of Eq. (A.5) giving

$$
\begin{aligned}
\mathbf{V}_{\mathrm{D}}(q, i\nu_m, i\nu'_m) =& U + 2\mathbf{\Phi}_{ph}(q, i\nu_m, i\nu_{m'}) + 2\hat{P}_{\overline{ph}\to ph}\big[\mathbf{\Phi}_{\overline{ph}}\big](q, i\nu_m, i\nu_{m'}) \\
&+ 2\hat{P}_{pp\to ph}\big[\mathbf{\Phi}_{pp}\big](q, i\nu_m, i\nu_{m'}) - \hat{P}_{ph\to\overline{ph}}\big[\mathbf{\Phi}_{ph}\big](q, i\nu_m, i\nu_{m'}) \\
&- \mathbf{\Phi}_{\overline{ph}}(q, i\nu_m, i\nu_{m'}) - \hat{P}_{pp\to\overline{ph}}\big[\mathbf{\Phi}_{pp}\big](q, i\nu_m, i\nu_{m'}) && \text{(A.7a)} \\
=& U + \mathbf{\Phi}_{\mathrm{D}}(q, i\nu_m, i\nu_{m'}) - \frac{1}{2}\hat{P}_{ph\to\overline{ph}}\big[\mathbf{\Phi}_{\mathrm{D}}\big](q, i\nu_m, i\nu_{m'}) \\
&- 2\hat{P}_{\overline{ph}\to ph}\big[\mathbf{\Phi}_{\mathrm{M}}\big](q, i\nu_m, i\nu_{m'}) + \frac{1}{2}\hat{P}_{ph\to\overline{ph}}\big[\mathbf{\Phi}_{\mathrm{M}}\big](q, i\nu_m, i\nu_{m'}) \\
&+ 2\hat{P}_{pp\to ph}\big[\mathbf{\Phi}_{\mathrm{SC}}\big](q, i\nu_m, i\nu_{m'}) - \hat{P}_{pp\to\overline{ph}}\big[\mathbf{\Phi}_{\mathrm{SC}}\big](q, i\nu_m, i\nu_{m'}) && \text{(A.7b)} \\
\mathbf{V}_{\mathrm{M}}(q, i\nu_m, i\nu_{m'}) =& - U - \frac{1}{2}\hat{P}_{ph\to\overline{ph}}\big[\mathbf{\Phi}_{\mathrm{D}}\big](q, i\nu_m, i\nu_{m'}) + \frac{1}{2}\hat{P}_{ph\to\overline{ph}}\big[\mathbf{\Phi}_{m}\big](q, i\nu_m, i\nu_{m'}) \\
&+ \mathbf{\Phi}_{\mathrm{M}}(q, i\nu_m, i\nu_{m'}) - \hat{P}_{pp\to\overline{ph}}\big[\mathbf{\Phi}_{\mathrm{SC}}\big](q, i\nu_m, i\nu_{m'}) && \text{(A.7c)} \\
\mathbf{V}_{\mathrm{SC}}(q, i\nu_m, i\nu_{m'}) =& U + \frac{1}{2}\hat{P}_{ph\to pp}\big[\mathbf{\Phi}_{\mathrm{D}}\big](q, i\nu_m, i\nu_{m'}) - \frac{1}{2}\hat{P}_{ph\to pp}\big[\mathbf{\Phi}_{\mathrm{M}}\big](q, i\nu_m, i\nu_{m'}) \\
&- \hat{P}_{\overline{ph}\to pp}\big[\mathbf{\Phi}_{\mathrm{M}}\big](q, i\nu_m, i\nu_{m'}) + \mathbf{\Phi}_{\mathrm{SC}}(q, i\nu_m, i\nu_{m'})\ . && \text{(A.7d)}
\end{aligned}
$$

While the flow equations are more compact in the physical channels (compare Eq. (A.1)) than in the diagrammatic channels (compare Eq. (A.5)), the construction of the full vertex requires more projections in the physical channels (compare Eq. (A.7)) than in the diagrammatic channels (compare Eq. (A.2)). These projections are numerically expensive and therefore calculations should only be performed in the physical channels if further reasons exist.

We now turn to the left (L) and right (R) mfRG equations. Note that the 2ℓ-flow equations have the same structure as the latter. Further, we report only the L-mfRG equations as the R-mfRG equations differ only in the position of the two-particle irreducible and the full vertex. The 2ℓ-flow equations in the diagrammatic notation are defined in Eqs. (2.23) and (2.24) and the two-particle irreducible vertex in the physical channels $\mathbf{I}_r$ in Eq. (2.25).

The translation between physical and diagrammatic channels for the vertex and the two-particle reducible vertex is fixed by Eqs. (A.3) to (A.5). We define analogously the translation of the two-particle-irreducible vertex by

$$
\begin{aligned}
\dot{\mathbf{I}}_{\mathrm{D}}(q, i\nu_m, i\nu_{m'}) =& 2\dot{\mathbf{I}}_{ph}(q, i\nu_m, i\nu_{m'}) - \dot{\mathbf{I}}_{\overline{ph}}(q, i\nu_m, i\nu_{m'}) && \text{(A.8a)} \\
\dot{\mathbf{I}}_{\mathrm{M}}(q, i\nu_m, i\nu_{m'}) =& - \dot{\mathbf{I}}_{\overline{ph}}(q, i\nu_m, i\nu_{m'}) && \text{(A.8b)} \\
\dot{\mathbf{I}}_{\mathrm{SC}}(q, i\nu_m, i\nu_{m'}) =& \dot{\mathbf{I}}_{pp}(q, i\nu_m, i\nu_{m'}) && \text{(A.8c)}
\end{aligned}
$$

and its corresponding back transformation. This definition simultaneously satisfies $\dot{\mathbf{I}}_\eta =$

$\dot{\mathbf{V}}_\eta - \dot{\mathbf{\Phi}}_\eta$. The explicit form of the scale-derived two-particle irreducible vertex is

$$\begin{aligned}
\dot{\mathbf{I}}_{\mathrm{D}}(q,i\nu_m,i\nu_{m'}) =& 2\hat{P}_{\overline{ph}\to ph}\big[\dot{\mathbf{\Phi}}_{\overline{ph}}\big](q,i\nu_m,i\nu_{m'}) + 2\hat{P}_{pp\to ph}\big[\dot{\mathbf{\Phi}}_{pp}\big](q,i\nu_m,i\nu_{m'}) \\
&- \hat{P}_{ph\to\overline{ph}}\big[\dot{\mathbf{\Phi}}_{ph}\big](q,i\nu_m,i\nu_{m'}) - \hat{P}_{pp\to\overline{ph}}\big[\dot{\mathbf{\Phi}}_{pp}\big](q,i\nu_m,i\nu_{m'}) \\
=& -2\hat{P}_{\overline{ph}\to ph}\big[\dot{\mathbf{\Phi}}_{\mathrm{M}}\big](q,i\nu_m,i\nu_{m'}) - \frac{1}{2}\hat{P}_{ph\to\overline{ph}}\big[\dot{\mathbf{\Phi}}_{\mathrm{D}}\big](q,i\nu_m,i\nu_{m'}) \\
&+ \frac{1}{2}\hat{P}_{ph\to\overline{ph}}\big[\dot{\mathbf{\Phi}}_{\mathrm{M}}\big](q,i\nu_m,i\nu_{m'}) + 2\hat{P}_{pp\to ph}\big[\dot{\mathbf{\Phi}}_{\mathrm{SC}}\big](q,i\nu_m,i\nu_{m'}) \\
&- \hat{P}_{pp\to\overline{ph}}\big[\dot{\mathbf{\Phi}}_{\mathrm{SC}}\big](q,i\nu_m,i\nu_{m'})
\end{aligned} \tag{A.9a}$$

$$\begin{aligned}
\dot{\mathbf{I}}_{\mathrm{M}}(q,i\nu_m,i\nu_{m'}) =& -\frac{1}{2}\hat{P}_{ph\to\overline{ph}}\big[\dot{\mathbf{\Phi}}_{\mathrm{D}}\big](q,i\nu_m,i\nu_{m'}) + \frac{1}{2}\hat{P}_{ph\to\overline{ph}}\big[\dot{\mathbf{\Phi}}_{\mathrm{M}}\big](q,i\nu_m,i\nu_{m'}) \\
&- \hat{P}_{pp\to\overline{ph}}\big[\dot{\mathbf{\Phi}}_{\mathrm{SC}}\big](q,i\nu_m,i\nu_{m'})
\end{aligned} \tag{A.9b}$$

$$\begin{aligned}
\dot{\mathbf{I}}_{\mathrm{SC}}(q,i\nu_m,i\nu_{m'}) =& \frac{1}{2}\hat{P}_{ph\to pp}\big[\dot{\mathbf{\Phi}}_{\mathrm{D}}\big](q,i\nu_m,i\nu_{m'}) - \frac{1}{2}\hat{P}_{ph\to pp}\big[\dot{\mathbf{\Phi}}_{\mathrm{M}}\big](q,i\nu_m,i\nu_{m'}) \\
&- \hat{P}_{\overline{ph}\to pp}\big[\dot{\mathbf{\Phi}}_{\mathrm{M}}\big](q,i\nu_m,i\nu_{m'})\ .
\end{aligned} \tag{A.9c}$$

The resulting L-mfRG equations assume a compact form

$$\dot{\mathbf{\Phi}}^{\ell,L}_{\mathrm{D}}(q,i\nu_m,i\nu_{m'}) = -\sum_{i\nu_{m''}} \dot{\mathbf{I}}^{\ell-1}_{\mathrm{D}}(q,i\nu_m,i\nu_{m''})\mathbf{\Pi}_{\mathrm{D}}(q,i\nu_{m''})\mathbf{V}_{\mathrm{D}}(q,i\nu_{m''},i\nu_{m'}) \tag{A.10a}$$

$$\dot{\mathbf{\Phi}}^{\ell,L}_{\mathrm{M}}(q,i\nu_m,i\nu_{m'}) = -\sum_{i\nu_{m''}} \dot{\mathbf{I}}^{\ell-1}_{\mathrm{M}}(q,i\nu_m,i\nu_{m''})\mathbf{\Pi}_{\mathrm{M}}(q,i\nu_{m''})\mathbf{V}_{\mathrm{M}}(q,i\nu_{m''},i\nu_{m'}) \tag{A.10b}$$

$$\dot{\mathbf{\Phi}}^{\ell,L}_{\mathrm{SC}}(q,i\nu_m,i\nu_{m'}) = -\sum_{i\nu_{m''}} \dot{\mathbf{I}}^{\ell-1}_{\mathrm{SC}}(q,i\nu_m,i\nu_{m''})\mathbf{\Pi}_{\mathrm{SC}}(q,i\nu_{m''})\mathbf{V}_{\mathrm{SC}}(q,i\nu_{m''},i\nu_{m'})\ . \tag{A.10c}$$

Finally, the central(C)-mfRG equations in the diagrammatic channels are defined according to Eq. (2.30). No further objects have to be introduced and the C-mfRG equations in the physical channels are directly reported

$$\dot{\mathbf{\Phi}}^{\ell,C}_{\mathrm{D}}(q,i\nu_m,i\nu_{m'}) = -\sum_{i\nu_{m''}} \mathbf{V}_{\mathrm{D}}(q,i\nu_m,i\nu_{m''})\mathbf{\Pi}_{\mathrm{D}}(q,i\nu_{m''})\dot{\mathbf{\Phi}}^{\ell-1,L}_{\mathrm{D}}(q,i\nu_{m''},i\nu_{m'}) \tag{A.11a}$$

$$\dot{\mathbf{\Phi}}^{\ell,C}_{\mathrm{M}}(q,i\nu_m,i\nu_{m'}) = -\sum_{i\nu_{m''}} \mathbf{V}_{\mathrm{M}}(q,i\nu_m,i\nu_{m''})\mathbf{\Pi}_{\mathrm{M}}(q,i\nu_{m''})\dot{\mathbf{\Phi}}^{\ell-1,L}_{\mathrm{M}}(q,i\nu_{m''},i\nu_{m'}) \tag{A.11b}$$

$$\dot{\mathbf{\Phi}}^{\ell,C}_{\mathrm{SC}}(q,i\nu_m,i\nu_{m'}) = -\sum_{i\nu_{m''}} \mathbf{V}_{\mathrm{SC}}(q,i\nu_m,i\nu_{m''})\mathbf{\Pi}_{\mathrm{SC}}(q,i\nu_{m''})\dot{\mathbf{\Phi}}^{\ell-1,L}_{\mathrm{SC}}(q,i\nu_{m''},i\nu_{m'})\ . \tag{A.11c}$$

B. Scaling property of the interaction flow at any loop order

In Ref. [42], it is shown that the scale in the interaction flow can be translated to the effective interaction. More specifically, the flow for a bare interaction U at the scale Λ corresponds to the final result of a flow with bare interaction $\Lambda^2 U$. Here, the proof of this property for all loop orders is presented, specifically

$$V^{\Lambda/l}(l^2 U) = l^2 V^{\Lambda}(U) \tag{B.1a}$$

$$\Sigma^{\Lambda/l}(l^2 U) = l \Sigma^{\Lambda}(U)\ , \tag{B.1b}$$

where the superscript indicates the scale within the flow from 0 to 1 and the parameter in the brackets is the bare interaction for which the flow is set up. By setting $l = \Lambda$, it can be followed that a diverging $V^{\Lambda}(U)$ at some $\Lambda < 1$ indicates that the vertex would diverge exactly at $\Lambda = 1$ for a bare interaction $\Lambda^2 U$ which defines the pseudo-critical interaction.

Note that the following discussion simplifies the notation omitting the frequency and momentum dependence, replacing the contractions of dependencies by the symbol $\circ$ and restricting to a schematic description with only one channel (one might consider it to be the particle-particle channel). However, as the scaling properties are not destroyed by the projection to another basis and neither by linear combination of vertices, the other channels analogous. For the same reason the proof holds also for the combination of all channels.

First, it is shown that, for every loop order, an induction procedure can prove the scaling property (B.1) if the condition

$$\dot{V}^{\Lambda/l}(l^2 U) = l^3 \dot{V}^{\Lambda}(U) \tag{B.2a}$$

$$\dot{\Sigma}^{\Lambda/l}(l^2 U) = l^2 \dot{\Sigma}^{\Lambda}(U) \tag{B.2b}$$

is true. It is assumed that the integration over Λ is performed in discrete steps. At each step n, Λ takes the value Λ_n and the vertex is calculated through the equation

$$V^{\Lambda_n}(U) = V^{\Lambda_{n-1}}(U) + (\Lambda_n - \Lambda_{n-1}) \dot{V}^{\Lambda_n}(U)\ . \tag{B.3}$$

The base case for the scaling property of the vertex is

$$V^{\Lambda_0/l}(l^2 U) = l^2 U = l^2 V^{\Lambda_0}(U)\ . \tag{B.4}$$

The induction step

$$\begin{aligned} V^{\Lambda_n/l}(l^2 U) &= V^{\Lambda_{n-1}/l}(l^2 U) + (\frac{\Lambda_n}{l} - \frac{\Lambda_{n-1}}{l}) \dot{V}^{\Lambda_n/l}(l^2 U) \\ &= l^2 V^{\Lambda_{n-1}}(U) + l^2 (\Lambda_n - \Lambda_{n-1}) \dot{V}^{\Lambda_n}(U) \\ &= l^2 V^{\Lambda_n}(U) \end{aligned} \tag{B.5}$$

uses the induction hypothesis (B.1a) and the condition (B.2a).

The procedure for the self-energy is analogous using the equation

$$\Sigma^{\Lambda_n}(U) = \Sigma^{\Lambda_{n-1}}(U) + (\Lambda_n - \Lambda_{n-1})\dot{\Sigma}^{\Lambda_n}(U) \tag{B.6}$$

and the base case

$$\Sigma^{\Lambda_0/l}(l^2U) = 0 = \Sigma^{\Lambda_0}(U)\ . \tag{B.7}$$

Here, the induction hypothesis (B.1b) and the condition (B.2b) are used for the induction step

$$\begin{aligned}\Sigma^{\Lambda_n/l}(l^2U) &= \Sigma^{\Lambda_{n-1}/l}(l^2U) + (\frac{\Lambda_n}{l} - \frac{\Lambda_{n-1}}{l})\dot{\Sigma}^{\Lambda/l}(l^2U)\\ &= l\Sigma^{\Lambda_{n-1}}(U) + l(\Lambda_n - \Lambda_{n-1})\dot{\Sigma}^{\Lambda}(U)\\ &= l\Sigma^{\Lambda_n}(U)\ .\end{aligned} \tag{B.8}$$

For the proof of the condition (B.2) the scaling of the (differentiated) bubbles has to be known. Those involve the Green's function, single-scale propagator and single-scale propagator with Katanin substitution which are defined in the interaction flow as

$$G^{\Lambda}(U) = \Lambda\frac{1}{i\nu_m + \epsilon(k) - \Lambda\Sigma^{\Lambda}(U)} \tag{B.9a}$$

$$S^{\Lambda}(U) = \frac{i\nu_m + \epsilon(k)}{(i\nu_m + \epsilon(k) - \Lambda\Sigma^{\Lambda}(U))^2} \tag{B.9b}$$

$$S_K^{\Lambda}(U) = \frac{i\nu_m + \epsilon(k) + \Lambda^2\dot{\Sigma}^{\Lambda}(U)}{(i\nu_m + \epsilon(k) - \Lambda\Sigma^{\Lambda}(U))^2} \qquad = S^{\Lambda}(U) + G^{\Lambda}(U)\dot{\Sigma}^{\Lambda}(U)G^{\Lambda}(U) \tag{B.9c}$$

and, using the assumption (B.1b) and condition (B.2b) on the scaling of the self-energy, their scaling can be followed easily

$$G^{\Lambda/l}(l^2U) = \frac{\Lambda}{l}\frac{1}{i\nu_m + \epsilon(k) - \frac{\Lambda}{l}\Sigma^{\Lambda/l}(l^2U)} \qquad = \frac{\Lambda}{l}\frac{1}{i\nu_m + \epsilon(k) - \Lambda\Sigma^{\Lambda}(U)} = \frac{1}{l}G^{\Lambda}(U) \tag{B.10a}$$

$$S^{\Lambda/l}(l^2U) = \frac{i\nu_m + \epsilon(k)}{(i\nu_m + \epsilon(k) - \frac{\Lambda}{l}\Sigma^{\Lambda/l}(l^2U))^2} \qquad = \frac{i\nu_m + \epsilon(k)}{(i\nu_m + \epsilon(k) - \Lambda\Sigma^{\Lambda}(U))^2} = S^{\Lambda}(U) \tag{B.10b}$$

$$S_K^{\Lambda/l}(l^2U) = \frac{i\nu_m + \epsilon(k) + (\frac{\Lambda}{l})^2\dot{\Sigma}^{\Lambda/l}(l^2U)}{(i\nu_m + \epsilon(k) - \frac{\Lambda}{l}\Sigma^{\Lambda/l}(l^2U))^2} \qquad = \frac{i\nu_m + \epsilon(k) + \Lambda^2\dot{\Sigma}^{\Lambda}(U)}{(i\nu_m + \epsilon(k) - \Lambda\Sigma^{\Lambda}(U))^2} = S_K^{\Lambda}(U)\ . \tag{B.10c}$$

Note that the single-scale propagator retains the same scaling property after the Katanin substitution and the following proof is performed for both cases simultaneously. With Eq. (B.10), the scaling of the (differentiated) bubbles becomes

$$\Pi^{\Lambda/l}(l^2U) = G^{\Lambda/l}(l^2U)G^{\Lambda/l}(l^2U) \qquad = \frac{1}{l^2}\Pi^{\Lambda}(U) \tag{B.11a}$$

$$\dot{\Pi}^{\Lambda/l}(l^2U) = G^{\Lambda/l}(l^2U)S^{\Lambda/l}(l^2U) + S^{\Lambda/l}(l^2U)G^{\Lambda/l}(l^2U) \qquad = \frac{1}{l}\dot{\Pi}^{\Lambda}(U)\ . \tag{B.11b}$$

In the 1ℓ-approximation, the condition (B.2) is shown easily via

$$\begin{aligned}\dot{V}^{\Lambda_n/l}(l^2U) &= V^{\Lambda_{n-1}/l}(l^2U) \circ \dot{\Pi}^{\Lambda_n/l}(l^2U) \circ V^{\Lambda_{n-1}/l}(l^2U) \\ &= l^3 V^{\Lambda_{n-1}}(U) \circ \dot{\Pi}^{\Lambda_n}(U) \circ V^{\Lambda_{n-1}}(U) = l^3 \dot{V}^{\Lambda_n}(U) \qquad \text{(B.12a)} \\ \dot{\Sigma}^{\Lambda/l}(l^2U) &= S^{\Lambda_n/l}(l^2U) \circ V^{\Lambda_{n-1}/l}(l^2U) = l^2 S^{\Lambda_n} \circ V^{\Lambda_{n-1}}(U) = l^2 \dot{\Sigma}^{\Lambda}(U) \qquad \text{(B.12b)}\end{aligned}$$

which are satisfied both with and without self-energy feedback.

For the $m\ell$-proof, an additional inner induction proof is needed showing that if the equations at one specific Λ_n are true for loop order ℓ, they are also true for loop order $\ell+1$. This involves left, right and central diagrams. It is reminded that the left $m\ell$-correction is

$$\dot{\Phi}^{\Lambda,\ell+2,L}_{\eta} = \dot{I}^{\Lambda,\ell+1}_{\eta} \circ \Pi^{\Lambda}_{\eta} \circ V^{\Lambda}_{\eta} \ , \qquad \text{(B.13)}$$

where $\dot{I}^{\Lambda,\ell}_{\eta} = \sum_{\eta' \neq \eta} \dot{\Phi}^{\Lambda,\ell}_{\eta'}$. The right $m\ell$-correction is related to Eq. (B.13) by an exchange of the position of $\dot{I}$ and γ_4 which does not change the structure and hence the scaling property.

The central $m\ell$-correction is

$$\dot{\Phi}^{\Lambda,\ell+2,C}_{\eta} = V^{\Lambda}_{\eta} \circ \Pi^{\Lambda}_{\eta} \circ \dot{I}^{\Lambda,\ell}_{\eta} \circ \Pi^{\Lambda}_{\eta} \circ V^{\Lambda}_{\eta} \ . \qquad \text{(B.14)}$$

The left, right and central contributions are added to the 1ℓ vertex flow, which has been considered above and shown to satisfy the scaling property. The following proof assumes that the induction is performed flow step after flow step and, within each step, loop order after loop order. Then, the central equation for the induction proof is

$$\begin{aligned}\dot{V}^{\Lambda_n,\ell}(U) = &\dot{I}^{\Lambda_n,\ell-1}(U) \circ \Pi^{\Lambda_n}(U) \circ V^{\Lambda_{n-1}}(U) + V^{\Lambda_{n-1}}(U) \circ \Pi^{\Lambda_n}(U) \circ \dot{I}^{\Lambda_n,\ell-1}(U) \\ &+ V^{\Lambda_{n-1}}(U) \circ \Pi^{\Lambda_n}(U) \circ \dot{I}^{\Lambda_n,\ell-2}(U) \circ \Pi^{\Lambda_n}(U) \circ V^{\Lambda_{n-1}}(U) \ , \qquad \text{(B.15)}\end{aligned}$$

omitting the channel index η. While for $\Lambda_n = \Lambda_0$, all loop orders vanish trivially

$$\dot{V}^{\Lambda_0/l,\ell}(l^2U) = 0 = \dot{V}^{\Lambda_0,\ell}(U) \ , \qquad \text{(B.16)}$$

for Λ_1 is treated analogously as any flow step Λ_n shown in the following. There, two base cases have to be considered as the multiloop correction according to Eq. (B.15) depends both on $\ell-1$ and $\ell-2$. The first is actually the $\ell = 1$ contribution (B.12a) and the second the $\ell = 2$ contribution

$$\begin{aligned}\dot{V}^{\Lambda_n/l,2}(l^2U) = &\underbrace{V^{\Lambda_{n-1}/l}(l^2U) \circ \dot{\Pi}^{\Lambda_n/l}(l^2U) \circ V^{\Lambda_{n-1}/l}(l^2U)}_{\dot{I}^{\Lambda_n/l,1}(l^2U)} \circ \Pi^{\Lambda_n/l}(l^2U) \circ V^{\Lambda_{n-1}/l}(l^2U) \\ &+ (\text{right} \sim \text{left}) + (\text{central} = 0\ ) \\ &= l^3 V^{\Lambda_{n-1}}(U) \circ \dot{\Pi}^{\Lambda_n}(U) \circ V^{\Lambda_{n-1}}(U) \circ \Pi^{\Lambda_n}(U) \circ V^{\Lambda_{n-1}}(U) \\ &= l^3 \dot{V}^{\Lambda_n,2}(U) \ . \qquad \text{(B.17)}\end{aligned}$$

At step n, the here used condition (B.2a) for $V^{\Lambda_{n-1}/l}(l^2U)$ at the previous step $n-1$ is already fulfilled if the induction proof for each Λ_n is performed in increasing order of n. Furthermore, at step n and loop order ℓ, the condition (B.2a) was already proven for all smaller loop orders at step n and therefore

$$\dot{I}^{\Lambda_n/l,\ell-1}(l^2U) = l^3 \dot{I}^{\Lambda_n,\ell-1}(U) \dot{I}^{\Lambda_n/l,\ell-2}(l^2U) \qquad = l^3 \dot{I}^{\Lambda_n,\ell-2}(U) \qquad \text{(B.18a)}$$

can be used in the induction step

$$\begin{aligned}\dot{V}^{\Lambda_n/l,\ell}(l^2U) =& \dot{I}^{\Lambda_n/l,\ell-1}(l^2U) \circ \Pi^{\Lambda_n/l}(l^2U) \circ V^{\Lambda_{n-1}/l}(l^2U) + (\text{right} \sim \text{left}) \\ &+V^{\Lambda_{n-1}/l}(l^2U) \circ \Pi^{\Lambda_n/l}(l^2U) \circ \dot{I}^{\Lambda_n/l,\ell-2}(l^2U) \circ \Pi^{\Lambda_n/l}(l^2U) \circ V^{\Lambda_{n-1}/l}(l^2U) \\ &= l^3\dot{I}^{\Lambda_n,\ell-1}(U) \circ \Pi^{\Lambda_n}(U) \circ V^{\Lambda_{n-1}}(U) + (\text{right} \sim \text{left}) \\ &+l^3V^{\Lambda_{n-1}}(U) \circ \Pi^{\Lambda_n}(U) \circ \dot{I}^{\Lambda_n,\ell-2}(U) \circ \Pi^{\Lambda_n}(U) \circ V^{\Lambda_{n-1}}(U) \\ &= l^3\dot{V}^{\Lambda_n,\ell}(U)\;,\end{aligned} \tag{B.19}$$

which proves the scaling property of the vertex flow.

Next, the two multiloop corrections of the self-energy are considered. For this, only Eq. (B.2b) has to be shown in order to repeat the induction as outlined in Eq. (B.8) and prove the scaling property. The first multiloop correction is

$$\dot{\Sigma}^{\Lambda_n,1}(U) = -G^{\Lambda_n}(U) \circ \Big[2\dot{I}^{\Lambda_n,C}(U) - \dot{I}^{\Lambda_n,C}(U)\Big] \tag{B.20}$$

for which it can be shown that the condition of the scale property is satisfied

$$\begin{aligned}\dot{\Sigma}^{\Lambda_n/l,1}(l^2U) &= -G^{\Lambda_n/l}(l^2U) \circ \Big[2\dot{I}^{\Lambda_n/l,C}(l^2U) - \dot{I}^{\Lambda_n/l,C}(l^2U)\Big] \\ &= -\frac{1}{l}G^{\Lambda_n}(U) \circ \Big[2l^3\dot{I}^{\Lambda_n,C}(U) - l^3\dot{I}^{\Lambda_n,C}(U)\Big] \\ &= l^2\dot{\Sigma}^{\Lambda_n,C}(U)\,.\end{aligned} \tag{B.21}$$

Finally, the second correction reads

$$\dot{\Sigma}^{\Lambda_n,2}(U) = -\delta S^{\Lambda_n}(U)\Big[2V^{\Lambda_n}(U) - V^{\Lambda_n}(U)\Big] \tag{B.22}$$

where $\delta S^{\Lambda_n}(U) = G^{\Lambda_n}(U)\dot{\Sigma}^{\Lambda_n,1}(U)G^{\Lambda_n}(U)$ which satisfies

$$\delta S^{\Lambda_n/l}(l^2U) = \delta S^{\Lambda_n}(U)\,. \tag{B.23}$$

$$\tag{B.24}$$

This is used in

$$\begin{aligned}\dot{\Sigma}^{\Lambda_n/l,2}(l^2U) &= -\delta S^{\Lambda_n/l}(l^2U) \circ \Big[2V^{\Lambda_n/l}(l^2U) - V^{\Lambda_n/l}(l^2U)\Big] \\ &= -\delta S^{\Lambda_n}(U) \circ \Big[2l^2V^{\Lambda_n}(U) - l^2V^{\Lambda_n}(U)\Big] \\ &= l^2\dot{\Sigma}^{\Lambda_n,2}(U)\,,\end{aligned} \tag{B.25}$$

which finalized the proof of the scaling property (B.1) in multiloop fRG.

In addition to this analytical study, it was also verified numerically that the scaling property is satisfied at any loop order.

C. Personal contribution to publications

C.1 Multiloop functional renormalization group for the two-dimensional Hubbard model: Loop convergence of the response functions

[A. Tagliavini, C. Hille, F. B. Kugler, S. Andergassen, A. Toschi, and C. Honerkamp. "Multiloop functional renormalization group for the two-dimensional Hubbard model: Loop convergence of the response functions". In: *SciPost Physics* 6 (2019), p. 009. DOI: `10.21468/SciPostPhys.6.1.009`]

The work related to this publication sets the basis for future material and system related calculations as well as method development. The collaboration between A. Tagliavini and myself was very close. All parts of the coding and derivation were understood and double checked by both first authors. Especially for the coding and debugging part we adopted the pair programming technique in order to minimize errors and increase the readability of the code. Nevertheless, one can attribute main fields of activities. While A. Tagliavini pushed our work regarding the susceptibilities and multiloop fRG implementation, I focussed on technical questions regarding the extension of the code to non-local systems, including debugging, optimization and attempts of parallelization. In this publication, A. Tagliavini and me share first authorship. My contribution to the manuscript consists in Sections 3.1., 4.2., 4.3, 4.4. and Appendices A, F and G.

C.2 Quantitative functional renormalization-group description of the two-dimensional Hubbard model

[C. Hille, F. B. Kugler, C. J. Eckhardt, Y.-Y. He, A. Kauch, C. Honerkamp, A. Toschi, and S. Andergassen. "Quantitative functional renormalization-group description of the two-dimensional Hubbard model". In: *pre-print* (2020). arXiv: `2002.02733`]

In this publication, the benchmark to other methods is performed. I developed the new flow scheme for the self-energy and implemented it in the code already developed in the framework of Ref. [110]. Also the post-processing of the self-energy was added by myself. The idea on how to explain the difference of the self-energy flow schemes was preformed in discussions with A. Tagliavini, C. Eckhardt and myself. The presentation thereof in the paper was proposed by myself and improved through extensive input from F. B. Kugler.

I performed all fRG calculations, collected the results from the other methods, fitted the correlation length for all methods and created all plots. My contribution to the manuscript consists in Sections II, III, V, VI and Appendix A to C. I also contributed in the shaping of Section II.B. The paper was submitted to *Physical Review Research* on the 10th of February 2020.

C.3 Pseudogap opening in the two-dimensional Hubbard model: a functional renormalization group analysis

[C. Hille, D. Rohe, C. Honerkamp, and S. Andergassen. “Pseudogap opening in the two-dimensional Hubbard model: A functional renormalization group analysis”. In: *Phys. Rev. Research* 2 (2020), p. 033068. DOI: `10.1103/PhysRevResearch.2.033068`]

This publication applies the new flow scheme for the self-energy in order to study the pseudogap opening in the half-filled 2D-Hubbard model. While the original idea to study the gap opening with our code came from D. Rohe, I suggested to use the new flow scheme which finally led to the interesting results shown. In this paper, I produced all data and figures by myself. I developed the idea to compare the first orders of $\overline{ph}$-diagrams and implemented those. My contribution to the manuscript consists in a first version of Section I, i Sections II and III and in Appendix A and B. The paper was submitted to *Physical Review Research* on the 4th of March 2020.

Bibliography

[1] A. Abanov, A. V. Chubukov, and J. Schmalian. “Quantum-critical theory of the spin-fermion model and its application to cuprates: Normal state analysis”. In: *Adv. Phys.* 52 (2003), p. 119. DOI: `10.1080/0001873021000057123`.

[2] S. Andergassen, T. Enss, V. Meden, W. Metzner, U. Schollwöck, and K. Schönhammer. “Functional renormalization group for Luttinger liquids with impurities”. In: *Phys. Rev. B* 70 (2004), p. 075102. DOI: `10.1103/PhysRevB.70.075102`.

[3] S. Andergassen, T. Enss, V. Meden, W. Metzner, U. Schollwöck, and K. Schönhammer. “Renormalization-group analysis of the one-dimensional extended Hubbard model with a single impurity”. In: *Phys. Rev. B* 73 (2006), p. 045125. DOI: `10.1103/PhysRevB.73.045125`.

[4] P. W. Anderson. “A poor man’s derivation of scaling laws for the Kondo problem”. In: *Journal of Physics C: Solid State Physics* 3 (1970), p. 2436. DOI: `10.1088/0022-3719/3/12/008`.

[5] F. Aryasetiawan, M. Imada, A. Georges, G. Kotliar, S. Biermann, and A. I. Lichtenstein. “Frequency-dependent local interactions and low-energy effective models from electronic structure calculations”. In: *Phys. Rev. B* 70 (2004), p. 195104. DOI: `10.1103/PhysRevB.70.195104`.

[6] J. G. Bednorz and K. A. Müller. “Possible high T_c superconductivity in the Ba-La-Cu-O system”. In: *Zeitschrift für Physik B Condensed Matter* 64 (1986), p. 189. DOI: `10.1007/BF01303701`.

[7] J. Berges, N. Tetradis, and C. Wetterich. “Non-perturbative renormalization flow in quantum field theory and statistical physics”. In: *Physics Reports* 363 (2002), p. 223. DOI: `10.1016/S0370-1573(01)00098-9`.

[8] N. E. Bickers. “Parquet equations for numerical self-consistent-field theory”. In: *Int. J. Mod. Phys. B* 05 (1991), p. 253. DOI: `10.1142/s021797929100016x`.

[9] N. E. Bickers. “Self-Consistent Many-Body Theory for Condensed Matter Systems”. In: *Theoretical Methods for Strongly Correlated Electrons*. Ed. by B. C. Sénéchal D. Tremblay A.-M. S. Springer New York, 2004, pp. 237–296. DOI: `10.1007/0-387-21717-7_6`.

[10] N. E. Bickers and D. J. Scalapino. “Conserving approximations for strongly fluctuating electron systems. I. Formalism and calculational approach”. In: *Ann. Phys.* 193 (1989), p. 206. DOI: `10.1016/0003-4916(89)90359-X`.

[11] R. Blankenbecler, D. J. Scalapino, and R. L. Sugar. “Monte Carlo calculations of coupled boson-fermion systems. I”. In: *Phys. Rev. D* 24 (1981), p. 2278. DOI: `10.1103/PhysRevD.24.2278`.

[12] P. Chalupa, C. Hille, F. B. Kugler, J. von Delft, S. Andergassen, and A. Toschi. In: *in preparation* (2020).

[13] E. Dagotto. "Correlated electrons in high-temperature superconductors". In: *Rev. Mod. Phys.* 66 (1994), p. 763. DOI: `10.1103/RevModPhys.66.763`.

[14] A. Damascelli, Z. Hussain, and Z.-X. Shen. "Angle-resolved photoemission studies of the cuprate superconductors". In: *Rev. Mod. Phys.* 75 (2003), p. 473. DOI: `10.1103/RevModPhys.75.473`.

[15] A. Eberlein. "Fermionic two-loop functional renormalization group for correlated fermions: Method and application to the attractive Hubbard model". In: *Phys. Rev. B* 90 (2014), p. 115125. DOI: `10.1103/PhysRevB.90.115125`.

[16] A. Eberlein. "Self-energy effects in functional renormalization group flows of the two-dimensional $t{-}t'$ Hubbard model away from van Hove filling". In: *Phys. Rev. B* 92 (2015), p. 235146. DOI: `10.1103/PhysRevB.92.235146`.

[17] C. J. Eckhardt, G. A. H. Schober, J. Ehrlich, and C. Honerkamp. "Truncated-unity parquet equations: Application to the repulsive Hubbard model". In: *Phys. Rev. B* 98 (2018), p. 075143. DOI: `10.1103/PhysRevB.98.075143`.

[18] C. J. Eckhardt, C. Honerkamp, K. Held, and A. Kauch. "Truncated unity parquet solver". In: *Phys. Rev. B* 101 (2020), p. 155104. DOI: `10.1103/physrevb.101.155104`.

[19] Y. Fang, G. Grissonnanche, A. Legros, S. Verret, F. Laliberte, C. Collignon, A. Ataei, M. Dion, J. Zhou, D. Graf, M. J. Lawler, P. Goddard, L. Taillefer, and B. J. Ramshaw. "Fermi surface transformation at the pseudogap critical point of a cuprate superconductor". In: *pre-print* (2020). arXiv: `2004.01725`.

[20] L. F. Feiner, J. H. Jefferson, and R. Raimondi. "Effective single-band models for the high-T_c cuprates. I. Coulomb interactions". In: *Phys. Rev. B* 53.13 (1996), p. 8751. DOI: `10.1103/PhysRevB.53.8751`.

[21] T. R. G. A. H. Schober J. Ehrlich and C. Honerkamp. "Truncated-unity functional renormalization group for multiband systems with spin-orbit coupling". In: *Frontiers in Physics* 6 (2018), p. 1.

[22] A. Georges and G. Kotliar. "Hubbard model in infinite dimensions". In: *Phys. Rev. B* 45 (1992), p. 6479. DOI: `10.1103/PhysRevB.45.6479`.

[23] A. Georges, G. Kotliar, W. Krauth, and M. J. Rozenberg. "Dynamical mean-field theory of strongly correlated fermion systems and the limit of infinite dimensions". In: *Rev. Mod. Phys.* 68 (1996), p. 13. DOI: `10.1103/RevModPhys.68.13`.

[24] K.-U. Giering and M. Salmhofer. "Self-energy flows in the two-dimensional repulsive Hubbard model". In: *Phys. Rev. B* 86 (2012), p. 245122. DOI: `10.1103/PhysRevB.86.245122`.

[25] E. Gull and A. J. Millis. "Energetics of superconductivity in the two-dimensional Hubbard model". In: *Phys. Rev. B* 86 (2012), p. 1. DOI: `10.1103/PhysRevB.86.241106`.

[26] E. Gull, O. Parcollet, and A. J. Millis. "Superconductivity and the pseudogap in the two-dimensional hubbard model". In: *Phys. Rev. Lett.* 110 (2013), p. 216405. DOI: `10.1103/PhysRevLett.110.216405`.

[27] E. Gull, O. Parcollet, P. Werner, and A. J. Millis. “Momentum-sector-selective metal-insulator transition in the eight-site dynamical mean-field approximation to the Hubbard model in two dimensions”. In: *Phys. Rev. B* 80 (2009), p. 1. DOI: `10.1103/PhysRevB.80.245102`.

[28] O. Gunnarsson, T. Schäfer, J. P. F. LeBlanc, J. Merino, G. Sangiovanni, G. Rohringer, and A. Toschi. “Parquet decomposition calculations of the electronic self-energy”. In: *Phys. Rev. B* 93 (2016), p. 245102. DOI: `10.1103/PhysRevB.93.245102`.

[29] O. Gunnarsson, T. Schäfer, J. P. F. LeBlanc, E. Gull, J. Merino, G. Sangiovanni, G. Rohringer, and A. Toschi. “Fluctuation Diagnostics of the Electron Self-Energy: Origin of the Pseudogap Physics”. In: *Phys. Rev. Lett.* 114.23 (2015), p. 236402. DOI: `10.1103/PhysRevLett.114.236402`.

[30] C. J. Halboth and W. Metzner. “d-Wave Superconductivity and Pomeranchuk Instability in the Two-Dimensional Hubbard Model”. In: *Phys. Rev. Lett.* 85 (2000), p. 5162. DOI: `10.1103/PhysRevLett.85.5162`.

[31] C. J. Halboth and W. Metzner. “Renormalization-group analysis of the two-dimensional Hubbard model”. In: *Phys. Rev. B* 61 (2000), p. 7364. DOI: `10.1103/PhysRevB.61.7364`.

[32] V. Hankevych, B. Kyung, A. M. Daré, D. Sénéchal, and A.-M. S. Tremblay. “Strong- and weak-coupling mechanisms for pseudogap in electron-doped cuprates”. In: *J. Phys. Chem. Solids* 67 (2006), p. 189. DOI: `10.1016/j.jpcs.2005.10.121`.

[33] P. Hansmann, N. Parragh, A. Toschi, G. Sangiovanni, and K. Held. “Importance of $d-p$ Coulomb interaction for high T_c cuprates and other oxides”. In: *New J. Phys.* 16 (2014), p. 033009. DOI: `10.1088/1367-2630/16/3/033009`.

[34] Y.-Y. He, M. Qin, H. Shi, Z.-Y. Lu, and S. Zhang. “Finite-temperature auxiliary-field quantum Monte Carlo: Self-consistent constraint and systematic approach to low temperatures”. In: *Phys. Rev. B* 99 (2019), p. 045108. DOI: `10.1103/PhysRevB.99.045108`.

[35] Y.-Y. He, H. Shi, and S. Zhang. “Reaching the Continuum Limit in Finite-Temperature Ab Initio Field-Theory Computations in Many-Fermion Systems”. In: *Phys. Rev. Lett.* 123 (2019), p. 136402. DOI: `10.1103/PhysRevLett.123.136402`.

[36] K. Held, A. A. Katanin, and A. Toschi. “Dynamical Vertex Approximation: An Introduction”. In: *Prog. Theor. Phys. Supp.* 176 (2008), p. 117. DOI: `10.1143/PTPS.176.117`.

[37] M. H. Hettler, A. N. Tahvildar-Zadeh, M. Jarrell, T. Pruschke, and H. R. Krishnamurthy. “Nonlocal dynamical correlations of strongly interacting electron systems”. In: *Phys. Rev. B* 58 (1998), R7475. DOI: `10.1103/PhysRevB.58.R7475`.

[38] C. Hille, F. B. Kugler, C. J. Eckhardt, Y.-Y. He, A. Kauch, C. Honerkamp, A. Toschi, and S. Andergassen. “Quantitative functional renormalization-group description of the two-dimensional Hubbard model”. In: *pre-print* (2020). arXiv: `2002.02733`.

[39] C. Hille, D. Rohe, C. Honerkamp, and S. Andergassen. “Pseudogap opening in the two-dimensional Hubbard model: A functional renormalization group analysis”. In: *Phys. Rev. Research* 2 (2020), p. 033068. DOI: `10.1103/PhysRevResearch.2.033068`.

[40] J. E. Hoffman, K. McElroy, D.-H. Lee, K. M. Lang, H. Eisaki, S. Uchida, and J. C. Davis. “Imaging Quasiparticle Interference in Bi2Sr2CaCu2O8+δ”. In: *Science* 297 (2002), p. 1148. DOI: `10.1126/science.1072640`.

[41] C. Honerkamp. “Electron-doping versus hole-doping in the 2D t-t’ Hubbard model”. In: *Eur. Phys. J. B* 21 (2001), p. 81. DOI: `10.1007/PL00011117`.

[42] C. Honerkamp, D. Rohe, S. Andergassen, and T. Enss. “Interaction flow method for many-fermion systems”. In: *Phys. Rev. B* 70 (2004), p. 235115. DOI: `10.1103/PhysRevB.70.235115`.

[43] C. Honerkamp, M. Salmhofer, N. Furukawa, and T. M. Rice. “Breakdown of the Landau-Fermi liquid in two dimensions due to umklapp scattering”. In: *Phys. Rev. B* 63 (2001), p. 035109. DOI: `10.1103/PhysRevB.63.035109`.

[44] C. Honerkamp. “Density Waves and Cooper Pairing on the Honeycomb Lattice”. In: *Phys. Rev. Lett.* 100 (2008), p. 146404. DOI: `10.1103/PhysRevLett.100.146404`.

[45] C. Honerkamp. “Effective interactions in multiband systems from constrained summations”. In: *Phys. Rev. B* 85 (2012), p. 195129. DOI: `10.1103/PhysRevB.85.195129`.

[46] C. Honerkamp. “Efficient vertex parametrization for the constrained functional renormalization group for effective low-energy interactions in multiband systems”. In: *Phys. Rev. B* 98 (2018), p. 155132. DOI: `10.1103/PhysRevB.98.155132`.

[47] C. Honerkamp and M. Salmhofer. “Flow of the quasiparticle weight in the N-patch renormalization group scheme”. In: *Phys. Rev. B* 67 (2003), p. 174504. DOI: `10.1103/PhysRevB.67.174504`.

[48] C. Honerkamp and M. Salmhofer. “Temperature-flow renormalization group and the competition between superconductivity and ferromagnetism”. In: *Phys. Rev. B* 64 (2001), p. 184516. DOI: `10.1103/PhysRevB.64.184516`.

[49] C. Honerkamp, H. Shinaoka, F. F. Assaad, and Werner. “Limitations of constrained random phase approximation downfolding”. In: *Phys. Rev. B* 98 (2018), p. 235151.

[50] J. Hubbard. “Electron correlations in narrow energy bands”. In: *Proc. Roy. Soc. London Ser. A* 276 (1963), p. 238. DOI: `10.1098/rspa.1963.0204`.

[51] C. Huscroft, M. Jarrell, T. Maier, S. Moukouri, and A. N. Tahvildarzadeh. “Pseudogaps in the 2D Hubbard model”. In: *Phy. Rev. Lett.* 86 (2001), p. 139. DOI: `10.1103/PhysRevLett.86.139`.

[52] C. Husemann, K.-U. Giering, and M. Salmhofer. “Frequency-dependent vertex functions of the $(t, t^{'})$ Hubbard model at weak coupling”. In: *Phys. Rev. B* 85 (2012), p. 075121. DOI: `10.1103/PhysRevB.85.075121`.

[53] C. Husemann and M. Salmhofer. “Efficient parametrization of the vertex function, Ω scheme, and the $t, t^{'}$ Hubbard model at van Hove filling”. In: *Phys. Rev. B* 79 (2009), p. 195125. DOI: `10.1103/PhysRevB.79.195125`.

[54] C. Karrasch. “The Functional Renormalization Group for Zero-Dimensional Quantum Systems in and out of Equilibrium”. PhD thesis. RWTH Aachen University, 2010.

[55] C. Karrasch, R. Hedden, R. Peters, T. Pruschke, K. Schönhammer, and V. Meden. "A finite-frequency functional renormalization group approach to the single impurity Anderson model". In: *J. Phys.: Condens. Matter* 20 (2008), p. 345205. DOI: `10.1088/0953-8984/20/34/345205`.

[56] A. A. Katanin. "Fulfillment of Ward identities in the functional renormalization group approach". In: *Phys. Rev. B* 70 (2004), p. 115109. DOI: `10.1103/PhysRevB.70.115109`.

[57] A. A. Katanin. "Two-loop functional renormalization group approach to the one- and two-dimensional Hubbard model". In: *Phys. Rev. B* 79 (2009), p. 235119. DOI: `10.1103/PhysRevB.79.235119`.

[58] A. A. Katanin and A. P. Kampf. "Quasiparticle Anisotropy and Pseudogap Formation from the Weak-Coupling Renormalization Group Point of View". In: *Phys. Rev. Lett.* 93 (2004), p. 106406. DOI: `10.1103/PhysRevLett.93.106406`.

[59] M. L. Kiesel, C. Platt, W. Hanke, D. A. Abanin, and R. Thomale. "Competing many-body instabilities and unconventional superconductivity in graphene". In: *Phys. Rev. B* 86 (2012), p. 020507. DOI: `10.1103/PhysRevB.86.020507`.

[60] A. J. Kim, F. Simkovic, and E. Kozik. "Spin and Charge Correlations across the Metal-to-Insulator Crossover in the Half-Filled 2D Hubbard Model". In: *Phys. Rev. Lett.* 124 (2020), p. 117602. DOI: `10.1103/PhysRevLett.124.117602`.

[61] M. Kinza. "Single Impurity Anderson Model and Dynamical Mean Field Theory A Functional Renormalization Group Study". PhD thesis. RWTH Aachen University, 2013.

[62] M. Klett, N. Wentzell, T. Schäfer, F. Simkovic IV, O. Parcollet, S. Andergassen, and P. Hansmann. "Real-space cluster dynamical mean-field theory: Center focused extrapolation on the one- and two particle level". In: *pre-print* (2020). arXiv: `2003.05215`.

[63] W. Kohn. "Nobel Lecture: Electronic structure of matter—wave functions and density functionals". In: *Rev. Mod. Phys.* 71 (1999), p. 1253. DOI: `10.1103/RevModPhys.71.1253`.

[64] P. Kopietz, L. Bartosch, and F. Schütz. *Introduction to the Functional Renormalization Group*. Springer Berlin, 2010. DOI: `10.1007/978-3-642-05094-7`.

[65] G. Kotliar, S. Y. Savrasov, G. Pálsson, and G. Biroli. "Cellular Dynamical Mean Field Approach to Strongly Correlated Systems". In: *Phys. Rev. Lett.* 87 (2001), p. 186401. DOI: `10.1103/PhysRevLett.87.186401`.

[66] F. B. Kugler and J. von Delft. "Fermi-edge singularity and the functional renormalization group". In: *Journal of Physics: Condensed Matter* 30 (2018), p. 195501. DOI: `10.1088/1361-648x/aaba2e`.

[67] F. B. Kugler and J. von Delft. "Multiloop Functional Renormalization Group That Sums Up All Parquet Diagrams". In: *Phys. Rev. Lett.* 120 (2018), p. 057403. DOI: `10.1103/PhysRevLett.120.057403`.

[68] F. B. Kugler and J. von Delft. "Derivation of exact flow equations from the self-consistent parquet relations". In: *New J. Phys.* 20 (2018), p. 123029. DOI: `10.1088/1367-2630/aaf65f`.

[69] F. B. Kugler and J. von Delft. “Multi-loop functional renormalization group for general models”. In: *Phys. Rev. B* 97 (2018), p. 035162. DOI: `10.1103/PhysRevB.97.035162`.

[70] B. Kyung, V. Hankevych, A. M. Daré, and A.-M. S. Tremblay. “Pseudogap and spin fluctuations in the normal state of the electron-doped cuprates”. In: *Phys. Rev. Lett.* 93 (2004), p. 1. DOI: `10.1103/PhysRevLett.93.147004`.

[71] B. Kyung, S. S. Kancharla, D. Sénéchal, A.-M. S. Tremblay, M. Civelli, and G. Kotliar. “Pseudogap induced by short-range spin correlations in a doped Mott insulator”. In: *Phys. Rev. B* 73 (2006), p. 1. DOI: `10.1103/PhysRevB.73.165114`.

[72] B. Kyung, J. S. Landry, D. Poulin, and A.-M. S. Tremblay. “Comment on “Absence of a Slater Transition in the Two-Dimensional Hubbard Model”. In: *Phys. Rev. Lett.* 90 (2003), p. 99702. DOI: `10.1103/PhysRevLett.90.099702`.

[73] F. Lemay. “Des propriétés de l’état normal du modèle de Hubbard bidimensionnel”. PhD thesis. Université de Sherbrooke, 2000.

[74] G. Li, A. Kauch, P. Pudleiner, and K. Held. “The victory project v1.0: An efficient parquet equations solver”. In: *Computer Physics Communications* 241 (2019), pp. 146–154. DOI: `10.1016/j.cpc.2019.03.008`.

[75] G. Li, N. Wentzell, P. Pudleiner, P. Thunström, and K. Held. “Efficient implementation of the parquet equations: Role of the reducible vertex function and its kernel approximation”. In: *Phys. Rev. B* 93 (2016), p. 165103. DOI: `10.1103/PhysRevB.93.165103`.

[76] J. Lichtenstein, S. Sanchez de la Peña, D. Rohe, E. Di Napoli, C. Honerkamp, and S. Maier. “High-performance functional Renormalization Group calculations for interacting fermions”. In: *Comput. Phys. Commun.* 213 (2017), p. 100. DOI: `10.1016/j.cpc.2016.12.013`.

[77] A. Macridin, M. Jarrell, T. Maier, P. R. C. Kent, and E. D’Azevedo. “Pseudogap and antiferromagnetic correlations in the hubbard model”. In: *Phys. Rev. Lett.* 97 (2006), p. 1. DOI: `10.1103/PhysRevLett.97.036401`.

[78] G. D. Mahan. *Many-Particle Physics.* Springer US, 2000. DOI: `10.1007/978-1-4757-5714-9`.

[79] S. Maier, J. Ortloff, and C. Honerkamp. “Multiorbital effects in the functional renormalization group: A weak-coupling study of the Emery model”. In: *Phys. Rev. B* 88 (2013), p. 1. DOI: `10.1103/PhysRevB.88.235112`.

[80] P. Mehta and D. J. Schwab. “An exact mapping between the Variational Renormalization Group and Deep Learning”. In: *pre-print* (2014). arXiv: `1410.3831`.

[81] N. D. Mermin and H. Wagner. “Absence of Ferromagnetism or Antiferromagnetism in One- or Two-Dimensional Isotropic Heisenberg Models”. In: *Phys. Rev. Lett.* 17 (1966), p. 1133. DOI: `10.1103/PhysRevLett.17.1133`.

[82] W. Metzner, M. Salmhofer, C. Honerkamp, V. Meden, and K. Schönhammer. “Functional renormalization group approach to correlated fermion systems”. In: *Rev. Mod. Phys.* 84 (2012), p. 299. DOI: `10.1103/RevModPhys.84.299`.

[83] W. Metzner and D. Vollhardt. “Correlated Lattice Fermions in $d = \infty$ Dimensions”. In: *Phys. Rev. Lett.* 62 (1989), p. 324. DOI: `10.1103/PhysRevLett.62.324`.

[84] X. Montiel, T. Kloss, and C. Pépin. “Effective SU(2) theory for the pseudogap state”. In: *Phys. Rev. B* 95 (2017), p. 104510. DOI: `10.1103/PhysRevB.95.104510`.

[85] P. Nozières. “The theory of interacting Fermi systems”. In: (1964). DOI: `10.1016/0029-5582(64)90379-7`.

[86] S. Onari, R. Arita, K. Kuroki, and H. Aoki. “Phase diagram of the two-dimensional extended Hubbard model: Phase transitions between different pairing symmetries when charge and spin fluctuations coexist”. In: *Phys. Rev. B* 70 (2004), p. 094523. DOI: `10.1103/PhysRevB.70.094523`.

[87] D. S. de la Peña, J. Lichtenstein, and C. Honerkamp. “Competing electronic instabilities of extended Hubbard models on the honeycomb lattice: A functional renormalization group calculation with high-wave-vector resolution”. In: *Phys. Rev. B* 95 (2017), p. 085143. DOI: `10.1103/PhysRevB.95.085143`.

[88] M. Potthoff. “Self-energy-functional approach: Analytical results and the Mott-Hubbard transition”. In: *Eur. Phys. J. B* 36 (2003), p. 335. DOI: `10.1140/epjb/e2003-00352-7`.

[89] T. Reckling and C. Honerkamp. “Approximating the frequency dependence of the effective interaction in the functional renormalization group for many-fermion systems”. In: *Phys. Rev. B* 98 (2018), p. 085114. DOI: `10.1103/PhysRevB.98.085114`.

[90] J. Reuther and R. Thomale. “Functional renormalization group for the anisotropic triangular antiferromagnet”. In: *Phys. Rev. B* 83 (2011), p. 024402. DOI: `10.1103/PhysRevB.83.024402`.

[91] D. Rohe. “Hierarchical parallelisation of functional renormalisation group calculations — hp-fRG”. In: *Computer Physics Communications* 207 (2016), p. 160. DOI: `10.1016/j.cpc.2016.05.024`.

[92] D. Rohe and W. Metzner. “Pseudogap at hot spots in the two-dimensional Hubbard model at weak coupling”. In: *Phys. Rev. B* 71 (2005), p. 115116. DOI: `10.1103/PhysRevB.71.115116`.

[93] G. Rohringer, A. Toschi, A. Katanin, and K. Held. “Critical Properties of the Half-Filled Hubbard Model in Three Dimensions”. In: *Phys. Rev. Lett.* 107 (2011), p. 256402. DOI: `10.1103/PhysRevLett.107.256402`.

[94] G. Rohringer. “New routes towards a theoretical treatment of nonlocal electronic correlations”. PhD thesis. Vienna University of Technology, 2013.

[95] B. Roulet, J. Gavoret, and P. Nozières. “Singularities in the X-Ray Absorption and Emission of Metals. I. First-Order Parquet Calculation”. In: *Phys. Rev.* 178 (1969), p. 1072. DOI: `10.1103/PhysRev.178.1072`.

[96] M. Salmhofer. *Renormalization. An Introduction.* Springer Berlin Heidelberg, 1999. DOI: `10.1007/978-3-662-03873-4`.

[97] M. Salmhofer and C. Honerkamp. “Fermionic Renormalization Group Flows: Technique and Theory”. In: *Prog. Theor. Exp. Phys* 105 (2001), p. 1. DOI: `10.1143/PTP.105.1`.

[98] D. J. Scalapino. “A common thread: The pairing interaction for unconventional superconductors”. In: *Rev. Mod. Phys.* 84 (2012), p. 1383. DOI: `10.1103/RevModPhys.84.1383`.

[99] D. J. Scalapino and R. L. Sugar. "Monte Carlo calculations of coupled boson-fermion systems. II". In: *Phys. Rev. B* 24 (1981), p. 4295. DOI: `10.1103/PhysRevB.24.4295`.

[100] T. Schäfer, S. Ciuchi, M. Wallerberger, P. Thunström, O. Gunnarsson, G. Sangiovanni, G. Rohringer, and A. Toschi. "Nonperturbative landscape of the Mott-Hubbard transition: Multiple divergence lines around the critical endpoint". In: *Phys. Rev. B.* 94 (2016), p. 235108. DOI: `10.1103/PhysRevB.94.235108`.

[101] T. Schäfer, F. Geles, D. Rost, G. Rohringer, E. Arrigoni, K. Held, N. Blümer, M. Aichhorn, and A. Toschi. "Fate of the false Mott-Hubbard transition in two dimensions". In: *Phys. Rev. B* 91 (2015), p. 125109. DOI: `10.1103/PhysRevB.91.125109`.

[102] T. Schäfer, G. Rohringer, O. Gunnarsson, S. Ciuchi, G. Sangiovanni, and A. Toschi. "Divergent Precursors of the Mott-Hubbard Transition at the Two-Particle Level". In: *Phys. Rev. Lett.* 110 (2013), p. 246405. DOI: `10.1103/PhysRevLett.110.246405`.

[103] T. Schäfer, A. Toschi, and K. Held. "Dynamical vertex approximation for the two-dimensional Hubbard model". In: *Journal of Magnetism and Magnetic Materials* 400 (2016), p. 107. DOI: `10.1016/j.jmmm.2015.07.103`.

[104] T. Schäfer, N. Wentzell, F. Šimkovic, Y.-Y. He, C. Hille, M. Klett, C. J. Eckhardt, B. Arzhang, V. Harkov, F.-M. Le Régent, A. Kirsch, Y. Wang, A. Kim, E. Kozik, E. A. Stepanov, A. Kauch, S. Andergassen, P. Hansmann, D. Rohe, Y. M. Vilk, J. LeBlanc, S. Zhang, A. .-.-M. Tremblay, M. Ferrero, O. Parcollet, and A. Georges. "Tracking the Footprints of Spin Fluctuations: A Multi-Method, Multi-Messenger Study of the Two-Dimensional Hubbard Model". In: *pre-print* (2020). arXiv: `2006.10769`.

[105] U. Schollwöck. "The density-matrix renormalization group in the age of matrix product states". In: *Ann. Phys.* 326 (2011), p. 96. DOI: `j.aop.2010.09.012`.

[106] D. Sénéchal and A.-M. S. Tremblay. "Hot spots and pseudogaps for hole- and electron-doped high-temperature superconductors". In: *Phys. Rev. Lett.* 92 (2004), p. 1. DOI: `10.1103/PhysRevLett.92.126401`.

[107] F. Simkovic, J. P. F. LeBlanc, A. J. Kim, Y. Deng, N. V. Prokof'ev, B. V. Svistunov, and E. Kozik. "Extended Crossover from a Fermi Liquid to a Quasiantiferromagnet in the Half-Filled 2D Hubbard Model". In: *Phys. Rev. Lett.* 124 (2020), p. 017003. DOI: `10.1103/PhysRevLett.124.017003`.

[108] E. Stoudenmire and S. R. White. "Studying Two-Dimensional Systems with the Density Matrix Renormalization Group". In: *Annual Review of Condensed Matter Physics* 3 (2012), p. 111. DOI: `10.1146/annurev-conmatphys-020911-125018`.

[109] A. Tagliavini. "Response functions of correlated systems in the linear regime and beyond". PhD thesis. Eberhard Karls Universität Tübingen, 2018.

[110] A. Tagliavini, C. Hille, F. B. Kugler, S. Andergassen, A. Toschi, and C. Honerkamp. "Multiloop functional renormalization group for the two-dimensional Hubbard model: Loop convergence of the response functions". In: *SciPost Physics* 6 (2019), p. 009. DOI: `10.21468/SciPostPhys.6.1.009`.

[111] L. Taillefer. “Scattering and Pairing in Cuprate Superconductors”. In: *Annu. Rev. Condens. Matter Phys.* 1 (2010), p. 51. DOI: `10.1146/annurev-conmatphys-070909-104117`.

[112] C. Taranto, S. Andergassen, J. Bauer, K. Held, A. Katanin, W. Metzner, G. Rohringer, and A. Toschi. “From Infinite to Two Dimensions through the Functional Renormalization Group”. In: *Phys. Rev. Lett.* 112 (2014), p. 196402. DOI: `10.1103/PhysRevLett.112.196402`.

[113] T. Timusk and B. Statt. “The pseudogap in high-temperature superconductors: an experimental survey”. In: *Rep. Prog. Phys.* 62 (1999), p. 61. DOI: `10.1088/0034-4885/62/1/002`.

[114] A. Toschi, A. A. Katanin, and K. Held. “Dynamical vertex approximation: A step beyond dynamical mean-field theory”. In: *Phys. Rev. B* 75 (2007), p. 45118. DOI: `10.1103/PhysRevB.75.045118`.

[115] A.-M. S. Tremblay, B. Kyung, and D. Sénéchal. “Pseudogap and high-temperature superconductivity from weak to strong coupling. Towards a quantitative theory (Review Article)”. In: *Low Temp. Phys.* 32 (2006), p. 424. DOI: `10.1063/1.2199446`.

[116] S. W. Tsai and J. B. Marston. “$\kappa-(BEDT-TTF)_2X$ organic crystals: superconducting versus antiferromagnetic instabilities in an anisotropic triangular lattice Hubbard model”. In: *Can. J. Phys.* 79 (2001), p. 1463. DOI: `10.1139/p01-085`.

[117] S. Uebelacker and C. Honerkamp. “Self-energy feedback and frequency-dependent interactions in the functional renormalization group flow for the two-dimensional Hubbard model”. In: *Phys. Rev. B* 86 (2012), p. 235140. DOI: `10.1103/PhysRevB.86.235140`.

[118] K. Veschgini and M. Salmhofer. “Schwinger-Dyson renormalization group”. In: *Phys. Rev. B* 88 (2013), p. 155131. DOI: `10.1103/PhysRevB.88.155131`.

[119] D. Vilardi. “Functional renormalization group for strongly interacting Fermi systems”. PhD thesis. Universität Stuttgart, 2018.

[120] D. Vilardi, C. Taranto, and W. Metzner. “Antiferromagnetic and d-wave pairing correlations in the strongly interacting two-dimensional Hubbard model from the functional renormalization group”. In: *Phys. Rev. B* 99 (2019), p. 104501. DOI: `10.1103/PhysRevB.99.104501`.

[121] D. Vilardi, C. Taranto, and W. Metzner. “Dynamically enhanced magnetic incommensurability: Effects of local dynamics on nonlocal spin correlations in a strongly correlated metal”. In: *Phys. Rev. B* 97 (2018), p. 235110. DOI: `10.1103/PhysRevB.97.235110`.

[122] D. Vilardi, C. Taranto, and W. Metzner. “Nonseparable frequency dependence of the two-particle vertex in interacting fermion systems”. In: *Phys. Rev. B* 96 (2017), p. 235110. DOI: `10.1103/PhysRevB.96.235110`.

[123] Y. M. Vilk and A.-M. S. Tremblay. “Non-Perturbative Many-Body Approach to the Hubbard Model and Single-Particle Pseudogap”. In: *J. Phys. I France* 7 (1997), p. 1309. DOI: `10.1051/jp1:1997135`.

[124] J. Vucicevic, N. Wentzell, M. Ferrero, and O. Parcollet. “Practical consequences of the Luttinger-Ward functional multivaluedness for cluster DMFT methods”. In: *Phys. Rev. B* 97 (2018), p. 125141. DOI: `10.1103/PhysRevB.97.125141`.

[125] W.-S. Wang, Y.-Y. Xiang, Q.-H. Wang, F. Wang, F. Yang, and D.-H. Lee. “Functional renormalization group and variational Monte Carlo studies of the electronic instabilities in graphene near $\frac{1}{4}$ doping”. In: *Phys. Rev. B* 85 (2012), p. 035414. DOI: `10.1103/PhysRevB.85.035414`.

[126] Y. Wang, N. P. Ong, Z. A. Xu, T. Kakeshita, S. Uchida, D. A. Bonn, R. Liang, and W. N. Hardy. “High Field Phase Diagram of Cuprates Derived from the Nernst Effect”. In: *Phys. Rev. Lett.* 88 (2002), p. 257003. DOI: `10.1103/PhysRevLett.88.257003`.

[127] F. J. Wegner and A. Houghton. “Renormalization Group Equation for Critical Phenomena”. In: *Phys. Rev. A* 8 (1973), p. 401. DOI: `10.1103/PhysRevA.8.401`.

[128] S. Weinberg. *The Quantum Theory of Fields.* Cambridge University Press, 1995. DOI: `10.1017/cbo9781139644167`.

[129] N. Wentzell, G. Li, A. Tagliavini, C. Taranto, G. Rohringer, K. Held, A. Toschi, and S. Andergassen. “High-frequency asymptotics of the vertex function: diagrammatic parametrization and algorithmic implementation”. In: *pre-print* (2016). arXiv: `1610.06520`.

[130] N. Wentzell, C. Taranto, A. Katanin, A. Toschi, and S. Andergassen. “Correlated starting points for the functional renormalization group”. In: *Phys. Rev. B* 91 (2015), p. 045120. DOI: `10.1103/PhysRevB.91.045120`.

[131] N. Wentzell. “Functional renormalization group beyond the perturbative regime”. PhD thesis. Eberhard Karls Universität Tübingen, 2016.

[132] C. Wetterich. “Exact evolution equation for the effective potential”. In: *Phys. Lett. B* 301 (1993), p. 90. DOI: `10.1016/0370-2693(93)90726-X`.

[133] S. R. White. “Density matrix formulation for quantum renormalization groups”. In: *Phys. Rev. Lett.* 69 (1992), p. 2863. DOI: `10.1103/PhysRevLett.69.2863`.

[134] K. G. Wilson. “The renormalization group and critical phenomena”. In: *Rev. Mod. Phys.* 55 (1983), p. 583. DOI: `10.1103/RevModPhys.55.583`.

[135] K. G. Wilson. “The renormalization group: Critical phenomena and the Kondo problem”. In: *Rev. Mod. Phys.* 47 (1975), p. 773. DOI: `10.1103/RevModPhys.47.773`.

[136] W. Wu, M. Ferrero, A. Georges, and E. Kozik. “Controlling Feynman diagrammatic expansions: Physical nature of the pseudogap in the two-dimensional Hubbard model”. In: *Phys. Rev. B* 96 (2017), p. 041105. DOI: `10.1103/PhysRevB.96.041105`.

[137] K.-Y. Yang, T. M. Rice, and F.-C. Zhang. “Phenomenological theory of the pseudogap state”. In: *Phys. Rev. B* 73 (2006), p. 174501. DOI: `10.1103/PhysRevB.73.174501`.

[138] T. Yoshida, X. J. Zhou, T. Sasagawa, W. L. Yang, P. V. Bogdanov, A. Lanzara, Z. Hussain, T. Mizokawa, A. Fujimori, H. Eisaki, Z.-X. Shen, T. Kakeshita, and S. Uchida. In: *Phys. Rev. Lett.* 91 (2003), p. 027001. DOI: `10.1103/PhysRevLett.91.027001`.

[139] D. Zanchi. “Angle-resolved loss of Landau quasiparticles in 2D Hubbard model”. In: *Europhys. Lett.* 55 (2001), p. 376. DOI: `10.1209/epl/i2001-00413-7`.

[140] D. Zanchi and H. J. Schulz. “Weakly correlated electrons on a square lattice: Renormalization-group theory”. In: *Phys. Rev. B* 61 (2000), p. 13609. DOI: `10.1103/PhysRevB.61.13609`.

[141] D. Zanchi and H. J. Schulz. “Weakly correlated electrons on a square lattice: A renormalization group theory”. In: *Europhys. Lett.* 44 (1998), p. 235. DOI: `10.1209/epl/i1998-00462-x`.

[142] D. Zanchi and H. J. Schulz. “Instabilities of weakly correlated electronic gas on a two dimensional lattice”. In: *Z. Phys. B - Condensed Matter* 103.2 (1996), p. 339. DOI: `10.1007/s002570050385`.

[143] S. Zhang. “Quantum Monte Carlo Methods for Strongly Correlated Electron Systems”. In: *Theoretical Methods for Strongly Correlated Electrons*. Ed. by B. C. Sénéchal D. Tremblay A.-M. S. Springer New York, 2004, pp. 39–74. DOI: `10.1007/0-387-21717-7_2`.